

7-11-2013

A time-of-flight spectrometer for fission fragment identification

Richard Blakeley

Follow this and additional works at: https://digitalrepository.unm.edu/ne_etds

Recommended Citation

Blakeley, Richard. "A time-of-flight spectrometer for fission fragment identification." (2013). https://digitalrepository.unm.edu/ne_etds/29

This Thesis is brought to you for free and open access by the Engineering ETDs at UNM Digital Repository. It has been accepted for inclusion in Nuclear Engineering ETDs by an authorized administrator of UNM Digital Repository. For more information, please contact disc@unm.edu.

Richard Blakeley
Candidate

Chemical & Nuclear Engineering
Department

This thesis is approved, and it is acceptable in quality and form for publication:

Approved by the Thesis Committee:

Dr. Adam Hecht, Chairperson

Dr. Robert Busch

Dr. Gary Cooper

**A Time-of-Flight Spectrometer for Fission Fragment
Identification**

By

Richard E. Blakeley

Bachelor of Science – Nuclear Engineering 2009

University of New Mexico

Submitted in Partial Fulfillment of the
Requirements for the Degree of

Master of Science

Nuclear Engineering

The University of New Mexico
Albuquerque, New Mexico

May 2013

A Time-of-Flight Spectrometer for Fission Fragment Identification

by

Richard Blakeley

B.S., Nuclear Engineering, University New Mexico, 2006

M.S., Nuclear Engineering, University New Mexico, 2013

ABSTRACT

Fission fragment and product inventories play a key role in many areas of nuclear science from simulation of fissioning systems to diagnostics for optimal reactor operation and waste disposal. New experimental data are needed to further reduce the uncertainty in the current standard data as well as investigating fission fragment distributions for incident neutron energies where no data currently exist.

To accomplish these goals the Spectrometer for Ion Detection in Fission Research (SPIDER) project is intended to be a multi-armed, high-efficiency, high-resolution time-of-flight spectrometer for event-by-event fission fragment identification. As a contribution to the project, a single module timing detector was designed and constructed to be fielded at the LANSCE facility at Los Alamos National Laboratory at a later date.

The development and performance of the prototype single module, timing detector has shown improved efficiency (68%-70%) and sharper microchannel plate vs. surface barrier coincidence event time-resolution (6.38 ns) than previous, similar experiments.

TABLE OF CONTENTS

A Time-of-Flight Spectrometer for Fission Fragment Identification	ii
<i>ABSTRACT</i>	<i>iii</i>
<i>ACKNOWLEDGEMENTS</i>	<i>viii</i>
<i>INDEX OF FIGURES</i>	<i>ix</i>
<i>INDEX OF TABLES</i>	<i>xiii</i>
Chapter 1	1
Introduction & Purpose	1
<i>1.1 Fundamental Theory</i>	<i>2</i>
<i>1.2 Fundamental Measurements (K,Q and R values)</i>	<i>3</i>
1.2.1 K, Q and R Values	4
<i>1.3 Next Generation Reactor Design & Operation</i>	<i>6</i>
<i>1.4 Passive and Active Interrogation</i>	<i>8</i>
<i>1.5 Experimental Solution</i>	<i>11</i>
<i>1.6 Organization of Thesis</i>	<i>12</i>
Chapter 2	13
Background on Experimental Fission Product Measurements	13
<i>2.1 Methods for Fission Fragment Identification</i>	<i>13</i>
2.1.1 Radiochemical Separation and Mass Recoil Spectrometry	13
2.1.2 Mass Separation for Unslowed Fission Products (Lohengrin)	14
2.1.3 COSI FAN TUTTE (Double Velocity, Double Energy or 2V, 2E Spectrometer)	16
2.1.4 Spectrometer for Ion Detection in Fission Research (SPIDER)	20
2.1.5 SPIDER “Single-Arm” Prototype	21
2.1.6 Mass Resolution Error Accounting	23

Chapter 3	25
Characterizing the TOF Spectrometer	25
<i>3.1 Time-of-Flight Simulation</i>	25
<i>3.2 Chamber Design</i>	27
<i>3.3 Detectors</i>	28
3.3.1 Microchannel Plate Detector	29
3.3.1.1 Construction and Operating Principles	30
3.3.1.2 Gain Limiting Mechanisms	35
3.3.1.3 MCP Detection Efficiency	36
3.3.1.4 MCP Time Response	39
3.3.2 Hamamatsu F-9890-11	40
3.3.2.1 F-9890-11 Set-up & Installation	41
3.3.2.2 F-9890-11 Characterization	44
3.3.2.3 F-9890-11 Time Response	45
3.3.2.4 F-9890-11 Pulse Height Distribution & Charge Saturation	47
3.3.3 Passivated Implanted Planer Silicon (PIPS) Detector	50
3.4 Single Module Construction	51
3.4.1 Material selection	52
3.4.2 Reflection/Acceleration Grid Construction	53
3.4.2.1 FR4 Grid Frames	53
3.4.3 Housing	57
3.4.4 Carbon Foil Measurements	60
Chapter 4	65
Experimental Results	65

4.1 <i>Single Module Efficiency Measurements</i>	65
4.1.1 Single Module Efficiency Calculations	66
4.1.2 Single Module Efficiency Measurements	70
4.2 <i>Single Module Timing Measurements</i>	76
4.2.1 Timing Optimization	76
4.2.2 Time Resolution Measurement	78
Chapter 5	81
Conclusions	81
Chapter 6	82
Future Work	82
6.1 <i>MCP-MCP Characterization</i>	82
6.2 <i>Ion Chamber</i>	82
Bibliography	86
Appendix A	91
A.1 <i>MCP Further Information</i>	91
A.1.1 MCP Composition	91
A.1.2 Dark Current	91
A.1.3 MCP Lifetime Characteristics	92
A.2 <i>Simulations of Active Interrogation & Use of Fission Fragment Data</i>	93
A.2.1 Active Interrogation Simulation Study	94
A.2.2 Means for Simulation	96
A.2.3 Experimental Benchmark Description	97
A.2.4 Simulations	97
A.2.5 Results	100

A.2.6 Further Simulation Work	107
A.2.7 Simulation Conclusions	109

ACKNOWLEDGEMENTS

I'd like to begin by thanking the people who have been instrumental in the completion of the work submitted herein, most of all my parents, Mark and Diane Blakeley for their unconditional support. Without them, my accomplishments wouldn't be possible.

I'd also like to thank my adviser Dr. Adam Hecht for his diligent efforts in setting up beneficial collaborations, insightful suggestions and guidance through the experimental process. Ken Carpenter for his patience while fielding countless questions and sharing his unique practical knowledge. Thank you to professors and mentors Dr. Robert Busch, Dr. Gary Cooper and Dr. Anil Prinja for their moral and intellectual support throughout my time in both graduate and undergraduate education.

Equally invaluable, the input and cooperative work environment created by my fellow group member and friend, Drew Mader, the assistance given by Elliott Leonard (Mr. C++) for everything computer science related.

INDEX OF FIGURES

- Figure 1: Neutron energy spectrum produced at the LANSCE/WNR facility
[White, 2012]
- Figure 2: Calculated and measured fission fragment distributions for thermal and
2 MeV incident neutrons on fission target test sphere.
- Figure 3: Contour difference plot in % / fission of GEANT4 simulations minus
England & Rider experimental data.
- Figure 4: Lohengrin detector principles and operation [ILL, 2012]
- Figure 5: Illustration of a back-to-back TOF spectrometer
- Figure 6: COSI-FAN-TUTTE experimental setup [Boucheneb, 1989]
- Figure 7: SPIDER time detector during installation process
- Figure 8: Single module unit setup
- Figure 9: A single fission fragment through carbon and subsequent electron
emission
- Figure 10: GEANT4 simulated TOF results
- Figure 11: a) External view of the experimental chamber b) Turbo pump
connected to the experimental chamber
- Figure 12: Illustrates a simplified MCP
- Figure 13: Charge multiplication within a single channel of the MCP
- Figure 14: MCP gain as a function of voltage for various length-to-diameter
values [Hamamatsu, 2001]
- Figure 15: Chevron configuration of two MCPs placed in series
- Figure 16: Gain characteristics of single and multi-stage MCP configurations
[Hamamatsu, 2001]

Figure 17: Electron detection efficiency as a function of energy [Hamamatsu, 2001]

Figure 18: MCP sensitivity to 500 eV to 1 keV primary electrons as a function of incident angle [Hamamatsu, 2001]

Figure 19: Typical output signal from a fast response MCP [Hamamatsu, 2001]

Figure 20: a) MCP support setup b) MCP installed on its side, inside the six-way cross

Figure 21: External view of the MCP experimental setup

Figure 22: MCP output signal at varied voltage potentials

Figure 23: F-9890-11 output signal at a bias voltage of 2200V. The output pulse settles to baseline after ~35 ns.

Figure 24: a) 109PC pre-amplified signal b) 590A amplified signal

Figure 25: Pulse height distribution for the Hamamatsu F-9890-11 MCP

Figure 26: a) Acceleration grid FR4 frame dimensions b) Reflection grid FR4 frame dimensions

Figure 27: Au-W wire grid construction device

Figure 28: a) FR4 grid frame installation b) FR4 grid frame soldering setup

Figure 29: Au-W parallel wire array soldered to an acceleration grid frame

Figure 30: 1) Housing top plate. 2) Back plate, reflection grid holder. 3) Base plate. 4) Front plate, source holder/collimator.

Figure 31: Housing with acceleration and reflection grids installed while dimensions are measured

Figure 32: Experimental setup for C foil measurements

Figure 33: energy spectra measurements for the collided (with C foil) and uncollided (no C foil) setups.

Figure 34: Comparison of simulation and experiment. Tri-nuclide alpha energy spectra through $100 \mu\text{g}/\text{cm}^2$ carbon

Figure 35: Example of SIMION geometry setup for secondary electron timing and efficiency simulations

Figure 36: Final dimensions used for efficiency / timing measurements

Figure 37: Experimental setup for the coincidence efficiency measurement

Figure 38: a) Simulated SE flight path with the single module shifted forward by 1.5 cm, hit efficiency = 70-80%. b) Initial MCP position, hit efficiency = 5-10%

Figure 39: Efficiency of the single module coincidence unit.

Figure 40: a) Reflection potential at 2500 V, acceleration potential at 1000 V b) Reflection potential at 1000V, acceleration potential at 1000 V

Figure 41: Electric potential regions in the single module unit

Figure 42: Experimental setup for the timing / coincidence measurements

Figure 43: Timing results for the PIPS-MCP coincidence measurements

Figure 44: Axial IC installed onto ConFlat flange

Figure 45: IC experimental setup

Figure 46: Early results for IC energy spectrum using a $0.025 \mu\text{Ci}$ Tri-nuclide source

Figure A1: Gain reduction as a function of operation time [Hamamatsu, 2001]

Figure A2: GEANT4 representation of the Uranium sphere

Figure A3: Comparison of average rate of photons per fission

Figure A4: Comparison of average rate of photon energy released per fission

Figure A5: Comparison of time-integrated average energy per photon between computational methods and Fisher and Engle experimental quantities.

Figure A6: a) Contour plot of fission product data from England & Rider for ^{235}U in % / fission. b) Contour plot of simulated fission product data for ^{235}U using GEANT4 in % / fission.

INDEX OF TABLES

- Table 1: MCP gain characteristics as a function of l/d and applied voltage [Kosev, 2007]
- Table 2: Detection efficiencies for MCP [Wiza, 1979]
- Table 3: Specifications for the Hamamatsu F-9890-11
- Table 4: MCP voltage for ion/ photon & electron detection modes [Roentdek, 2013]
- Table 5: Test operating voltages for the F-9890-11 MCP
- Table 6: Summary of the A-450-20-AM PIPS detector characteristics
- Table 7: Comparison between G10 & FR4 outgassing properties [NASA, 2013]
- Table 8: Peak energy results from simulated and experimental foil measurements.
- Table 9: SE production properties for α -particles and fission fragments through 2 $\mu\text{g}/\text{cm}^2$ carbon foil
- Table 10: SIMION SE simulation results.
- Table A1: MCP glass composition by element [Wiza, 1979]
- Table A2: Results from the Fisher and Engle experiment, GEANT4 simulation, and MCNPX/CINDER simulation.
- Table A3: Proportional difference below Fisher and Engle experimental values, of GEANT4 and of MCNPX/CINDER results. All differences are in percent (%).

Chapter 1

Introduction & Purpose

This work proposes to contribute to the further advancement of the fundamental understanding of the neutron induced fission process, particularly in regard to the production of post-scission fission products. Typically, post-scission theoretical models are lacking precision in prediction of fission fragment yield distribution values. This is generally due to scarce experimental data available. The scope of this work specifically addresses the initial building and testing of a detector system for a prototype, single-arm spectrometer for fission fragment identification.

Fission product yield experiments performed by England & Rider in the early 1990's [England, 1993] have been the most extensive to date and are currently utilized in the ENDF/B-VI nuclear data library. However, as the data needs of researchers and advancements in computing capability have changed over the past two decades, so has the need for a more complete and accurate set of fission product yield data. These data needs are generally specific, used as a standard, to assess important quantities from actinide burn up in reactors and fission rates [Chadwick, 2011] to time dependent expected delayed gamma intensities for active and passive interrogation techniques [Blakeley, 2011] for homeland security purposes. Most importantly, this work will also help to facilitate the

continuing effort towards understanding fundamental fission theory, that will decrease error in prediction and simulation [White, 2012].

Fission fragment yield experiments carried out using the COSI FAN TUTTE detector have successfully measured fragments to 1 atomic mass unit (amu) for light fragments and 2-3 amu for heavy fragments [Boucheneb, 1989] from experiments with thermal neutrons on ^{229}Th . Through the utilization of fast-timing electronics, increased efficiency and resolution, the Spectrometer for Ion Detection in Fission Research (SPIDER) detector array aims to achieve a mass resolution of 1 amu for both light and heavy fragments produced by a wide range of incident neutron energies.

Outside of data from thermal energy neutrons and the typical 14 MeV neutrons found in Deuterium-Tritium neutron generators, direct measurement of intermediate and high energy neutron induced fission data are extremely limited, but are growing interest with the resurgence of the nuclear industry and the complex issues of handling waste [Ganesan, 1990; Chadwick, 2011]. Specifics on how the improved resolution and efficiency of the SPIDER detector will help to enable researchers to better quantify their predictive capability and diminish the uncertainties in nuclear data where fission product yield is of importance are discussed in this chapter.

1.1 Fundamental Theory

Fission theory and modeling has progressed at a staggering rate with the advent of increased computing power. However, acquisition of empirical data has not

followed at the same rate. This has left recent innovations in fission modeling with few experimental benchmarks to verify simulated results, especially in the prediction of fission fragment distributions. The current fission model, developed by Moller et al [Moller, 1995] at Los Alamos National Laboratory (LANL), has been considered the standard since its inception in the 1990's. This is an extension of the fission model established by Nix *et al* [Nix, 1972] at LANL in the 1970's. The current model employs a five-coordinate fission shaping system described by nuclear elongation, mass asymmetry, necking and two deformation variables added by Moller *et al* [Moller, 1995]. Current modeling techniques are still ineffective at accurately determining fission fragment yields, both independent and cumulative. However, the techniques have been used to accurately predict mean fragment energies in the low-energy fission of actinides [Moller, 2001]. Precise knowledge of the fission fragments created in event-by-event fission, can give information on pre-formation in the nucleus before scission, which is determined by the potential energy deformation minima of the nucleus. With the high resolution, high efficiency detector array proposed by the SPIDER project, data previously unavailable to theorists can be used to benchmark current and future fission models to precisely predict fission product yields.

1.2 Fundamental Measurements (K,Q and R values)

A common measurement technique to measure fission rates employed by LANL and various other national laboratories around the country has been to correlate the fragment yields of ^{99}Mo and ^{147}Nd to determine the number of fissions in a given volume at various incident neutron energies. These two reference isotopes

are also utilized in part due to their favorable half-lives. This is of importance as these two nuclei are used as the standard reference for fission rate calculations applied to various experiments and operations within the national laboratory network. The previous consensus was these particular fragment yields showed little variation in yield percentage with incident neutron energy. This has recently come under investigation based on discrepancies between reported yield values of LANL and Lawrence Livermore National Laboratory (LLNL) [Chadwick, 2011].

1.2.1 K, Q and R Values

The calibration method of relating post fission observables to fission rates within a system has been employed since the early days of the Manhattan Project [Selby, 2010]. The K-factor relates the total number of fissions, F , to the activity of a specific isotope in counts per minute, A_j , obtained through radiochemical separation and subsequent counting of β and γ radiation of a particular nuclide (described further in section 2.1.1). K factors accounted for various neutron energies and fuel type by concurrent irradiation of various fuel compositions along with the reference foil under identical irradiation conditions. Below, the relation between K-factors and cumulative fission product yield is given [Selby, 2010].

$$K = \frac{F}{A_j} \quad [\text{Eq. 1}]$$

with,

$$A_j = N_j \varepsilon_j \lambda_j = F Y_j \varepsilon_j \lambda_j \quad [\text{Eq. 2}]$$

Where N_j is the number of atoms, ϵ_j encapsulates both counting efficiency as well as respective branching ratios, λ_j the respective decay constant and Y_j representative of the cumulative fission product yield of the j-th isotope. In the end, we have the K-factor in relation to the fission product cumulative yield,

$$K = \frac{1}{Y_j \epsilon_j \lambda_j} \quad [\text{Eq. 3}]$$

Therefore we are left with a simple relation of the total number of fissions to the fission product cumulative yield of the j-th nuclide,

$$F = A_j K_j = \frac{N_j}{Y_j} \quad [\text{Eq. 4}]$$

The K-factor on its own is not of much use as direct comparisons require identical conditions. However, LANL Radiochemistry constructed a method using the so-called Q- and R-values to relate the reference K-factor to various fuel types and irradiation conditions. The detector independent Q-value ratios are expressed below:

$$Q_j = \frac{K_j^*}{K_j^{f,e}} = \frac{Y_j^{f,e}}{Y_j^*} \quad [\text{Eq. 5}]$$

The asterisk indicates the reference fission material and incident neutron energy, while the f,e superscript indicates the fission material and neutron energy of the non-reference fissionable material. The standard reference used in the LANL evaluations is thermal neutrons incident on ^{235}U .

The R-values are composed of a double ratio of measured activity from two fission products in the reference and non-reference fission materials,

$$R_j = \frac{\frac{A_j^{f,e}}{A_i^{f,e}}}{\frac{A_j^*}{A_i^*}} = \frac{r_j^{f,e}}{r_j^*} \quad [\text{Eq. 6}]$$

With precise measurements made for the thermal r_j^* values and accurate measurements performed for the non-reference $r_j^{f,e}$ values, K- and Q- values can be derived independent of fuel material or incident neutron energy. For K-factors;

$$K_j^{f,e} = \frac{K_j^{f,e}}{r_j^* R_j^{f,e}} = \frac{K_j^*}{r_j^* Q_j^{f,e}} \quad [\text{Eq. 7}]$$

For Q-values;

$$Q_j^{f,e} = \frac{R_j^{f,e} K_j^*}{K_j^{f,e}} = R_j^{f,e} Q_j^{f,e} \quad [\text{Eq. 8}]$$

The dependencies within the R-value process are highly contingent on the accuracy of the fundamental measurements, i.e., the precision of the fission product yield data obtained in reference measurements. The SPIDER project will help to diminish the uncertainties in these fundamental quantities to increase certainty in the R-value process utilized to assess fission rates at the national laboratories.

1.3 Next Generation Reactor Design & Operation

Fission product yield data have been used in the nuclear industry for many years as a diagnostic assessment tool for important quantities that address issues from reactor performance to safety [IAEA, 2000]. Fission fragment yield data are currently used in criticality and reactivity calculations for reactor design, core

management, fission gas accumulation and decay heat production after shutdown as well as decay heat generated in stored spent fuel for plant operation and safety [IAEA, 2000].

The data needs for fission yields differ depending on the application, e.g., reactor kinetics is generally only concerned about the concentration of strong neutron absorbers. On the other hand, calculations of decay heat after shutdown require a complete set of fission product inventories to ensure proper cooling and personnel protection.

There has been an increasing interest and attraction to fast-spectrum reactors as a means of achieving higher burn-up rates as well a reduction in proliferation from increased actinide fission [IAEA, 2000]. Experimental data regarding fast-spectrum neutron induced fission yields are lacking precision, more so than the thermal data currently available to reactor designers.

Accelerator Driven Systems (ADS) operate far beyond the energies of thermal and “fast-spectrum” neutron reactors. ADS functions by creating spallation neutrons using proton irradiation in the GeV energy range impinging on a high Z target to produce neutrons with energy up to 160 MeV [IAEA, 2000]. Figure 1 shows the expected fluence rate as a function of energy at the LANSCE facility.

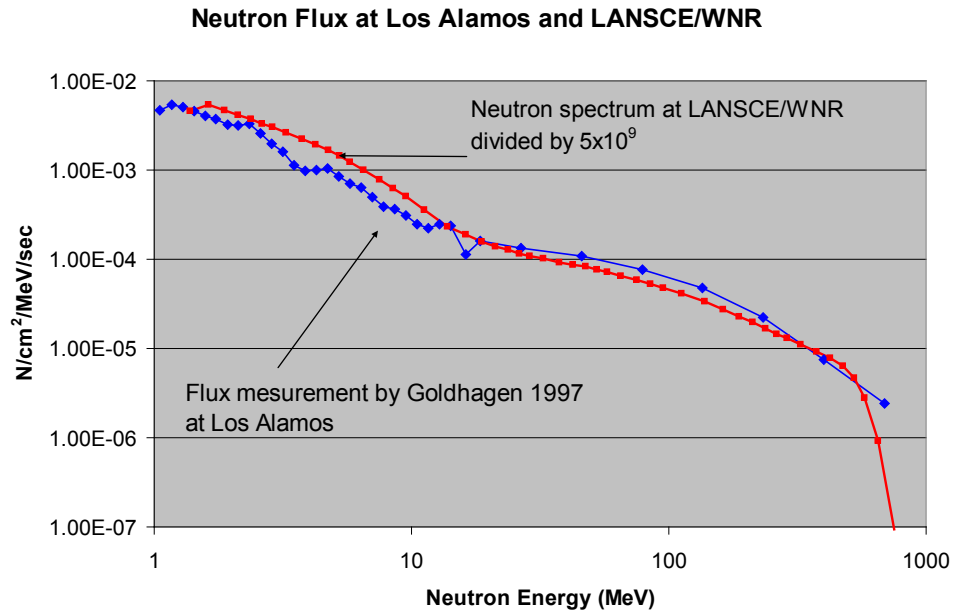


Figure 1: Neutron energy spectrum produced at the LANSCE/WNR facility
[White, 2012]

The IAEA developed a Coordinated Research Program (CRP) to determine what nuclear data would be needed to model actinide transmutation in such a system. The proposed reactor system would need fission product yield data for several actinides with incident neutron energies approaching 150 MeV [IAEA, 2000]. Several systematics [Katakura, 2003] have been developed that predict the fission product yields at spallation neutron energies, however there are a lack of experimental data to support these systematic approaches to yield predictions.

1.4 Passive and Active Interrogation

Nuclear non-proliferation has been of increased importance during the last few decades. A concern to national security is the transport of illicit fissile material by means of sea, land or air transportation. With the vast number of transport

containers entering and departing the various points of entry across the United States and an increased concern of global terrorism since the events of September 11th, 2001, efforts to detect illicit nuclear material smuggled in cargo containers has gained renewed interest. Passive interrogation techniques are dependent on the detection of decay gammas from smuggled nuclear material and is the current standard for interrogation. These materials may be hidden successfully with the appropriate shielding though. New methods utilizing neutron and/or gamma-ray generators to induce neutron and/or photo fission to detect both delayed neutron and gamma emission from illicit fissile material has been of interest to homeland security. Shielding complicates this scenario, but the expected signal detected from this active form of interrogation is heavily dependent on the fission products generated in the reaction.

An in-depth simulation study was performed to examine the interdependence of delayed gamma emission and fission fragment inventories for active interrogation. Details of the simulation and delayed gamma results are addressed in Appendix A. Figure 2 shows a linear axis plot of the experimental and GEANT4/MCNPX simulated fission product inventories. MCNPX runs off of an experimental inventory and is closer to experimental results at thermal energies than the physics driven simulation Geant4. Better theory can improve such physics driven simulations. Experimental results are sparse for comparison at intermediate energies.

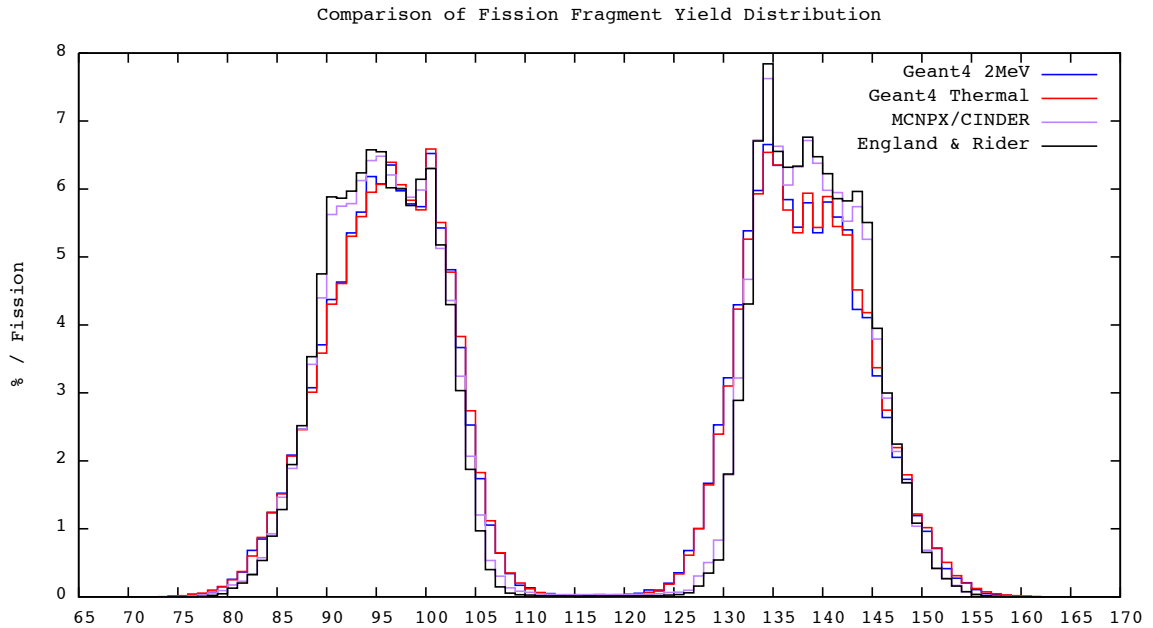


Figure 2: Calculated and measured fission fragment distributions for thermal and 2 MeV incident neutrons on fission target test sphere.

There are significant discrepancies between published experimental data for fission product inventories and those produced through GEANT4 physics based simulation methods. Fission product inventories were collected through simulation and compared to the England & Rider [England, 1993] experimental data for thermal neutrons to illustrate these discrepancies, a difference contour plot is provided in Figure 3.

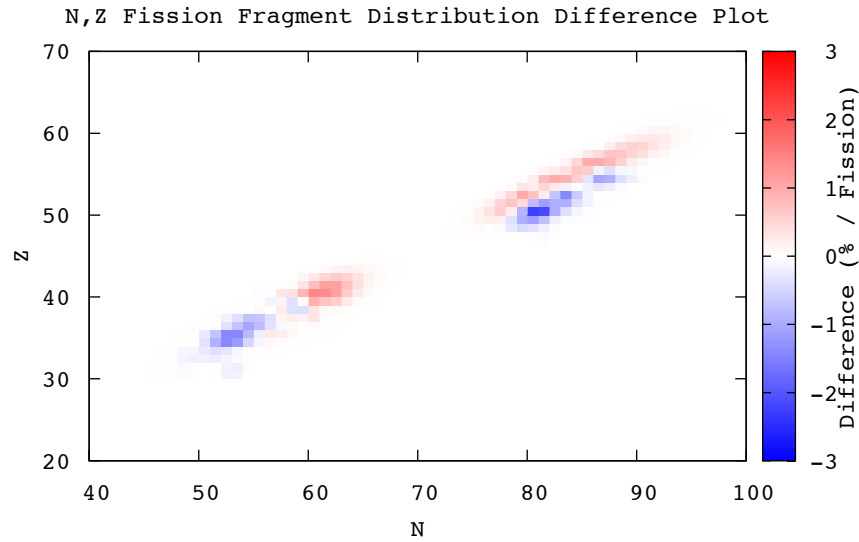


Figure 3: Contour difference plot in %/fission of GEANT4 simulations minus England & Rider experimental data.

GEANT4 determines the fragment yield based on a numerical Monte Carlo scheme, while MCNPX/CINDER determines the yield based on data tables sampled using deterministic methods. MCNPX/CINDER fission product inventories are limited by incident neutron energy data to thermal (0.025 eV), fission (2 MeV) and 14.1 MeV.

1.5 Experimental Solution

In collaboration with Los Alamos National Laboratories (LANL), an effort to research and develop a high-efficiency, high-resolution time-of-flight spectrometer for fission fragment identification is currently underway. The Spectrometer for Ion Detection in Fission Research (SPIDER) project aims to determine the light and heavy fragment distributions to an uncertainty of under

1 amu from fissile and fissionable material over a range incident neutron energies. A full description of the SPIDER project can be found in section 2.1.4.

1.6 Organization of Thesis

The remainder of this work will be split between the efforts performed in regard to simulation studies and physical experimental work. Chapter 2 examines the current and past methods of experimental techniques utilized to obtain physical data. Chapter 3 discusses the construction and implementation of the “Single Arm” prototype detector under development at UNM. Chapter 4 gives analysis of the experimental results for efficiency and timing resolution for a single timing detector. Finally, chapter 5 & 6 discusses the conclusions and further work that will need to be implemented in the final product.

Chapter 2

Background on Experimental Fission Product

Measurements

2.1 Methods for Fission Fragment Identification

There are several methods of experimental measurement employed to evaluate fission product yields. LANL Radiochemistry developed the methods mentioned in section 1.2 regarding the R-value calculation utilizing fission chambers and radiochemical separation techniques [Selby, 2010]. Nonchemical methods include mass recoil spectrometry. The current work involves employing the combination of time-of-flight measurements to obtain velocity information (v) along with an axial ion chamber for total kinetic energy (KE) deposition to resolve the mass (A) of the fragment following $KE = \frac{1}{2} m v^2$. The ionic charge (Z) may be extracted from the axial ion chamber, thus also determining N of the fragment and, with both fragments identified, the number of neutrons boiled off in fission. A survey of methods is presented below to contrast with the new detector method.

2.1.1 Radiochemical Separation and Mass Recoil Spectrometry

Radiochemistry methods have been used extensively to determine cumulative yields of fission fragment inventories. The process for detection generally involves the use of a fission chamber with chemical separation post irradiation. Following separation, gamma and beta counts are taken. This method has an

overall accuracy of 2-5% [Selby, 2010] and produces independent yield data measured shortly after irradiation or cumulative yield data through the collection of integral fission events via long irradiation and counting times, with independent yield methods being measured shortly after irradiation. Theory can be adjusted to emulate these results; however they cannot be used to directly develop relationships to the scission event itself.

2.1.2 Mass Separation for Unslowed Fission Products (Lohengrin)

The Lohengrin detector at the Institut Laue-Langevin (ILL) is the current standard in event-by-event fission fragment detection, used at the Grenoble high flux reactor [ILL]. The Lohengrin detector utilizes recoil mass spectrometry to separate the products of differing mass. An actinide sample is placed near the reactor core and subject to a flux of $5.3 \times 10^{14} \text{ n cm}^{-2} \text{ s}^{-1}$. The fission products that travel down the beam pipe are mass selected (A/Q) by a magnetic field and momentum selected (p/Q) by an electric field, Q being the fragment charge. Products of a single mass are then collected and analyzed using various techniques [Poenaru, 1997]. Figure 4 gives a schematic of the Lohengrin detector.

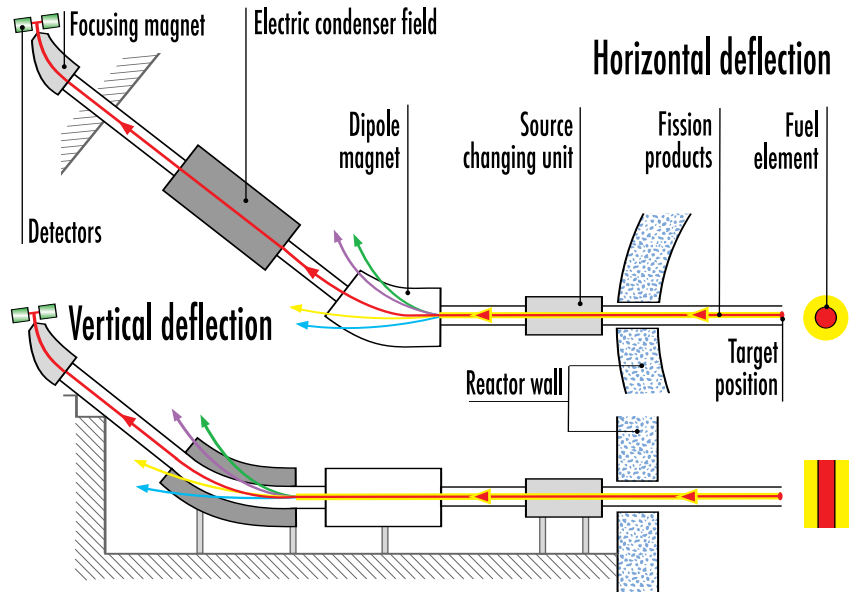


Figure 4: Lohengrin detector principles and operation [ILL, 2012]

The Lohengrin detector has a typical mass resolving power of $\sim A/\Delta A = 1500$, and an energy resolution of $\sim E/\Delta E = 100 - 1000$ for thermal neutron energy induced fission [Poenaru, 1997]. One limitation of the Lohengrin detector stems from the large use of “beam time” and its dependence on careful measurement of fragment charge state as it directly influences the results. Intrinsically, Lohengrin cannot distinguish between “multiplets”, fission products possessing the same A/q value, e.g. $A/q = 100/25$ or $96/24 = 4$. This has been remedied through the inclusion of a surface barrier detector or ionization chamber to collect ion charge data, Z [Poenaru, 1997]. This spectrometer has been used successfully to measure fission products from the $^{235}\text{U}(n_{\text{thermal}}, f)$ reaction and is a primary source of fission fragment data contained within current nuclear data libraries [Selby, 2010].

2.1.3 COSI FAN TUTTE (Double Velocity, Double Energy or 2V, 2E Spectrometer)

Another method for measuring a fission fragment mass is based on the conservation of momentum and energy. In this measurement technique, both the velocity and kinetic energy are measured simultaneously to resolve fragment mass; this is often referred to as the “2V, 2E” method. The 2V, 2E method follows from the simple principle of energy conservation:

$$KE_f = \frac{1}{2} m_f v_f^2 = \frac{1}{2} m_f \left(\frac{l}{t}\right)^2 \quad [\text{Eq. 9}]$$

Where KE_f is the fragment kinetic energy, m_f is the fragment mass, v_f the fragment velocity, l the distance between “start” and “stop” detectors and t the time the fragment takes to traverse distance l . With some basic algebra, the fragment mass can be found by:

$$m_f = \frac{2KE_f}{v_f^2} = \frac{2KE_f}{\left(\frac{l}{t}\right)^2} \quad [\text{Eq. 10}]$$

Typically in this technique, a thin foil of fissile material is placed in the path of a neutron beam of known energy causing fission events. Fragments are emitted fairly back to back from the fission parent position. Placing identical detector setups “back-to-back”, on either side of the irradiated fissile thin foil, allows for velocity and energy measurements for both fragments in an event to be made when the fragment paths line up with the detectors. The velocity measurement can be made through time-of-flight principles. Fission fragments traverse two thin ($\sim 2\text{-}100 \text{ ug cm}^{-2}$) transmission foils, spaced by a known distance, l . The electrons knocked out from these foils are collected by various means to serve as the start and stop times for the velocity measurement. The fission fragment energy measurement is generally done by the means of an ionization chamber or

surface barrier detectors placed behind the time of light setup. The diagram in Figure 5 illustrates how a back-to-back spectrometer setup may look. A similar 2V, 2E method is the basis of the current work.

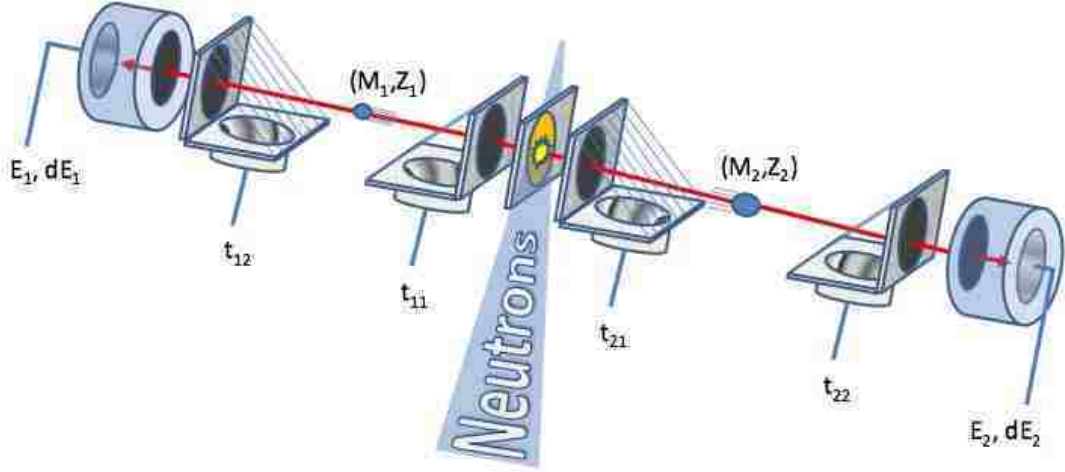


Figure 5: Schematic of how a back-to-back TOF spectrometer would work. This technique has several advantages and disadvantages. One disadvantage includes issues with resolution of both energy and velocity measurements, which are impacted by the recoil energy of the nucleus following prompt neutron evaporation [Poenaru, 1997]. Mathematically,

$$E_{recoil} = \left(\frac{A_n}{A_f} \right) E_n \approx 0.005 - 0.014 \text{ MeV} \quad [\text{Eq. 11}]$$

where E_{recoil} is the recoil energy, A_n the neutron mass number (1), A_f the mass number of the fission fragment (70-170) and E_n is the prompt neutron energy (using a mean energy of ~ 1 MeV). The recoil energy transferred to the fragment is a minimal source of uncertainty. However, it does lead to the broadening of both the energy and velocity distributions. Following Eq. 9, the energy measurement is also impacted by the change in mass from prompt neutron evaporation [Poenaru, 1997]:

$$\Delta E_f(\%) = \frac{\nu}{A_f} * 100 \approx 1.4 - 3.5 \% \quad [\text{Eq.12}]$$

where ΔE_f is the change in fission fragment kinetic energy expressed in percent and ν is the number of neutrons emitted distributed around the mean value $\nu(A)$, which varies between 0.5 – 3 as a function of fragment mass [Poenaru, 1997]. This approximates to a change in fragment energy by roughly 0.5 – 3 MeV. The energy measurement inherently suffers more from prompt neutron emission than the velocity measurement. However in the past, poor detector timing resolution accounted for a greater error [Poenaru, 1997]. Recent improvements in fast timing microchannel plate (MCP) technology have led to a decrease in uncertainty in the velocity measurement.

This method has the advantage of measuring details of the fission process on an event-by-event basis collecting information after each fission, as opposed to integral measurements made with radiochemical separation techniques. This method also produces a complete mass yield in a single experiment, utilizing small amounts of fissile material [Vertes, 2010]. With this method, fragment yields can be obtained, as opposed to radiochemical separation methods, which give delayed products, those nuclides which were decayed into at the time of separation. This event-by-event method maps the fragment production distribution and thus gives information on the pre-fission scission development, which feeds the further development of theoretical fission models and helps lead to predictive capability of fission fragment yield distributions [White, 2012].

The COSI FAN TUTTE spectrometer has yielded a mass resolution for light fragments in the $^{229}\text{Th}(n_{\text{thermal}}, f)$ reaction of 1 amu [Boucheneb, 1989]. Though COSI FAN TUTTE was originally proposed to measure energy and velocity of both fission fragments (2V,2E), the substrate backing on the thorium target foil blocked fission fragment emission from the backside of the target foil, thus operated as a 1V, 1E detector described in Figure 6. The inherent low efficiency (0.01%) of COSI FAN TUTTE limits the feasibility of fission fragment measurements for incident neutron energies outside of the thermal region as the fission cross-section drops strongly with increased neutron energy [White, 2012; Boucheneb, 1989].

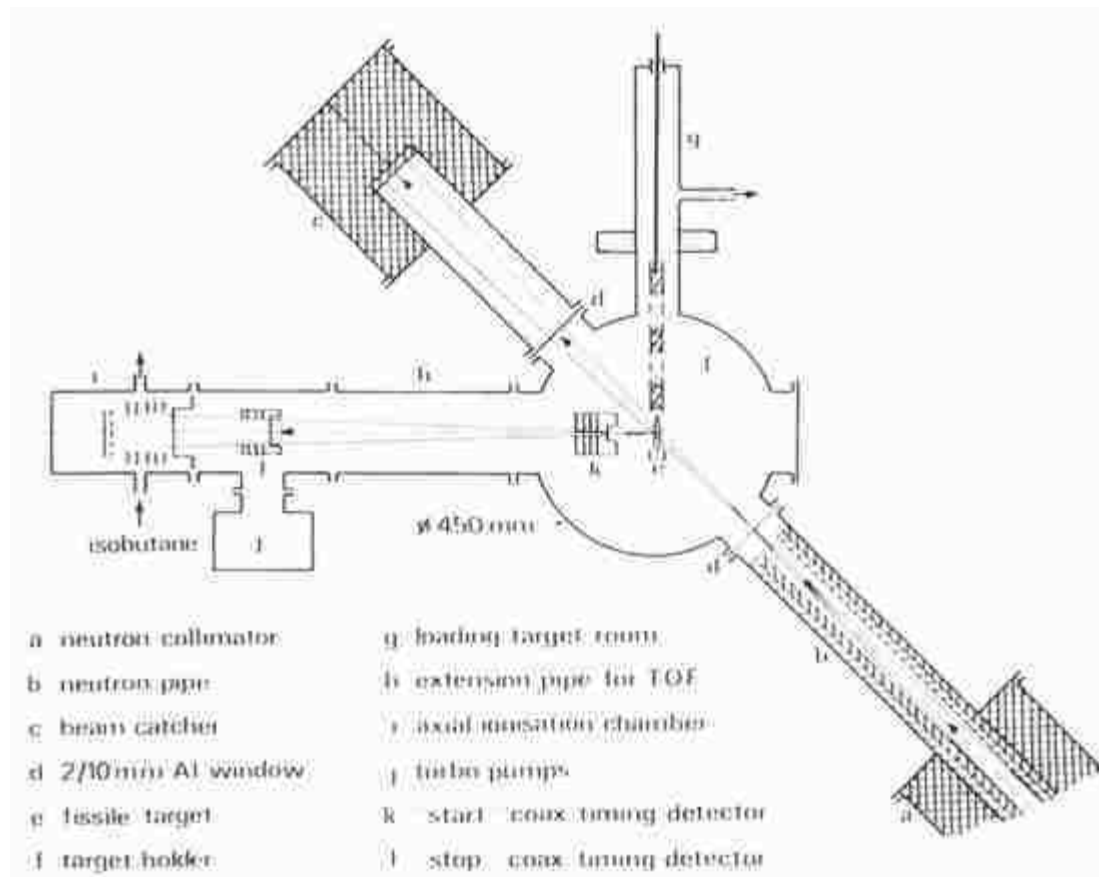


Figure 6: COSI-FAN-TUTTE experimental setup [Boucheneb, 1989]

2.1.4 Spectrometer for Ion Detection in Fission Research (SPIDER)

The SPIDER detector is an ambitious project following the proposed 2V, 2E method of the COSI FAN TUTTE detector. The SPIDER project aims to increase the efficiency and mass resolution by implementing an array of 16 back-to-back 2V, 2E detectors described in Figure 5. Utilizing advancements in time resolution seen in fast-timing MCP, improved energy resolution in ion chambers, digital data acquisition electronics and thin, silicon nitride ion chamber entrance windows to achieve 1 amu resolution on light and heavy fission fragments [White, 2012]. Figure 7 shows one of the SPIDER time detectors being prepared for operation.

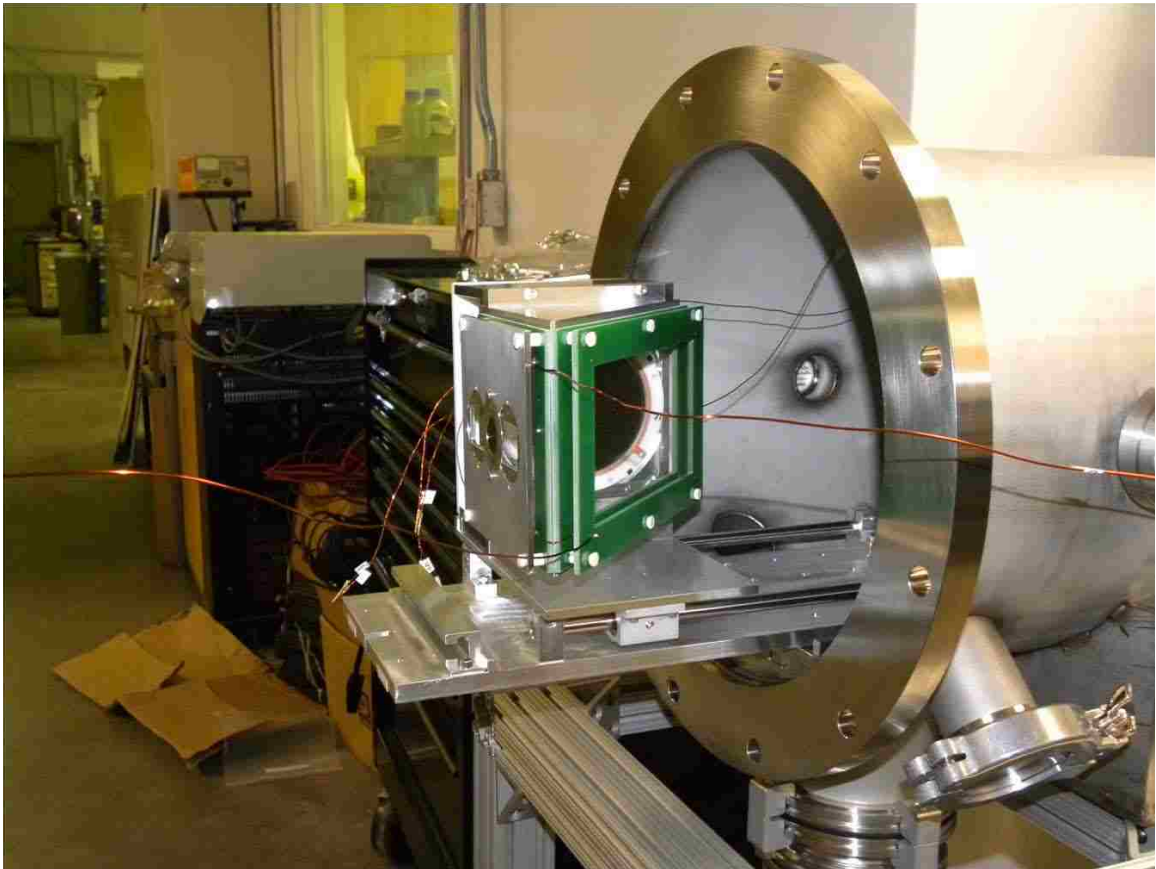


Figure 7: SPIDER time detector during installation process

The improved efficiency will allow researchers to investigate neutron-induced fission outside of the thermal region, through several MeV, where reaction cross-sections are much lower. Event-by-event fission fragment distribution measurements for non-thermal neutron-induced fission reactions have not been undertaken due to the decreased fission cross-section with increased neutron energy with the low collection efficiency of previous detectors. The culmination of the SPIDER project will yield previously uninvestigated data sets as well as new data on thermal neutron induced fission, taking advantage of the broad neutron energy spectra produced at the LANSCE facilities.

Dealing with data deficiencies, rudimentary interpolation techniques have often been used in the past to fill in the gaps between measured data. Advances in theory, namely the LANL potential energy model for a fissioning nuclei, will be employed to evaluate fission fragment yields for various incident energies as well as actinide targets with extremely short half-lives that are infeasible to measure [White, 2012]. Benchmarking the potential energy model to accurate fission fragment data obtained by the SPIDER detector array will help lead to predictive methods for unmeasured actinides and incident neutron energies.

2.1.5 SPIDER “Single-Arm” Prototype

UNM is developing a “Single-Arm” prototype of the proposed detector to assess timing and energy resolution characteristics to optimize design in the SPIDER project. The UNM based project will culminate in a scaled down SPIDER detector using two arms and operating on the low energy (milli eV to a few keV) neutron beamline at LANSCE where the (n,f) cross sections are higher and the

lower efficiency of a two arm spectrometer is appropriate. The development and initial testing of the timing detector portion of the fission fragment spectrometer is the focus of this work. A “single module” has been built and tested using various α sources. The “single module” design depicted below consists of a $100 \mu\text{g}/\text{cm}^2$ carbon foil through which the ion passes and knocks out secondary electrons, acceleration and deflection grids for the ejected electrons, consist of 21 μm diameter gold plated tungsten wire in parallel with 1 mm spacing, a Canberra A-450-20-AM 450 mm^2 surface barrier detector for α detection and a Hamamatsu F-9890-11 fast timing MCP detector for detecting the reflected secondary electrons. Figure 8 presents a diagram of the single module unit with their main components utilized in this work.

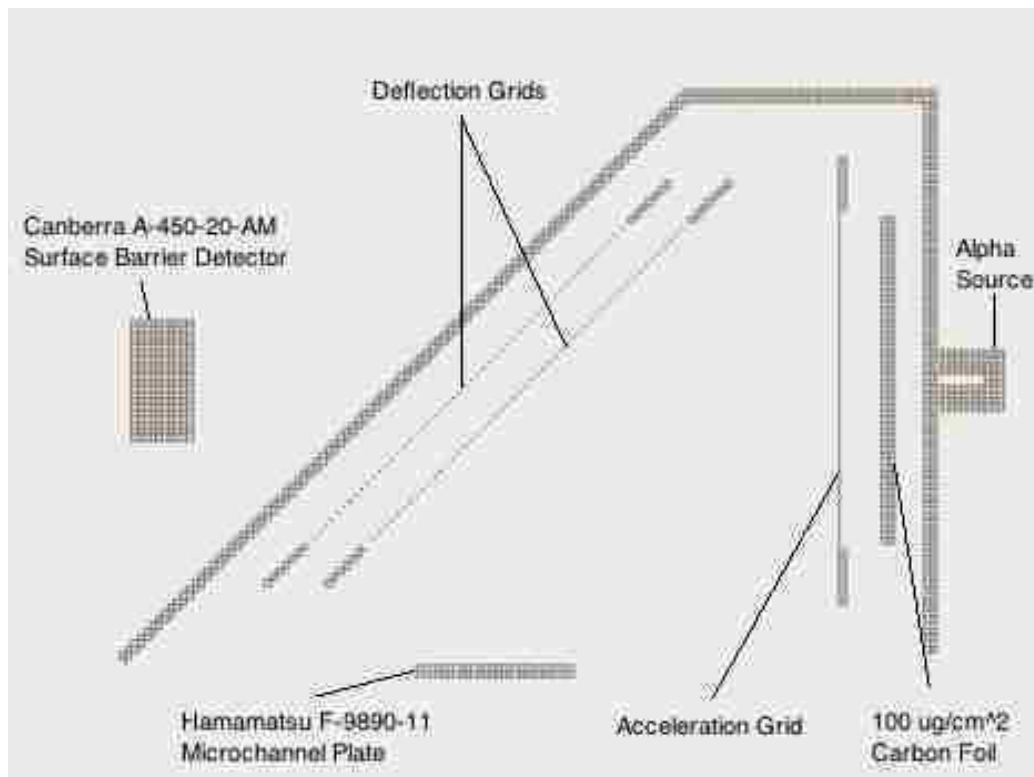


Figure 8: Single module unit setup. The ions enter the module from the right.

The following chapter discusses in detail the construction process and coincidence measurements to determine efficiency and timing resolution of the single module using NIM-based analog data collection methods.

The final design will incorporate two of the single module setups spaced 50 cm apart with the inclusion of an axial ion chamber currently being designed and tested to be attached to the back end of the time of flight setup for energy measurements.

2.1.6 Mass Resolution Error Accounting

The allowable uncertainty in the timing resolution measurement to achieve $A = 1$ amu (FWHM) mass resolution for fission fragments is found using the uncertainty accounting equation, derived from Eq. 9 :

$$\left(\frac{\sigma m}{m}\right)^2 = \left(\frac{\sigma E}{E}\right)^2 + \left(\frac{2\sigma d}{d}\right)^2 + \left(\frac{2\sigma t}{t}\right)^2 \quad [\text{Eq. 13}]$$

where for Gaussian distributions,

$$\sigma m, \sigma E, \sigma t, \sigma d = \frac{FWHM}{2.35} \quad [\text{Eq.14}]$$

Using $A = 140$ as an example, for a mass resolution of 1 amu, a $\sigma m/m$ value of 0.31% is needed. The time, t , for a fragment of 140 amu and ~ 90 MeV of kinetic energy to traverse 50 cm is roughly 50 ns. The foil-to-foil distance, d , can be known precisely using diligent measuring techniques for which we will assume the uncertainty is negligible. Equation 13 is simplified to the following:

$$\left(\frac{\sigma m}{m}\right)^2 = \left(\frac{\sigma E}{E}\right)^2 + \left(\frac{2\sigma t}{t}\right)^2 = 0.0031 \quad [\text{Eq. 15}]$$

The proportional energy uncertainty reduces with ion mass and energy. For the energy uncertainty required for fission fragments, the goal for the IC energy resolution is to reach 1% for alpha particles. In previous axial IC work performed by Oed et al [Oed, 1984], for which the IC being developed is based, a FWHM of 385 keV and 510 keV was achieved for light and heavy fission fragments respectively. Using the FWHM value of 510 keV for heavy fragments we find:

$$\left(\frac{\sigma E}{E}\right) = \left(\frac{217 \text{ keV}}{90000 \text{ keV}}\right) = 0.0024 \quad [\text{Eq.16}]$$

Our collaborators at Los Alamos have recently finished initial testing on the MCP-MCP timing measurements using alpha particles. Initial results have been favorable, returning a time resolution of 190 picoseconds. Translating from resolution given in FWHM/centroid to $2\sigma t$ /centroid, that gives:

$$\left(\frac{2\sigma t}{t}\right) = \left(\frac{2 \cdot 80.85 \text{ ps}}{50,000 \text{ ps}}\right) = 0.0032 \quad [\text{Eq.17}]$$

Using these values, the expected uncertainty of the current setup is given by:

$$\left(\frac{\sigma m}{m}\right) = \sqrt{\left(\frac{\sigma E}{E}\right)^2 + \left(\frac{2\sigma t}{t}\right)^2} = \sqrt{(0.0024)^2 + (0.0032)^2} = 0.004 \quad [\text{Eq.18}]$$

As can be seen in the uncertainty estimate, improvements still need to be made in the timing resolution to realize the goal of 1 amu mass resolution on heavy fragments. Similar calculations show these are already acceptable numbers for sufficient light fragment resolution as the fractional resolution ($\sigma m/90$ for light fragments vs. $\sigma m/140$ for heavy fragments) is less demanding.

Chapter 3

Characterizing the TOF Spectrometer

The main goal of the experimental portion of this work is to characterize and optimize the timing detector for the single-arm prototype. To begin, a simulation study was performed to measure the inherent limit in time resolution for fission fragments based on the collection of secondary electrons. The vacuum chamber design and construction is discussed, followed by a description of the micro-channel plate operation and initial efficiency and time resolution tests. The design and implementation of the single-module coincidence unit is then addressed in detail. Efficiency and timing resolution results for the single-module coincidence unit are analyzed and presented in the final section.

3.1 Time-of-Flight Simulation

With the stringent requirement of detecting fission fragments with a mass resolution of 1 amu FWHM, a simulation study using GEANT4 was performed. In this simulation, two fission fragment isotopes separated by a single neutron mass, e.g., ^{135}Xe and ^{136}Xe , were generated and directed into two, $100\ \mu\text{g}/\text{cm}^2$ carbon foils separated by 50 centimeters. The illustration in Figure 9 is taken directly from simulation to aid with visualization.

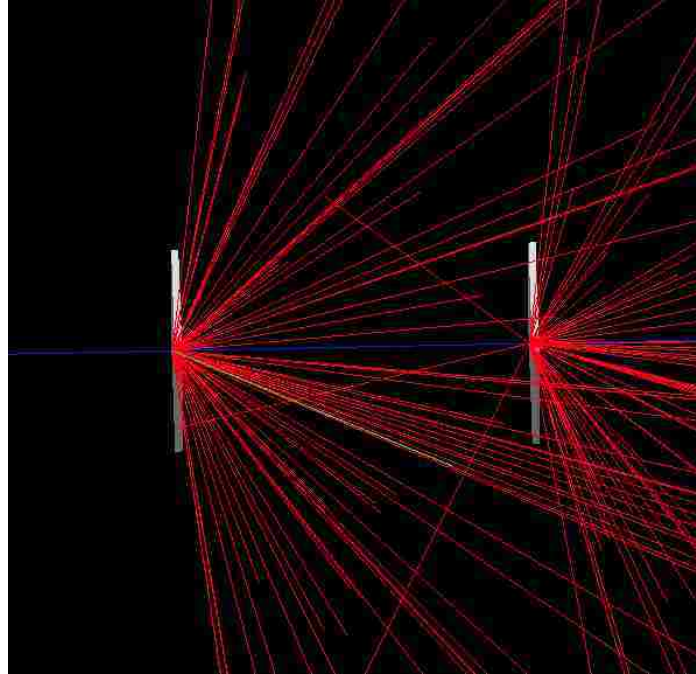


Figure 9: A single fission fragment through carbon and subsequent electron emission

Two electron detectors were simulated behind each of the carbon foils to collect the arrival times of the secondary electrons produced in the carbon foil. To emulate electronic data acquisition limitations, a threshold of ten electrons was set in the electron detectors as a time pick-off, e.g., a fission fragment knocks out 100 electrons in the first foil; when the 10th electron is noted exiting the foil, *time 1* is recorded, the fragment continues to travel to the second carbon foil where the process is repeated to obtain *time 2*. The difference in times represents a time of flight measurement and is recorded and histogrammed.

Using 100,000 particles of each isotopes (Xe-135 and Xe-136 isotopes with a kinetic energy of exactly 70 MeV) for each run, an inherent time resolution of FWHM ~100 picoseconds exists. This sets an expected experimental minimum

achievable resolution regardless of the timing properties of the detectors employed. The results also tell us that if a 100 picosecond timing resolution can be achieved using fast-timing micro-channel plates, it will be possible to distinctively identify fission fragment isotopes differing in mass by a single neutron. A plot of the GEANT4 TOF results for Xe isotopes is given in Figure 10.

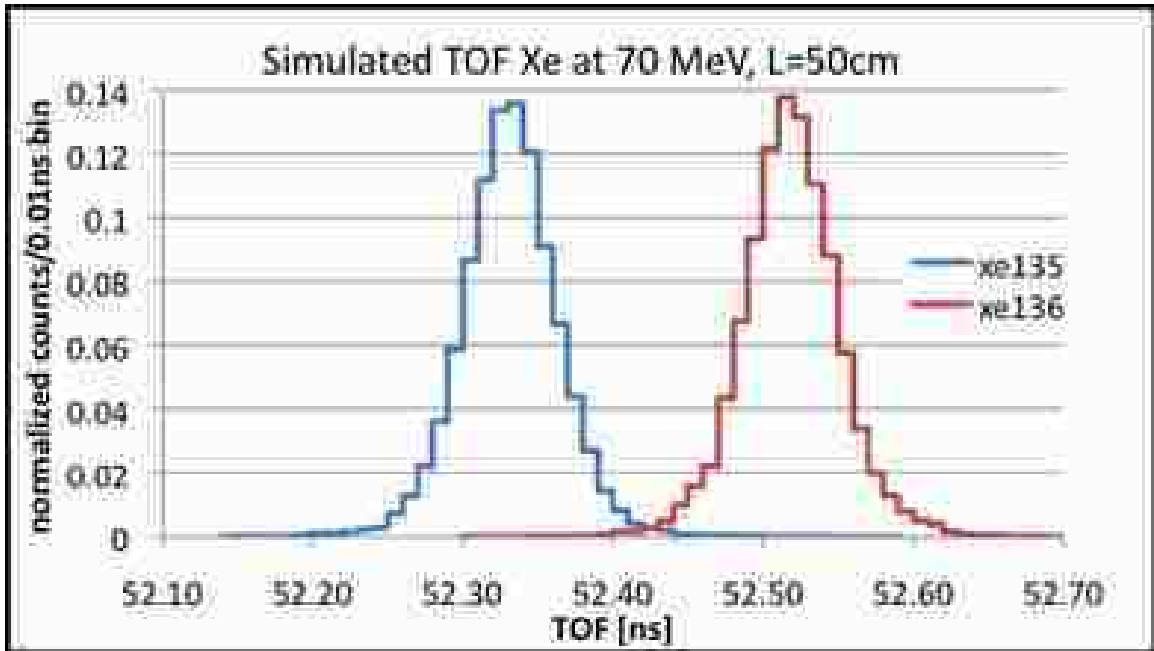


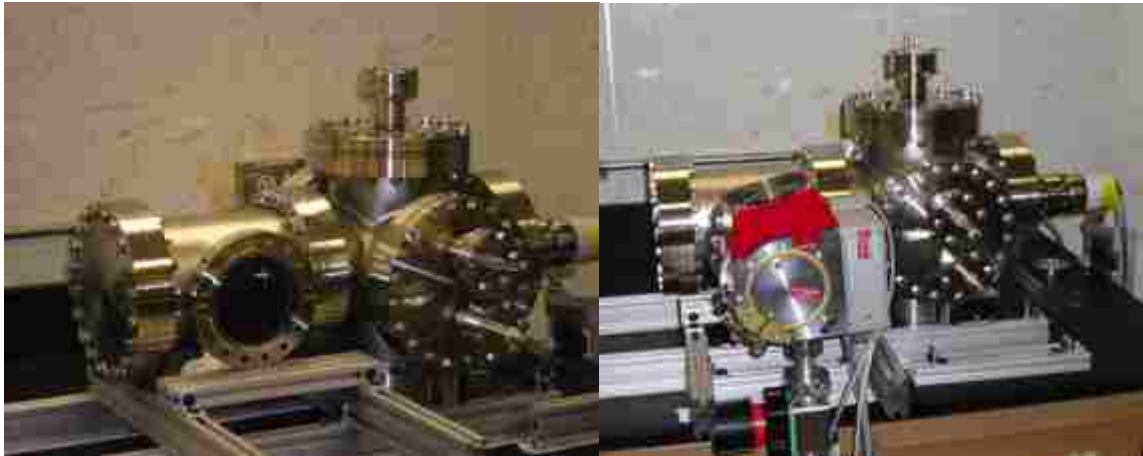
Figure 10: GEANT4 simulated TOF results

3.2 Chamber Design

The initial consideration when building the single-module coincidence unit was the vacuum vessel and equipment needed to maintain adequate pressures through the testing process. For this work, a stainless steel 6-way vacuum cross (8 inch ConFlat flange) was utilized to house the MCP and acceleration/deflection grid. Several 2.75 inch ConFlat flange half-nipples were welded on to four of the ConFlat flange flats to provide electrical/signal feedthroughs to the internal components. A straight 20 cm long stainless steel T

with 8 inch ConFlat flanges on the ends and a 6 inch ConFlat flange on the T , was connected to the cross. The 6 inch flange connects to a turbo pump.

Structural support for the unit is provided with 80/20 modular framing. Figure 11 a & b show the external chamber construction.



a)

b)

Figure 11: a) External view of the experimental chamber b) Turbo pump connected to the experimental chamber

A Pfeiffer brand pumping station, with a turbo pump and an oil free backing pump, were used to maintain the system at the 7.5×10^{-5} millitorr level required for MCP operation and for a long mean free path for the ions.

3.3 Detectors

The Hamamatsu F9890-11 micro-channel plate detector gives the signal for our timing measurements and will be the focus of the following sub-section. General properties and operation of the microchannel plate are investigated and reported, as well as initial characterization tests. A concise description of the Canberra A-450-20-AM surface barrier detector is given, but the surface barrier

detector was used primarily for the coincidence measurement of alpha particles and will not be covered in-depth due to its lack of presence in the final product.

3.3.1 Microchannel Plate Detector

Microchannel plates work on the principal of charge multiplication similar to photomultiplier tubes. Unlike photomultiplier tubes, the multi-channel plate consists of an array of millions of individual, very small (6 to 25 μm in diameter, 0.24 to 1 mm in length [Hamamatsu, 2001]), cylindrical glass capillaries fused together in the shape of a thin disc or rectangular plate to supply the charge amplification.

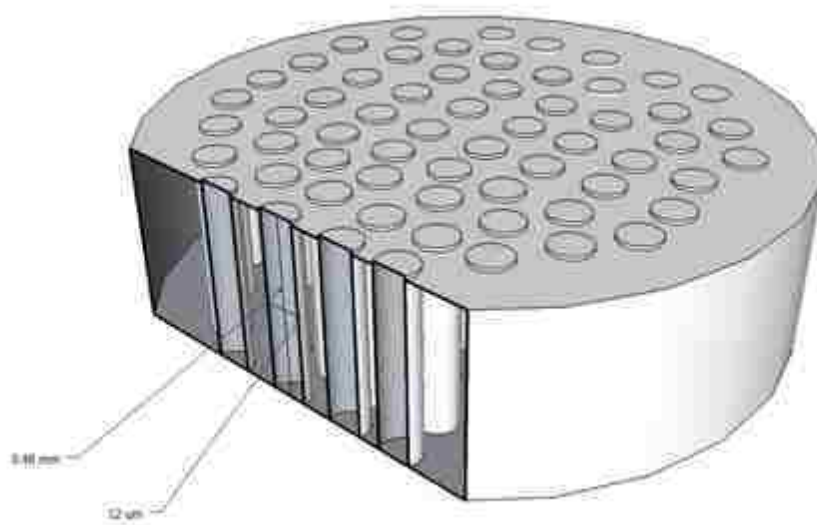


Figure 12: Illustrates a simplified MCP

These detectors are primarily used for charged particle detection; however, they are also sensitive to UV and X-ray radiation.

MCP detectors have a very desirable timing resolution due to the short pulse width (~100 ps) as well as a well-defined 1 and 2-dimensional spatial resolution utilizing discrete multiple anodes or phosphor screen imaging (~40 to 120 μm) [Hamamatsu, 2001]. Project collaborators on the related SPIDER project at LANL use large area MCPs employing spatial resolution to correct for differences in travel length for different lateral positions, though the MCPs in this work do not employ position sensitivity as we have a smaller acceptance and thus lower position uncertainty. The high electron sensitivity and fast pulse makes MCP ideal for high-resolution TOF measurements in fission fragment identification.

3.3.1.1 Construction and Operating Principles

The channels of the MCP are constructed individually and bundled together to form a dense hexagonal array of millions of separately insulated lead glass channels. Each channel acts as an individual charge multiplier. The incoming, primary radiation strikes the surface of an individual channel, subsequently releasing secondary electrons from the channel surface based on the energy of the primary radiation. Ni-Cr or Inconel depositions on the input and output surfaces of the MCP serve as the electrodes to accelerate the secondary electrons along a parabolic path produced by the primary radiation to induce further secondary electron emission as it interacts with the channel walls [Wiza, Hamamatsu].

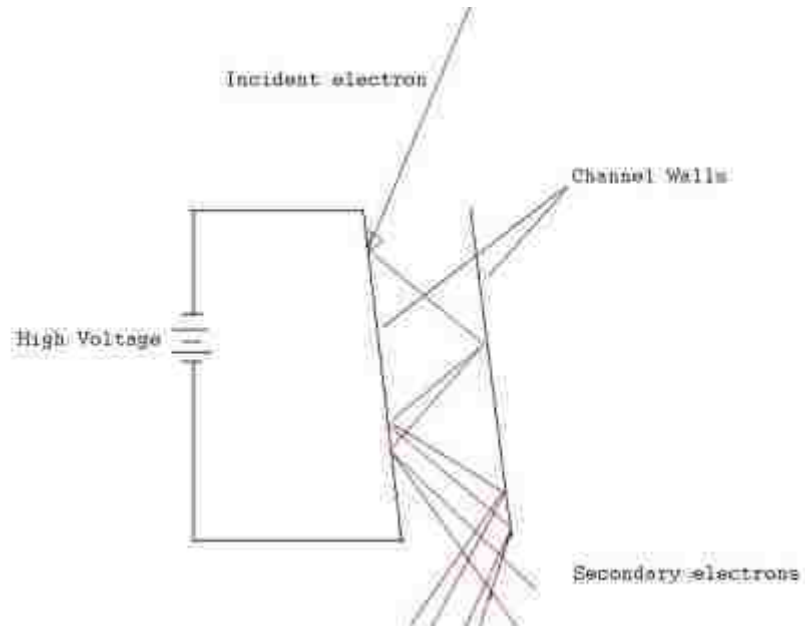


Figure 13: Charge multiplication within a single channel of the MCP

The overall gain, g , of the MCP can be written as a function of both the secondary emission characteristics of the channel wall material called the gain factor, G ($\sim 0.3-0.5$), and the length-to-diameter ratio, α , of the channel ($\alpha = l/d$) given by [Hamamatsu, Wiza]:

$$g = \exp (G * \alpha) \quad [\text{Eq. 19}]$$

Gain characteristics for MCPs as a function of applied voltage is shown in Figure 14 for various length-to-diameter ratios.

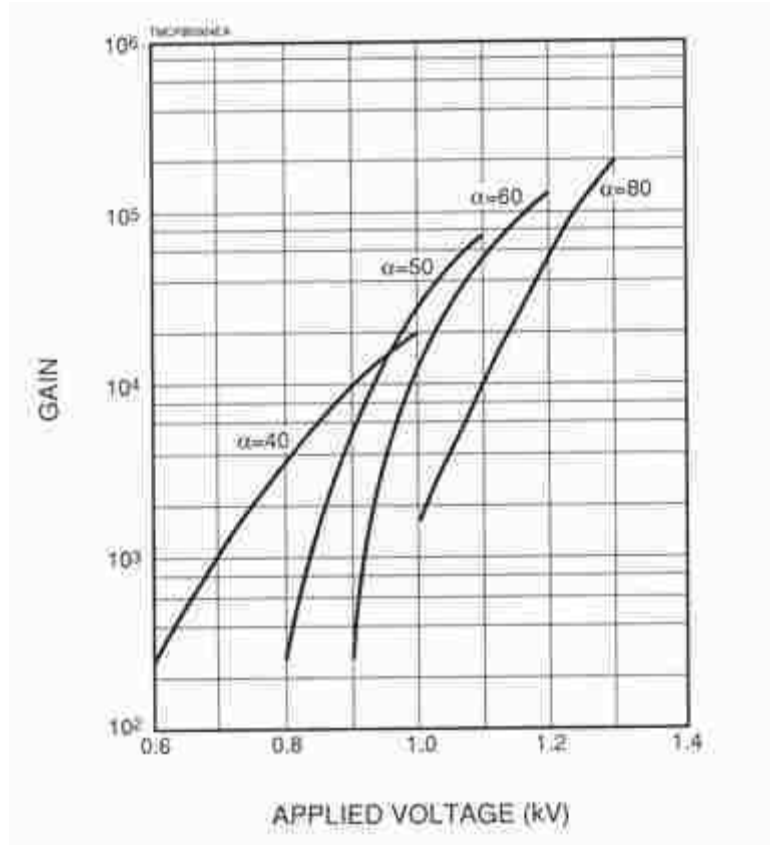


Figure 14: MCP gain as a function of voltage for various length-to-diameter values [Hamamatsu, 2001]

Manufactured length-to-diameter ratios vary from 40 – 100 producing a gain of $10^5 - 10^5$ for a single plate with an applied voltage of 1000V. Gains larger than 10^4 suffer from an increase in noise due to ion feedback [Hamamatsu, 2001]. The ion feedback, an undesired effect for this application, arises from the high charge density near the channel output producing positive ions when electrons collide with residual gas molecules. These positive ions then cause further secondary electron emission that leads to ion after pulses [Adams, 1966].

When a higher gain is required, multiple MCPs can be placed in series to achieve gains greater than 10^4 . The placement of two MCPs in series, typically separated by 50-200 μm , is often referred to as the “Chevron” configuration, while 3 MCPs in series is referred to as a “Z-stack”. Figure 15 illustrates a typical Chevron configuration of MCPs.

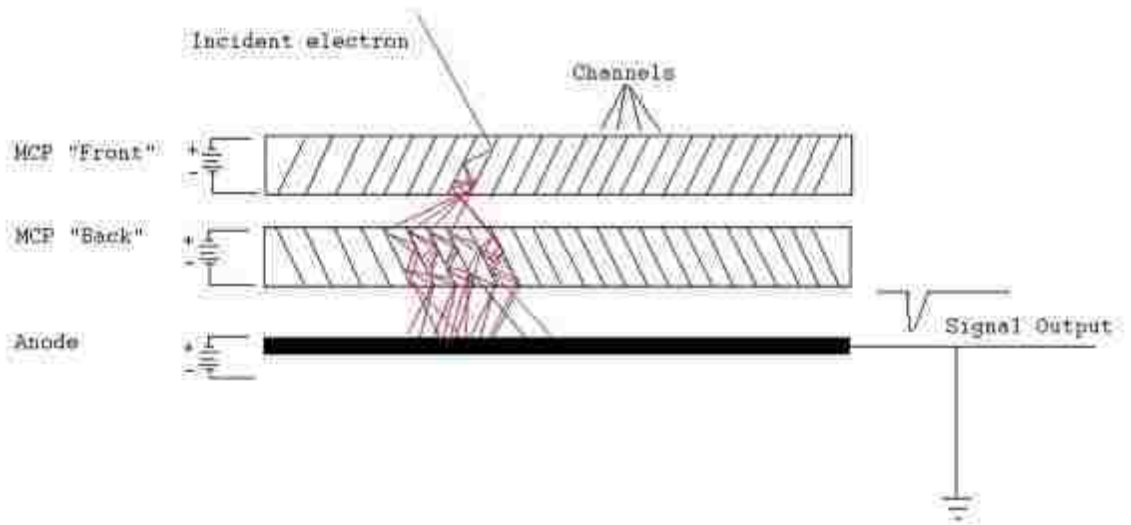


Figure 15: Chevron configuration of two MCPs placed in series [Wiza, 1979]

In the Chevron configuration, the channels are typically biased at an angle of 5° - 15° from the normal of the plate face in an attempt to limit ion feedback as well as increasing sensitivity to the incident radiation normal to the MCP surface [Hamamatsu, 2001].

Ion feedback in the chevron configuration is diminished due to the large directional change prohibiting positive ions created near proximity of the exit of the first plate from impacting the entrance of the second plate [Kosev, 2007].

Chevron configured MCPs also exhibit charge saturation at gain values of $\sim 10^7$. This is primarily due to the inter-plate bias voltage preventing the radial spread of the space-charge cloud exiting the single excited channel, which results in fewer channels being excited in the second plate. As a result, the excited channels experience an increase in the probability of space-charge saturation due to the increased electron impact energy [Kosev, 2007]. This is a desirable effect as it narrows the pulse height distribution FWHM to as much as 60% for a 3-stage MCP. The FWHM expressed as a percentage, is simply the ratio of the FWHM/peak-position channel ratio. Figure 16 shows the gain characteristics of a single stage MCP, Chevron configured MCPs and Z-stack MCPs as well as the peaked pulse height distributions from Chevron and Z-stack configured MCPs.

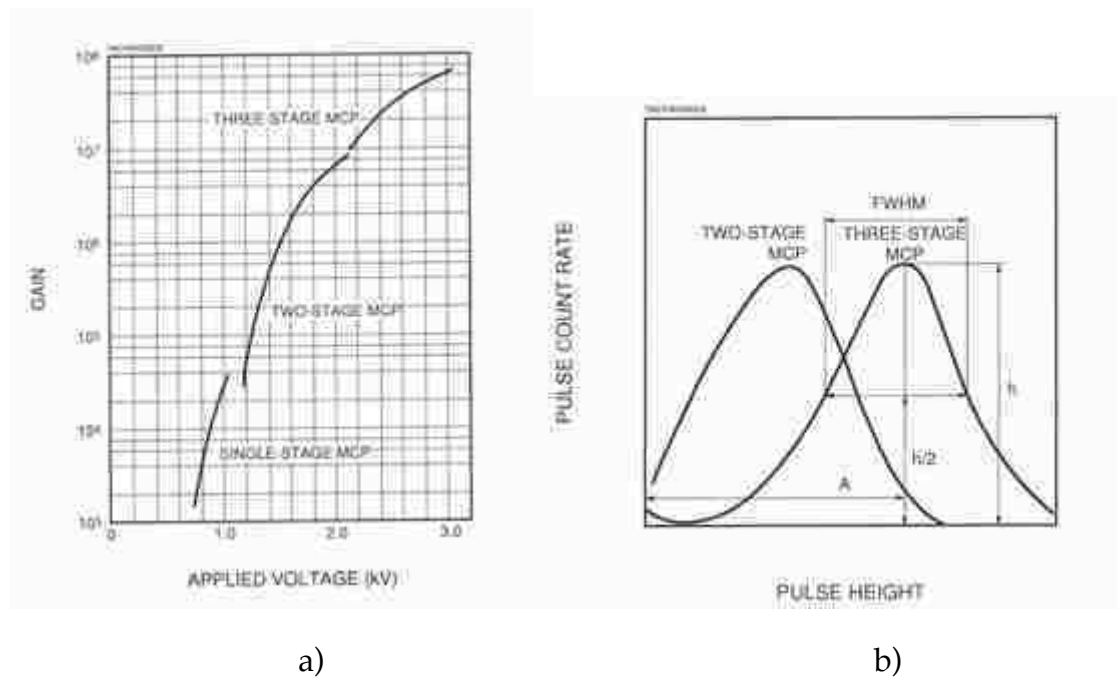


Figure 16: Gain characteristics of single and multi-stage MCP configurations and pulse height distributions [Hamamatsu, 2001]

Many pulse processing methods benefit from consistent pulse amplitudes, such as decreasing discriminator walk. Table 1 shows the expected pulse height distribution (FWHM), gain characteristics of single and multi-stage MCPs with varying length-to-diameter ratios and maximum applied voltage.

Configuration	l/d ratio	Maximum Voltage (V)	Gain	Pulse Height (FWHM%)
Single-stage	40	1000	$> 4 \times 10^3$	N/A
	60	1200	$> 1 \times 10^4$	N/A
Chevron	40	2000	$> 4 \times 10^6$	$< 175\%$
	60	2400	$> 1 \times 10^7$	$< 100\%$
Z-Stack	40	3000	$> 3 \times 10^7$	$< 120\%$
	60	3600	$> 2 \times 10^8$	$< 60\%$

Table 1: MCP gain characteristics as a function of l/d and applied voltage

[Kosev, 2007]

3.3.1.2 Gain Limiting Mechanisms

At gains higher than 10^8 in a single plate, the pulse height distribution changes from a negative exponential distribution to a quasi-Gaussian shape with a full-width-half-maximum (FWHM) of 50% or better [Schmidt, 1966]. This phenomenon is primarily the result of space-charge effects near the exit of the multiplier channel. Space-charge effects on gain limitations in straight channel multipliers were investigated extensively by Adams and Manely at the Bendix Corporation in the U.K. [Adams, 1966]. Their work focused on the relation between space charge density and the electron transit time. When the gain reaches a high value, the space-charge density near the channel exit becomes large enough to decrease the kinetic energy of the electrons impacting the channel wall. This causes the secondary electron emission coefficient, δ , to drop below one and electron multiplication ceases to occur. The space-charge density

is a dynamic quantity and as the multiplication drops below unity, the space-charge density also decreases, causing an increase in the impacting electron kinetic energy, increasing the δ value [Schmidt, 1966]. This feedback allows for a state of equilibrium or charge saturation to occur at gains approaching 10^8 . Operating the MCP in charge saturated mode leads to desirable effects on the current pulses for pulse processing schemes seen in the experiments performed by Schmidt and Hendee [Schmidt, 1966]. MCPs suffer from discriminator walk due to the large amplitude differences in pulse output. Operating in charge saturation mode helps to lessen discriminator walk that leads to inaccuracies in timing measurements.

3.3.1.3 MCP Detection Efficiency

MCP detectors have been used in a multitude of scientific applications. This is primarily due to their stable performance and reliability [Wiza, 1979], however it is also due to the MCP being sensitive to various types of radiation. Table 2 gives MCP detection efficiencies for various types of radiation.

Radiation Type	Energy/Wavelength	Detection Efficiency (%)
Electron	0.2 keV to 2 keV	50 - 85
	2 keV to 50 keV	10 - 60
Ion	0.5 keV to 2 keV	5 - 58
	2 keV to 50 keV	60 - 85
	50 keV to 200 keV	4 - 60
UV	300 Å to 1100 Å	5 - 15
	1100 Å to 1500 Å	1 - 5
X-Ray	0.12 Å to 0.2 Å	up to 1
	2 Å to 50 Å	5 - 15
High E Particles (ρ, π)	1 GeV to 10 GeV	up to 95
Neutron	2.5 MeV to 14 MeV	0.14 - 0.64

Table 2: MCP detection efficiencies for different radiation [Wiza, 1979]

The reported efficiencies are not absolute as the efficiency is also a function of the angle of the incident radiation normal to the surface of the MCP.

For this work, the primary concern is how the MCP responds to electrons. Electron detection efficiency reaches a maximum (~60-80%) with input electron energy around 500 eV to 1 keV [Hamamatsu, 2001]. With electrons below 1 keV kinetic energy, the efficiency is roughly equivalent to the Open Area Ratio (OAR), which is the ratio of the effective detection area and the total area of the MCP face. Typically the OAR value is manufactured to be around 60%, however, the OAR can be increased to 70% to 80% by etching the glass channel walls on the input side of the MCP plate [Hamamatsu, 2001]. Figure 17 shows a plot of the MCP detection efficiency as a function of input electron energy.

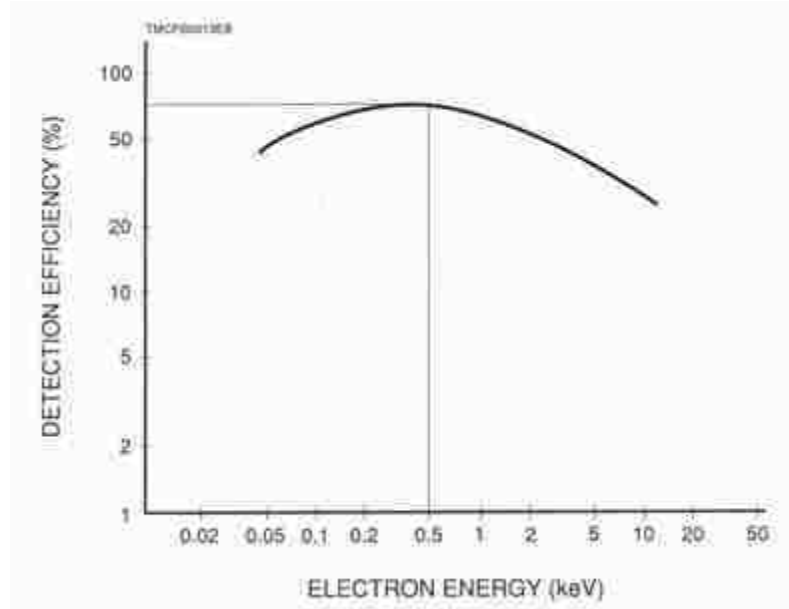


Figure 17: Electron detection efficiency as a function of energy [Hamamatsu, 2001]

Another variable to consider in the efficiency calculation is the MCP sensitivity to the angle of the primary electron. At lower energies, 500 eV to 1 keV, the optimum angle measured normal to the MCP surface was found to be $\sim 13^\circ$ [Hamamatsu, 2001] and so MCP channels are set to about 13 degrees from the surface normal, maximizing efficiency for electrons coming straight down. An angular spread in electrons to the MCP thus decreases efficiency. As the input angle becomes very sharp, the probability of interaction drops sharply as the electrons traverse parallel to the channel axis. With electron energies greater than 1 keV, the incident angle has less of an effect as the electrons striking the MCP face have an increased probability of creating secondary electrons that can, in turn, excite the neighboring channels [Kosev, 2007]. Figure 18 shows a plot of

the probability of interaction of primary electrons, in the 500 eV to 1 keV energy range, as a function of the incident electron angle to the MCP channel.

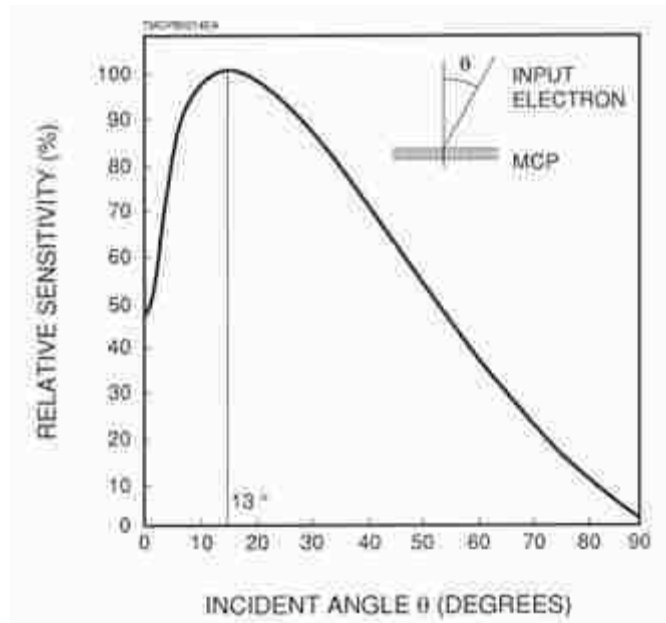


Figure 18: MCP sensitivity to 500 eV to 1 keV primary electrons as a function of incident electron and channel [Hamamatsu, 2001]

3.3.1.4 MCP Time Response

The superior timing characteristics exhibited by an MCP are primarily due to the shortened electron transit time in the very small channel volume compared to transit between discrete dynodes utilized in the more conventional photomultiplier tube (PMT). The signal transit time is proportional to the channel diameter; improvement in time resolution can be obtained as the diameter of the channel decreases [Hamamatsu, 2001]. Figure 19 illustrates a typical signal from a Hamamatsu F-9890-12 fast response MCP.

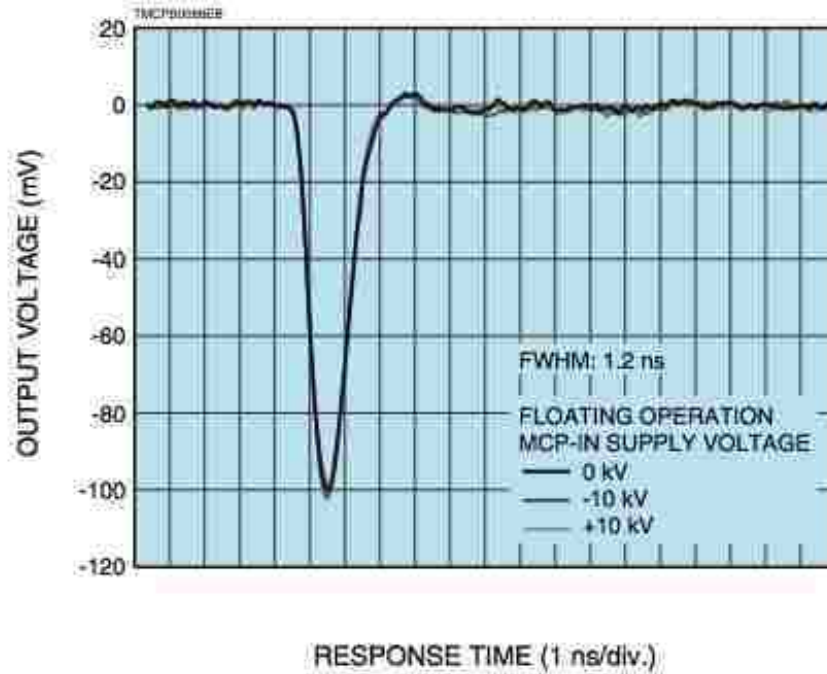


Figure 19: Typical output signal from a fast response MCP [Hamamatsu, 2001]

The Hamamatsu F-9890-12 MCP has a similar configuration to the F-9890-11 used in this work. The F-9890-12 has a channel diameter of 6 μm giving a signal width of 1.2 ns FWHM. We are using the F-9890-11 with a channel diameter of 12 microns.

3.3.2 Hamamatsu F-9890-11

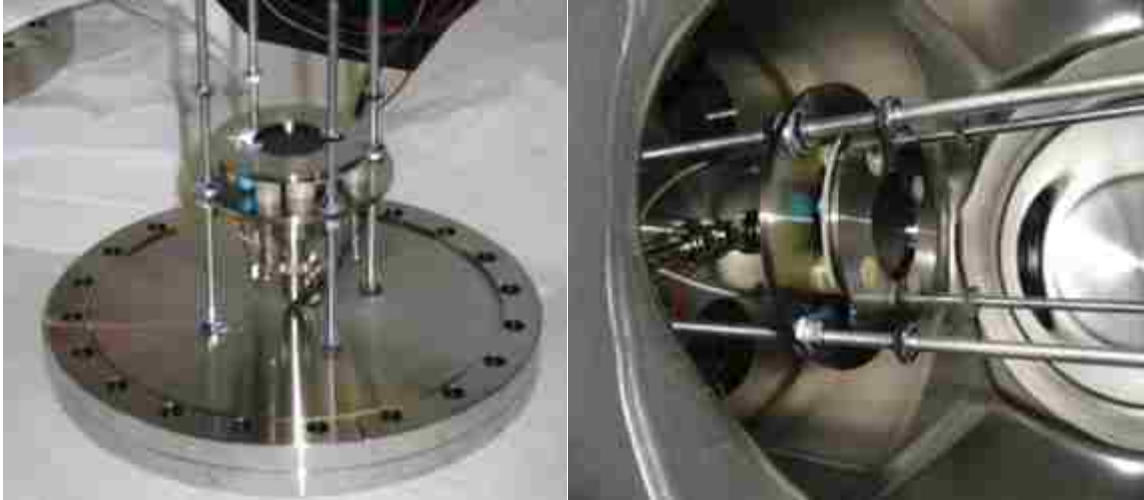
The Hamamatsu F-9890-11 MCP utilized in the single module coincidence experiments is a fast-timing, non-position sensitive MCP, ideal for time-of-flight measurements. Table 3 gives the specifications for the Hamamatsu F9890-11.

Parameter	Quantity	Unit
Channel Diameter	12	μm
Bias Angle	12	degree
Effective Diameter	27	mm
Number of MCPs	2	-
Gain	1×10^6	-
Plate Resistance	10 to 40	$\text{M}\Omega$
Dark Count	3	$\text{s}^{-1} \text{cm}^{-2}$
Pulse Width (FWHM)	0.9	ns
ΔV Between Plates	2	kV
ΔV MCP-Out & Anode	0.5	kV
Max MCP-In Bias	10	kV
Operating Pressure	$< 1 \times 10^{-3}$	mTorr

Table 3: Specifications for the Hamamatsu F-9890-11

3.3.2.1 F-9890-11 Set-up & Installation

The F-9890-11 MCP was installed on the vacuum side of an 8 inch ConFlat flange and supported by four 8-32, steel threaded rods. The MCP is held in place by nuts and lock washers measured equidistant from the surface of the ConFlat flange. Small slits were cut at the base of the steel threaded rods to prevent “virtual leaks” of trapped gas from the tapped holes below the rods. Figures 20 a & b show the MCP support structure on the ConFlat flange and installation in the six-way cross.



a)

b)

Figure 20: a) MCP support setup b) MCP installed on its side, inside the six-way cross

For precautionary reasons, the flange holding the MCP is installed on a side port of the six-way cross to avoid any accidental damage to the thin glass MCP due to falling objects during installation (washers, nuts, screws etc.).

The ConFlat flange used to support the MCP has been modified to provide bias and signal feedthroughs. The voltage supply and signal feedthroughs go through two, 2.75 inch half-nipples welded to an 8 inch ConFlat flange flat. The bias feedthrough consists of four pins, with each pin having a voltage rating of 5 kV and an amperage rating of 1 A. The signal feedthrough is a grounded, double-ended BNC connection type. Figure 21 shows an external view of the MCP experimental setup.

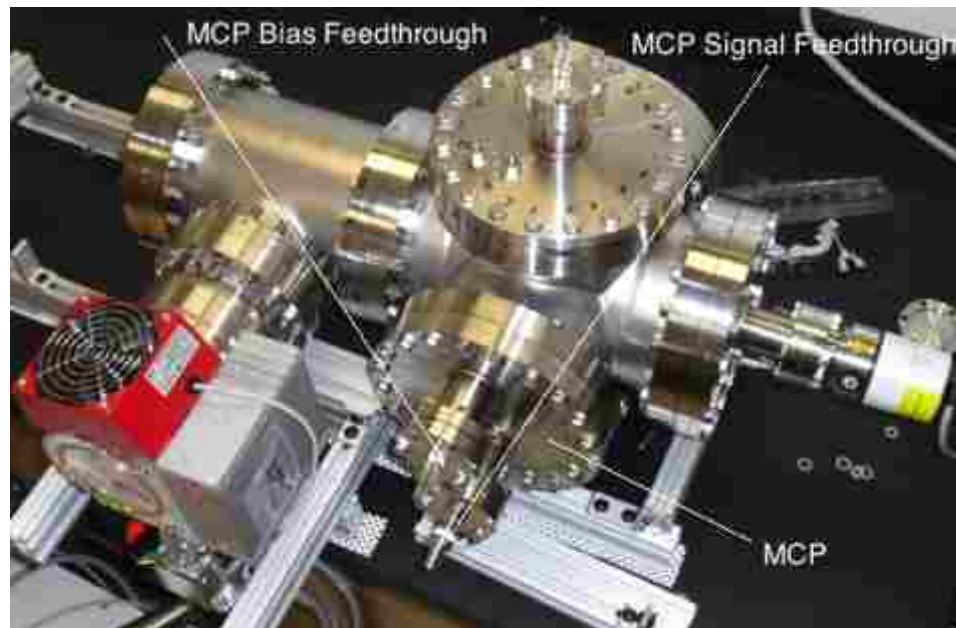


Figure 21: External view of the MCP experimental setup

Voltage is supplied to the MCP via an ORTEC 456 power supply rated for ± 3 kV, 0-10 mA. A voltage divider circuit provides bias to each MCP stage, defined as “MCP Front or MCP-in” and “MCP Back or MCP-out”, and the anode by a simple voltage division circuit. See figure 15 for a voltage diagram of the MCP. MCP-in voltage is applied to the top of the diagram, MCP-out to the bottom of the lowest MCP plate, and anode voltage to the top of the anode. The output is tied near ground by a resistor (not shown) and is connected to the anode via a capacitor (not shown).

After sealing the ConFlat, the chamber is brought to appropriate vacuum conditions, $\sim 7.5 \times 10^{-5}$ mtorr, with the Pfeiffer roughing/ turbo pump and held for roughly 24 hours before applying voltage to the MCP [Hamamatsu, 2001]. Table

4 gives typical operating voltages for each charged component based on incident particle type.

Component	Ion or Photon	Electron Detection	This Work
MCP-In	- 2400 V	+ 300 V	+ 271 V
MCP-Out	0 V	+ 2700 V	+ 1938 V
Anode	+ 150 V	+ 2850 V	+ 2200 V

Table 4: MCP voltage for ion/photon & electron detection modes [Roentdek, 2013]

The Hamamatsu F-9890-11 has a limit of 2 kV difference between MCP-in and MCP-out and a limit of 500 V between MCP-out, from which the signal is read, and the collection anode. MCP-out is connected to the anode via a capacitor to allow flexibility in anode biasing. Great care must be taken to ensure these limits are not exceeded as an electrical discharge within the plates can result in permanent damage to the MCP. This was the primary reason behind initially operating with a voltage difference of 1667 V between MCP-in/MCP-out and 262 V between MCP-out and anode.

3.3.2.2 F-9890-11 Characterization

Before installing the acceleration and reflection grids, the electron optics, for the coincidence measurements, it is useful to determine the operating characteristics of the MCP. Starting from a conservative bias voltage of 2200 V, the bias was increased at 100 V intervals up to 2600 V to analyze the F-9890-11 raw signal time characteristics and pulse height distribution. Table 5 gives a synopsis of the bias

voltages, voltage to each component of the MCP and voltage potential between components for several test runs.

Bias Voltage	MCP-In	MCP-Out	Anode	ΔV MCP-in/MCP-out	ΔV MCP-out/Anode
+ 2200 V	+ 271 V	+ 1938 V	+ 2200 V	1667 V	262 V
+ 2300 V	+ 283 V	+ 2016 V	+ 2300 V	1733 V	284 V
+ 2400 V	+ 296 V	+ 2103 V	+ 2400 V	1807 V	297 V
+ 2500 V	+ 308 V	+ 2191 V	+ 2500 V	1883 V	309 V
+ 2600 V	+ 320 V	+ 2279 V	+ 2600 V	1959 V	321 V

Table 5: Test operating voltages for the F-9890-11 MCP

3.3.2.3 F-9890-11 Time Response

A Techtronix TDS 2024B 200 MHz 2 GS/s 4-channel oscilloscope was utilized to analyze the raw signal from the MCP. The MCP signal time characteristics are expected to be unchanged with varying voltage potentials. The time characteristics are primarily governed by the diameter of the individual channel multipliers. Figure 22 shows that the time characteristics of the output pulse remain relatively unaffected by changes in the voltage potentials.

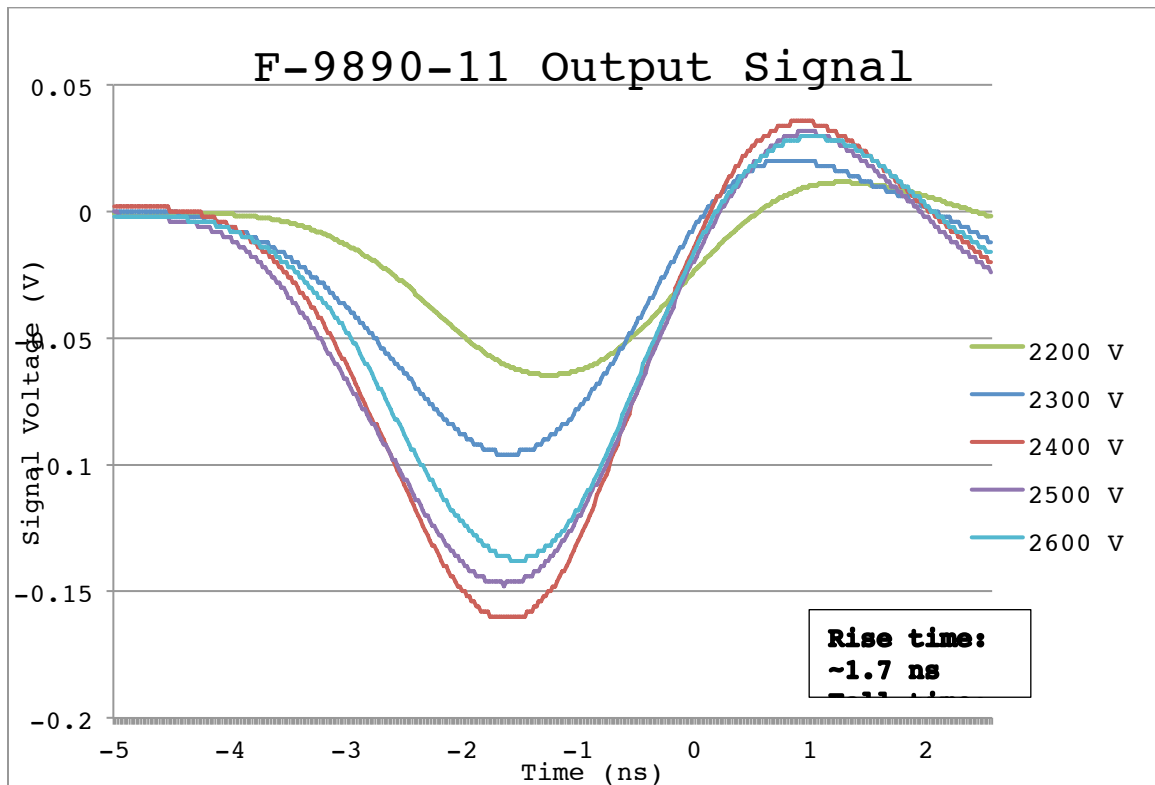


Figure 22: MCP output signal at varied voltage potentials

The signal rise time and fall time was calculated by subtracting the time measured at 90% maximum signal peak height from the time measured at 10% maximum peak height. The F-9890-11 output signal, regardless of voltage potentials, has a characteristic rise time of 1.7 ns, fall time of 1.1 ns and FWHM of 2.2 ns. There is significant ringing in the raw signal, which may be due to impedance mismatch, however the amplitude of the signal ring is roughly 20% of the peak height of the original signal and can be discriminated out to eliminate the false triggering in a pulse-processing scheme. The signal settling time is found to be roughly 35 ns. Figure 23 shows an example of the ringing experienced with the F-9890-11

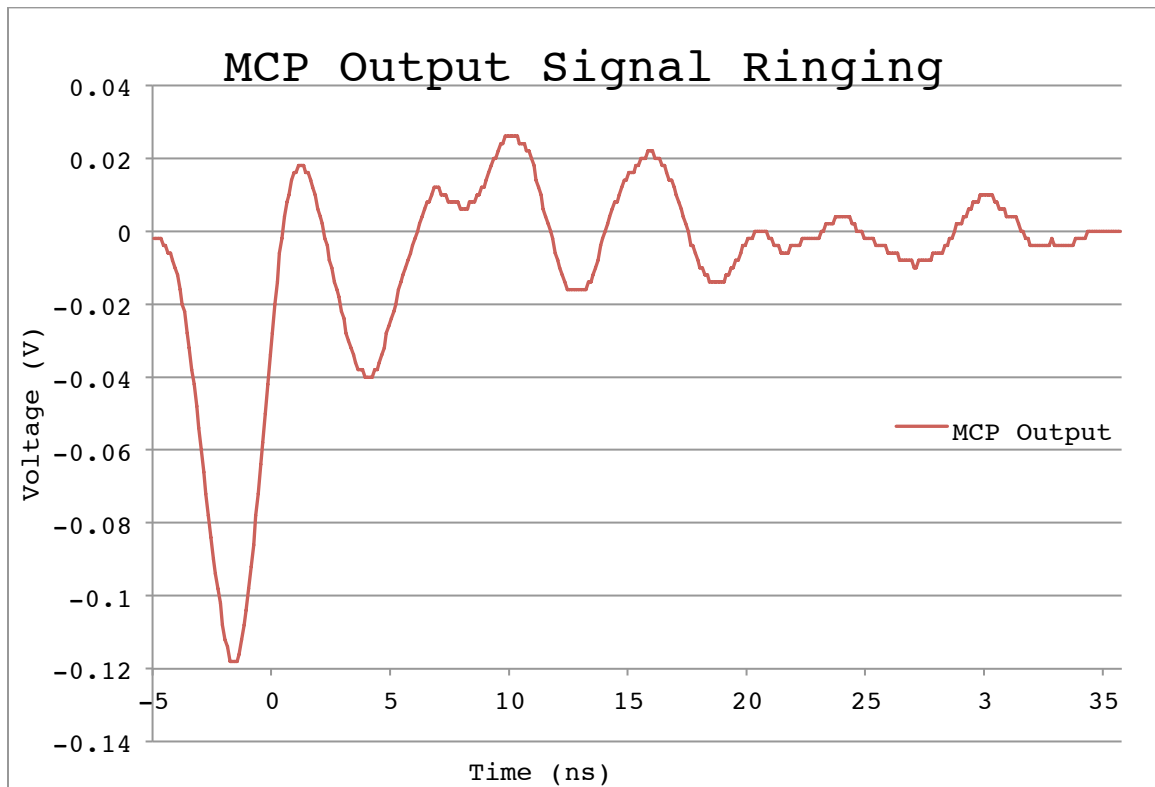


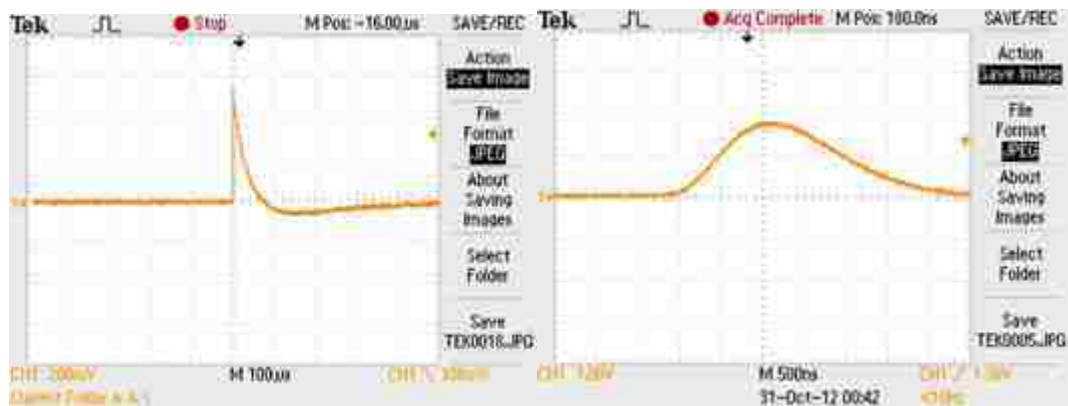
Figure 23: F-9890-11 output signal at a bias voltage of 2200V. The output pulse settles to baseline after ~35 ns.

3.3.2.4 F-9890-11 Pulse Height Distribution & Charge Saturation

The pulse height distribution of the MCP becomes important for discriminator settings in coincidence measurements. It is often beneficial to operate the MCP in charge saturation mode as a threshold discriminator can be used to filter out low-level noise. Measurements for the pulse height distributions were performed at the same bias voltages as the time response measurements in the previous section. The F-9890-11 output signal is pre-amplified by the ORTEC 109PC charge-sensitive pre-amplifier with further amplification utilizing the ORTEC 590A amplifier. The amplified analog signal is then converted to digital in the

analog-to-digital converter (ADC) of the ORTEC EasyMCA multichannel analyzer to histogram the pulse height distribution.

Viewing the signal up to the pre-amplifier, the ringing phenomenon in the raw signal is discriminated out by means of a low-pass filter in the pulse shaping stage of the pre-amplifier. The signal is inverted to provide the multichannel analyzer with a positive input signal. The pre-amplifier signal experiences overshoot due to amplifier characteristics as the pre-amplifier is set to return to baseline quickly to allow for high rates. This fast pulse is to be used for sharp timing measurements. For pulse height distribution characterization, a slower, ORTEC 590A amplifier is used on the pre-amplified signal to provide a semi-Gaussian signal to the multichannel analyzer to lower the signal-to-noise ratio and allow easy digitization. Unipolar, semi-Gaussian pulse-shaping amplifiers are normally the optimum choice for energy spectroscopy [ORTEC, 2010a]. Figures 24 a and b show the output pulses from the 109PC pre-amplifier and 590A amplifier.



a)

b)

Figure 24: a) 109PC pre-amplifier signal and b) 590A amplifier signal

Even though the MCP pulse height does not give any energy information about the incident electrons, it is useful to analyze the pulse height distribution to determine the optimum threshold discrimination threshold to remove random events from electrons originating in the MCP itself. As mentioned in section 4.2.1.2, for coincidence measurements and pulse-processing schemes it is often beneficial to operate the MCP in charge saturated mode to be able to better discriminate the real signal from the noise in the system. The pulse height distribution was obtained for the F-9890-11 utilizing the same 100 V increments on the operating bias used in the time response analysis from 2200 V to 2600 V. Figure 25 shows the results of the pulse height distribution at the various bias voltages.

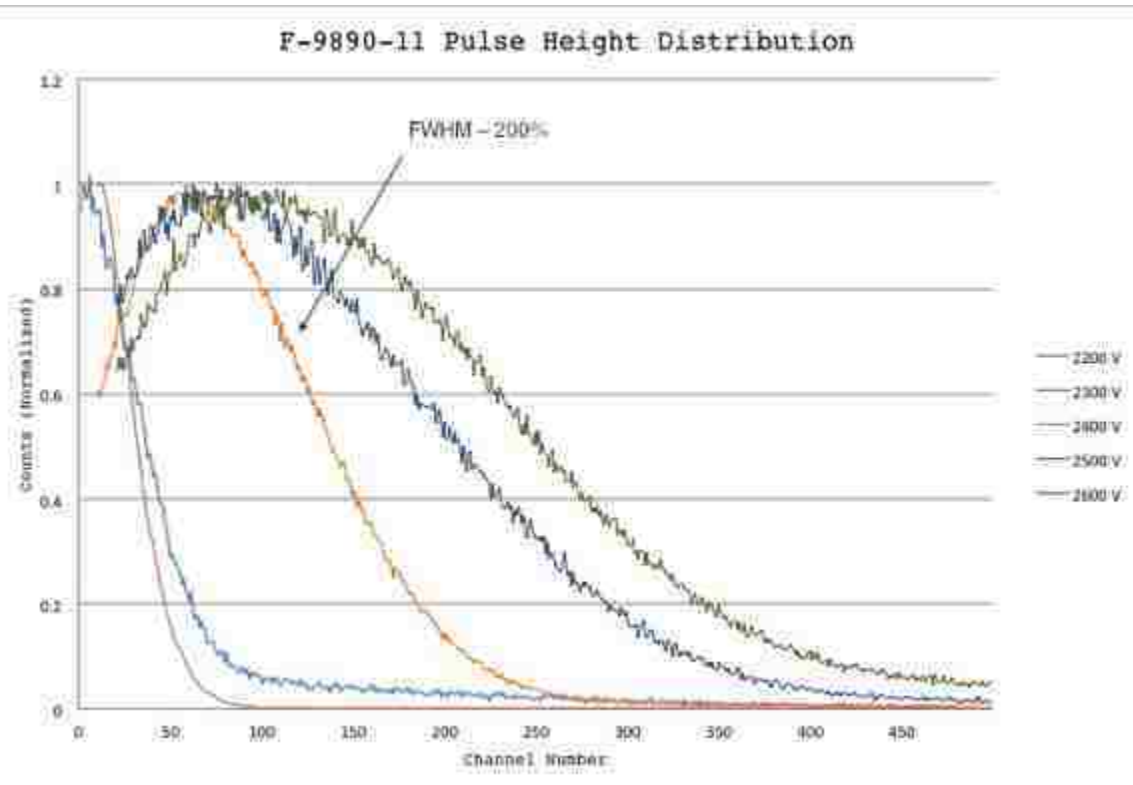


Figure 25: Pulse height distribution for the Hamamatsu F-9890-11 MCP

From Figure 25, charge saturation of the MCPs begins to occur at a bias voltage of 2400 V. As the bias voltage increases past 2400 V, the FWHM of the pulse height distribution begin to increase. Operating the MCP at a bias voltage of 2200-2400 V should allow for proper threshold discrimination for timing measurements to decrease inaccuracies due to discriminator walk.

3.3.3 Passivated Implanted Planer Silicon (PIPS) Detector

For initial timing coincidence measurements, an alpha particle source was used for the ion beam. The alpha particles passed through a foil, knocking out electrons that were used to produce an MCP timing signal, and into an alpha detector, used to produce the second timing signal. For detection of the α -particle, A Canberra A-450-20-AM passivated implanted planer silicon (PIPS) detector is used. The PIPS detector offers several advantages to the standard silicon surface barrier (SSB) and diffused junction (DJ) detectors [Canberra, 2012].

1. Contacts are ion implanted to form precise, thin, abrupt junctions for improved resolution.
2. Entrance window is stable and rugged for easy cleaning.
3. Leakage current is up to 1/ 100 of a typical SSB or DJ detectors.
4. Window thickness is less than comparable SSB and DJ detectors.

The window thickness is especially important to close detector-source experiments using low-level α -particle sources. Some α -particles will enter at large angles and experience greater energy straggling in the window, contributing to resolution broadening; this then is less of a concern with the thin

window PIPS detector. Table 6 shows the detection characteristics of the Canberra A-450-20-AM PIPS detector [Canberra, 2012].

Parameter	Quantity	Unit
Active Area	450	mm
Alpha Resolution	20	keV
Energy Detection Range	3 to 8	MeV
Background	6	counts/day
Window Thickness	500	Å (equiv. Si)
Operating Voltage	40	V

Table 6: Summary of the A-450-20-AM PIPS detector characteristics

The PIPS detector served as the alpha particle detector for the single module coincidence measurements discussed in chapter 4.

3.4 Single Module Construction

The TOF spectrometer consists of two modules, each consisting of a detector and ion optics electrodes. Both together give a start and stop time, or “time 1” and “time 2”. Before constructing the entire single-arm fission fragment spectrometer, the “time 1” detector or “single module” was built and tested to determine its individual properties. The construction of the single module consists of three main parts:

1. Design and construction of the acceleration/reflection grids.
2. Design and construction of the structural support or “housing”.
3. Design and construction of support for the conversion foil.

3.4.1 Material selection

The ion beam and the electrons require high vacuum to travel unperturbed, and the MCP detectors require high vacuum to function without arcing. Thus, it is important to choose materials for the acceleration/reflection grids and structural housing that exhibit low outgassing characteristics. Non-volatile substances such as hydrocarbons and oils that are often emitted from some plastics during the pump down process can implant on the MCP input and channel surface, leading to degradation in the secondary electron yield [NASA, 2013]. Volatile compounds like water vapor pose the greatest risk. Water vapor presented into the system can lead to spurious electrical breakdown causing permanent damage to the MCP. For this work, it is also important for the material chosen to be rigid and lightweight, as they will be installed on their side and are subject to vibration (from the turbo pump) and gravity that can create position line-up issues over time. It is also useful for the grid material to be insulated to avoid potential electrical contact with the metal vacuum chamber.

Utilizing the NASA outgassing database [NASA, 2013], A suitable grid and housing material was selected. G10 Garolite is a high-pressure industrial laminate made from glass fabric impregnated with epoxy resin and has been the standard for grid construction in apparatuses such as COSI-FAN-TUTTE and SPIDER. G10 Garolite is also the typical material used for printed circuit boards. A readily available, cost effective and flame retardant alternative to G10 is FR4. The only difference between G10 and FR4 is the resin used in the manufacturing process. Bromine is added to the resin composite to add heat resistance. The important outgassing quantities are conserved, with slight improvement in total

mass loss (TML) and water vapor recovered (WVR) with no added collected volatile condensable materials (CVCM). Table 7 compares the outgassing properties of G10 and FR4, showing them both to be suitable for our applications.

Material	%TML	%CVCM	%WVR
G10 Garolite	0.3	0	0.09
FR4 Garolite	0.27	0	0.05

Table 7: Comparison between G10 & FR4 outgassing properties [NASA, 2013]

Conveniently, due to its heavy use in the printed circuit board community, FR4 is readily available with thin conductive copper adhered to the surface. This is useful for the grid and foil holders as it allows proper electrical contact to be made to supply voltage to the grids and foil. The grids themselves consist of conductive, 20 μm diameter gold-plated tungsten wire, which are simply soldered to the plated FR4.

3.4.2 Reflection/Acceleration Grid Construction

A method of constructing the acceleration and reflection grids using the FR4 is described below.

3.4.2.1 FR4 Grid Frames

0.16 cm thick FR4 board with very thin (~0.25 mm) coppered surface for electrical connection was used to construct the grid frames. With a Dremel rotary tool, the FR4/copper boards were cut to the appropriate dimensions. The adhesive used to attach the copper sheeting to the FR4 is unknown and may be of some concern

regarding outgassing. To minimize this, the cooper sheeting was removed with fine grit sand paper where no electrical contact is necessary. Figure 26 shows the acceleration and reflection FR4 frames and their respective dimensions.

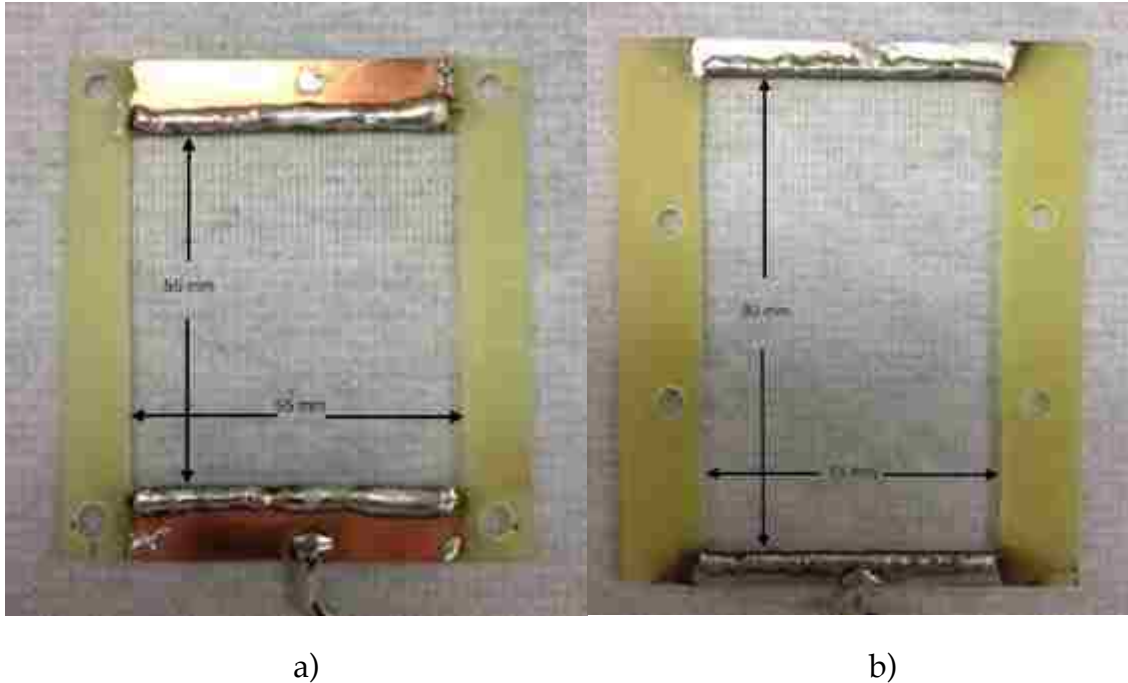


Figure 26: a) Acceleration and b) Reflection grid FR4 frame dimensions are presented

The parallel Au coated W wires for the electrodes were assembled using an in house construction technique. A frame was made to hold the wires consisting of two parallel threaded rods (wire guides) with a 1 mm pitch between threads held in place by two parallel pieces of wood, perpendicular to the threaded rods, creating a rectangular frame. The center of the frame was attached to another threaded rod with the same pitch to act as a pivot and to translate the frame one thread position per rotation. The frame was rotated to take up the wire, and with the translation matched to the outer rod threads the wire was taken up

along sequential thread positions with each rotation, creating a wire harp. A simple, manual pre-tensioner is used to keep the Au-W wire at a constant tension while it is wound about the wire guides. Figure 27 demonstrates the improvised grid construction device.



Figure 27: Au-W wire grid construction device

After winding a full grid, the ends of the wires were soldered to the parallel rods to prevent unwinding. The FR4 frame was put into position against the wires for soldering with an adjustable scissors jack. Once in place, the wires were soldered to the coppered FR4 frame using point-to-point soldering. Figure 28 shows the FR4 frame in place for soldering.



a)

b)

Figure 28: a) FR4 grid frame installation b) FR4 grid frame soldering setup

Solder is another potential source of outgassing in vacuum systems and care must be taken in the solder selection. Solder is typically lead based, however lead has a high vapor pressure and should never be used in ultra-high vacuum (UHV) environments. In this application, a silver based solder which consists of 96.5% Sn and 3.5% Ag was used to attach the Au-W wire to the coppered FR4 frame. The point-to-point soldering method introduces another possibility of outgassing as gas can become trapped in the soldering joints, however through practice and patience, this method has produced acceleration and reflection grids with minimal solder amounts and good structural contact between wire and frame. Figure 29 shows a completed acceleration grid ready for installation.

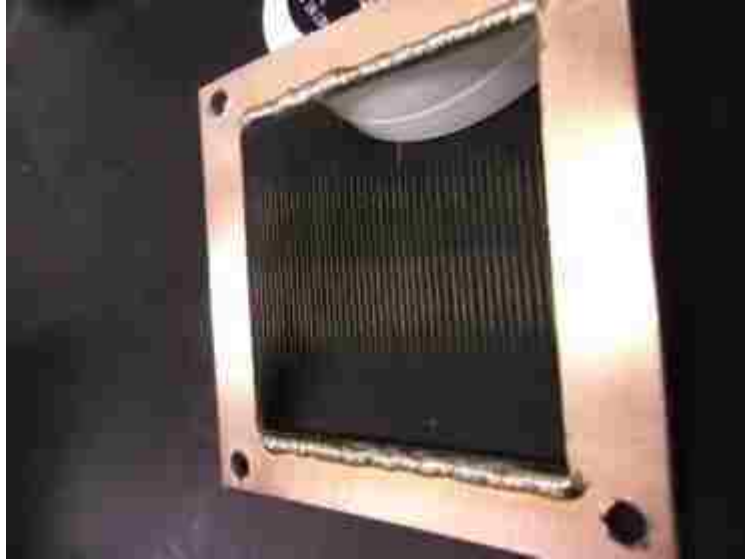


Figure 29: Au-W parallel wire array soldered to an acceleration grid frame

3.4.3 Housing

The housing for the acceleration and reflection grids serves two purposes: providing structural support and providing positional adjustment for the acceleration/reflection grids with respect to the MCP. Positioning is important for the coincidence measurements, as the coincidence efficiency is dependent upon the portion of secondary electrons from the conversion foil that impact the active area of the MCP. This is discussed in further detail in the results section.

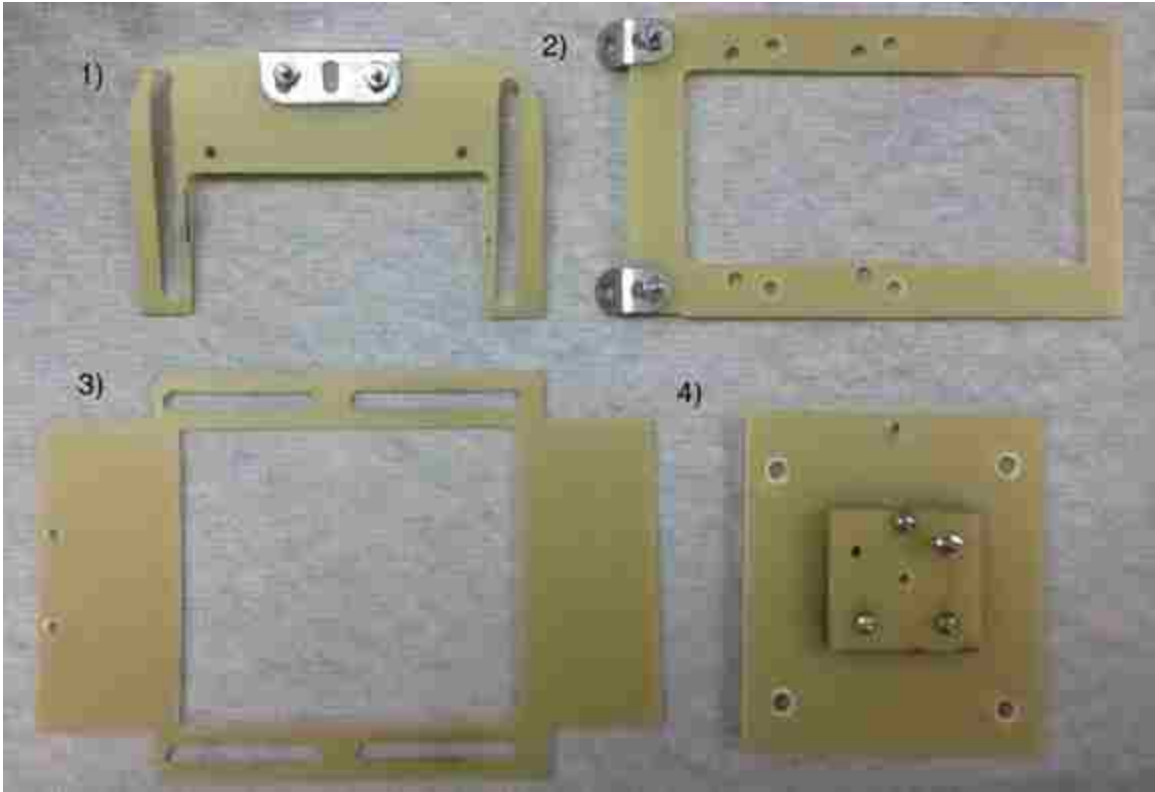


Figure 30: 1) Housing top plate. 2) Back plate, reflection grid holder. 3) Base plate. 4) Front plate, source holder/collimator.

Due to its low outgassing, rigidity, and workability, 0.16 cm thick FR4 was chosen to serve as the structural housing for the acceleration and reflection grids. The housing consists of four main components: a housing top plate, a back plate reflection grid holder, a base plate, and a front plate source holder, shown in figure 30. The assembly is shown in figure 31. The top plate and base plate are mounted to threaded rods connected to the vacuum flange. Both pieces have slots to allow for forward/backward adjustment of the secondary electron reflection grids relative to the MCP surface to optimize efficiency. The smaller steel threaded rods and nuts holding the acceleration and reflection grids in place in the primary setup shown (horizontal and diagonal rods in figure 31), are

replaced by Teflon threaded rod and Teflon nuts for electrical insulation purposes when in operation.

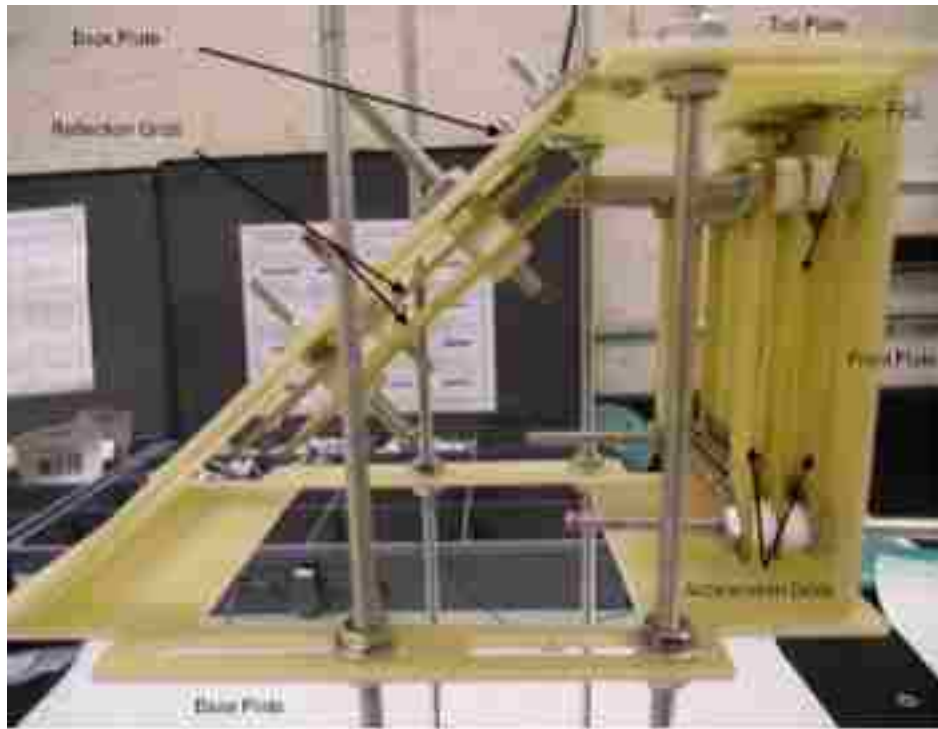


Figure 31: Housing with acceleration and reflection grids installed while dimensions are measured

After position measurements were made, the housing unit was installed into the 6-way vacuum cross. A separate circuit was built to provide the back reflection grid and carbon foil with a negative bias.

During initial power up tests of the acceleration and reflection grids, as the bias was applied to the grids approaching -2000V , the reflection grids experienced a break in a Au-W wire. High value resistors were added to the original circuit to lower the current to diagnose the problem. After the resistors were installed, the wire grids have not experienced another break, up to a bias of -3000 V applied

for up to 8 hours at a time. It is assumed that the breakage occurred due to high current joule heating combined with high mechanical tension on the wire.

The pressure of the vacuum chamber with the added single module unit was also assessed during these tests to make sure the MCP was still within its operational parameters. A pressure of 7.5×10^{-5} mtorr was measured after 20 hours of pump down time; well below the MCP operation limit of 1×10^{-3} mtorr.

3.4.4 Carbon Foil Measurements

The thin carbon conversion foils were provided to us through LANL from Oregon State University. The heavy ion passes through the foil, ejecting electrons which are then measured instead of directly measuring the heavy ion. Thickness measurements were necessary as there was uncertainty in the carbon foils supplied. It was assumed by the LANL source that the foils have a mass thickness of $100 \mu\text{g}/\text{cm}^2$. This is an important quantity to the timing and energy measurement as the energy loss of the alpha particles/fission fragments as they traverse through the carbon foil needs to be understood in the final mass calculation. Figure 32 shows the experimental setup for the carbon foil measurements.

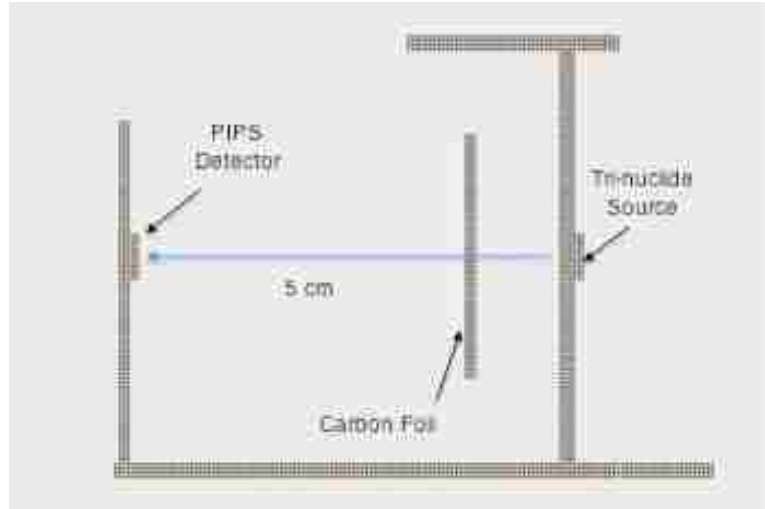


Figure 32: Experimental setup for C foil measurements

Alpha particle energy loss through the foil was used to extract the foil thickness using a tri-nuclide (^{239}Pu , ^{241}Am and ^{244}Cm) alpha source was used. The TOF module geometry was altered to perform these carbon thickness measurements. The back plate and the acceleration and reflection grids were removed from the module. The Canberra A-450-20-AM PIPS detector was added to the system attached to a rear FR4 plate, the PIPS detector is installed perpendicular to the collimated alpha particle beam. Unlike in TOF operation, the foil was not biased and there were no fields applied between the source and detector. To reduce sources of energy straggling, the system was brought down to a pressure of 7.5×10^{-5} mtorr before data was taken. Measurements were performed both with no foil, to calibrate full alpha particle energies, and with the foil in the beam path. The results of the carbon foil measurements are shown in figure 33.

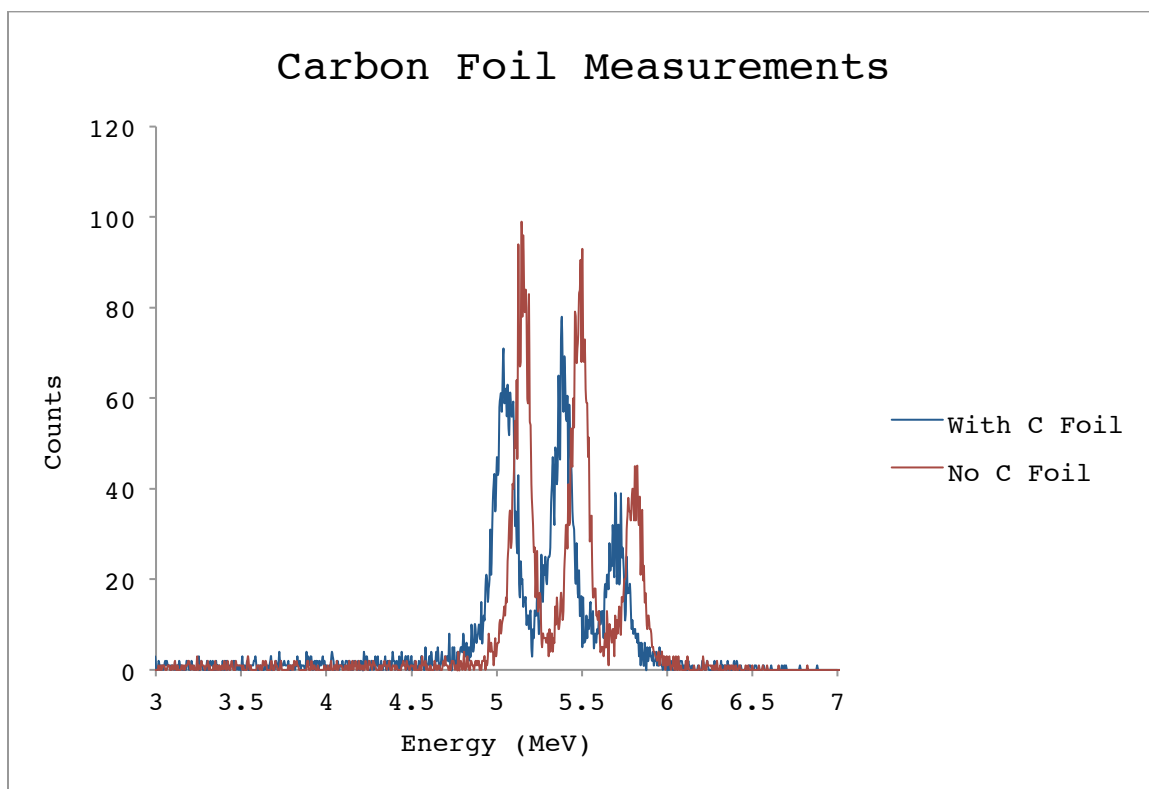


Figure 33: energy spectra measurements for the collided (with C foil) and uncollided (no C foil) setups.

An average energy loss of ~ 100 keV is seen from the three prominent alpha peaks. This is in reasonable agreement with calculated alpha particle stopping power tables [ORTEC, 2010b]. With an alpha particle energy of 5.5 MeV, the stopping power, $dE/\rho dx$, is given as $762 \text{ MeV cm}^2/\text{g}$. For a $100 \mu\text{g}/\text{cm}^2$ foil, the alpha particle should experience an energy loss of 76.2 keV. Given few alpha particles enter the foil exactly normal to the foil surface; it is not surprising the experimental energy loss is greater than the calculated loss.

As a secondary validation, simulations were performed using the Stopping and Range of Ions in Matter (SRIM) computer software package. The program was

setup with a $100 \mu\text{g}/\text{cm}^2$ ($0.44 \mu\text{m}$ thickness at a C density of $2.27 \text{g}/\text{cm}^2$) carbon layer with 10,000 primary alpha particles incident normal on the carbon layer. The most probable alpha energy for each nuclide in the tri-nuclide source was used in the simulation. The results of the simulation compared with the collided (with C foil) experimental measurement are shown in Figure 34.

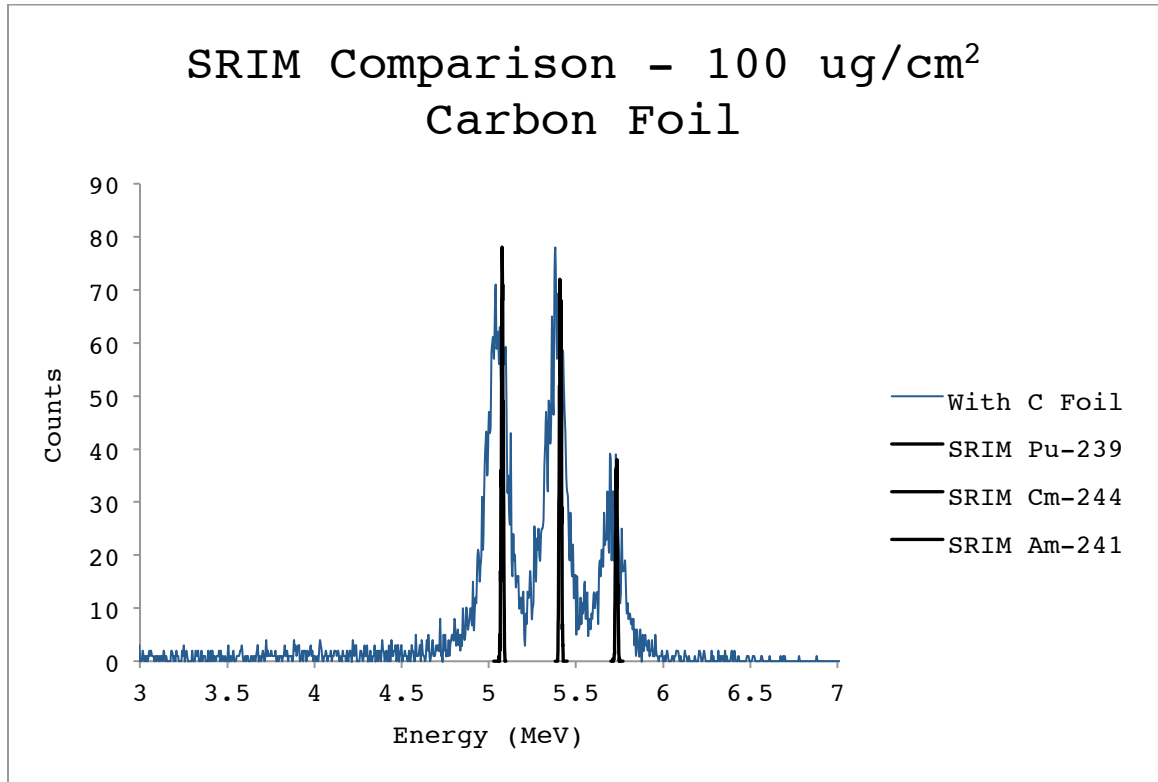


Figure 34: Comparison of simulation and experiment. Tri-nuclide alpha energy spectra through $100 \mu\text{g}/\text{cm}^2$ carbon

The SRIM calculated values form sharp peaks. Unlike for the true collimated alpha particle source, all the simulated particles incident on the carbon foil were normal to the surface. The simulation did not account for the lower probability alpha particles of differing energy from each nuclide. For the experimental results, these factors along with the inherent energy resolution of the Canberra

PIPS detector of 20 keV lead to a FWHM ~85-120 keV or 1-2% energy resolution. .
 The SRIM simulation results using a 100 $\mu\text{g}/\text{cm}^2$ carbon foil agree, within experimental resolution, with experimental results. Table 8 lists the results from experiment and simulation.

Alpha Source (Energy)	Without C Foil	With C Foil	SRIM (With C)
Pu-239 (5.156 MeV)	5.146 MeV	5.040 MeV	5.077 MeV
FWHM	86.7 keV	120.5 keV	N/A
Am-241 (5.485 MeV)	5.502 MeV	5.382 MeV	5.410 MeV
FWHM	91.5 keV	115.7 keV	N/A
Cm-244 (5.805 MeV)	5.825 MeV	5.728 MeV	5.732 MeV
FWHM	96.4 keV	115.7 keV	N/A

Table 8: Peak energy results from experiment and simulation.

Chapter 4

Experimental Results

With the single TOF module constructed, measurements were performed to characterize the module, including detection efficiency and initial timing measurements.

4.1 Single Module Efficiency Measurements

An important characteristic of any transmission based TOF system is the efficiency with which it can detect the heavy ion through detection of the electrons ejected from the conversion foil. The number of secondary electrons (SE) produced in the $100 \mu\text{g}/\text{cm}^2$ carbon foil is directly proportional to the energy lost (dE/dx) by the primary ion based on the square of its nuclear charge, Z^2 .

Thus, heavier elements have a higher linear energy transfer value and produce a much higher secondary electron yield. SEs are emitted from both sides of the carbon foil, so the electrodes and electron detector may be placed either upstream or downstream of the foil. SEs emitted in the “backward” direction (upstream, or opposite the heavy ion direction) have a lower kinetic energy as well as a decreased yield [Pferdekamper, 1977]. The lower energy component is favorable, as the secondary electrons emitted from the foil will have a diminished energy spread, which leads to tighter focusing with the electrodes, which reduces the time and position straggling of the SEs arriving at the MCP.

Alpha particles and fission products incident on $2 \mu\text{g}/\text{cm}^2$ carbon foil were

investigated by K.E. Pferdekamper and H.G. Clerc at the Institute of Kernphysik [Pferdekamper, 1977]. Table 9 summarizes the finding of Pferdekamper and serves as the basis for SIMION simulation input for the current work.

	α -particle		Light Fragment		Heavy Fragment
Energy (MeV/amu)	1.5	0.48	0.45	0.93	0.52
Number of SE/ion in forward direction					
KE < 230 eV	2.4	5.7	119	109	126
KE >230 eV	0.4	0.7	68	75	77
Number of SE/ion in backward direction					
KE < 230 eV	1.9	3	46	56	59
KE >230 eV	0.07	0.07	5	7	7
Total # of SE in 4π	4.8	9.5	238	247	269
SE mean KE (eV)	100	60	190	260	200

Table 9: SE production properties for α -particles and fission fragments through 2 $\mu\text{g}/\text{cm}^2$ carbon foil

Due to the low electron yield in the upstream direction from alpha particles, the single module unit was oriented to utilize the electrons ejected downstream. This orientation can easily be switched for fission fragments, with a much higher SE yield upstream and downstream than found from alpha particles.

4.1.1 Single Module Efficiency Calculations

Using the SIMION Ion and Electron Optics Simulator software package, simulations were performed to test and investigate important quantities regarding efficiency before making time consuming adjustments to the

experiment. Utilizing this simulation package, detailed information regarding the SE characteristics on their path from the carbon foil to the MCP can be determined. A “fast-refine” rendering of the geometry and initial voltage potentials used for the examination of SE characteristics is shown in Figure 35.

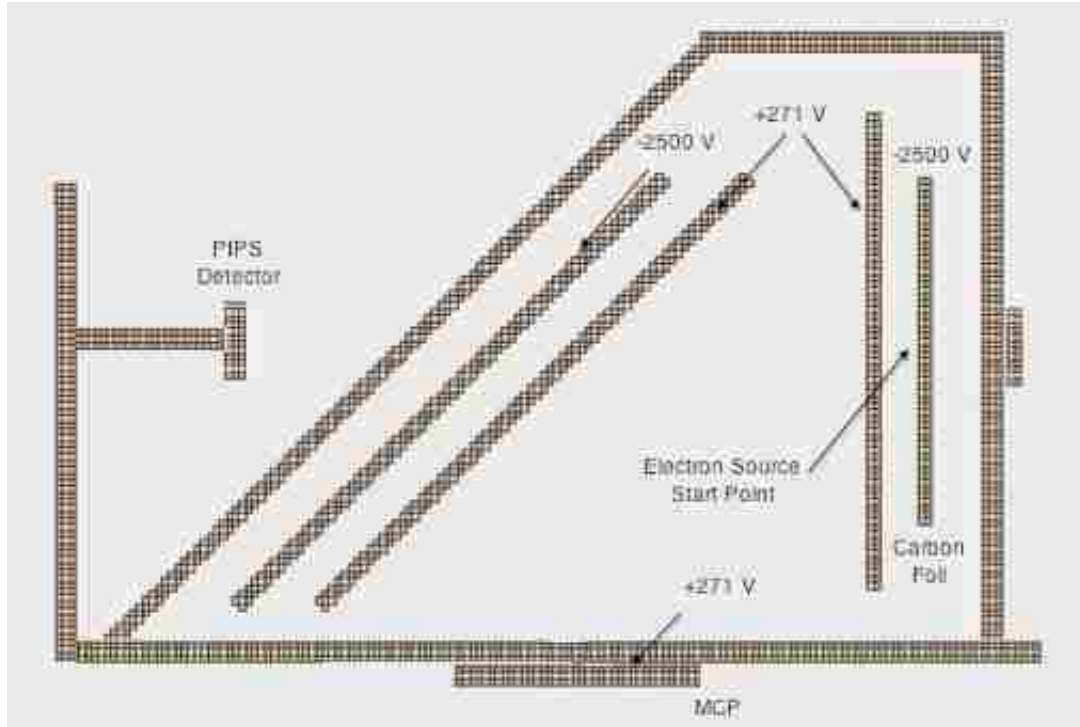


Figure 35: Example of SIMION geometry setup for secondary electron timing and efficiency simulations. The ion enters the module from the right.

Several useful quantities were extracted from the simulation such as electron KE at the MCP input, TOF, incident angle and probability of reaching the MCP input surface. These values, along with the experimental data from Pferdekamper, were used to estimate the expected efficiency using a simple binomial distribution.

$$\sum_{\vartheta=0}^n B_{np}(\vartheta) = \sum_{\vartheta=0}^n \binom{n}{\vartheta} p^{\vartheta} q^{n-\vartheta} = 1 \quad [\text{Eq. 20}]$$

Where $\binom{n}{\vartheta}$ accounts the various outcome schemes and can be written as;

$$\binom{n}{\vartheta} = \frac{n!}{\vartheta!(n-\vartheta)!} \quad [\text{Eq. 21}]$$

p in the binomial distribution is simply the inherent probability of detection for the MCP, q is the probability of non-detection or $(1-p)$. The number electrons emitted per ion is represented by n and the number of possible electron interactions with the MCP is represented by ϑ . Since only a single electron interaction with the MCP is necessary to generate a signal the efficiency of the system can be represented by the following.

$$\left[\sum_{\vartheta=1}^n \binom{n}{\vartheta} p^{\vartheta} q^{n-\vartheta} \right] - \left[\binom{n}{0} p^0 q^{n-0} \right] = \textit{Coincidence Efficiency} \quad [\text{Eq. 22}]$$

This is simply the difference between the probability of one or more electrons emitted from the carbon foil initiating channel multiplication and no electrons initiating a multiplication event. This also assumes that every electron emitted from the foil arrives at the active area of the MCP. For the alpha particle measurement, the acceleration/reflection potentials as well as the positioning of the reflection grid relative to the MCP becomes important to reaching an optimum efficiency. Using the acceleration/reflection potentials given in Figure 35 and planned experimental dimensions given in Figure 36, SIMION was used to investigate SE quantities. Electrons are simulated to eject from the from of the foil equally over 2π and over a range of energies, binned in the table. The acceleration foil accelerates the electrons downstream and, with the 2.4 kV voltage difference between the foil and accelerating grid, adds 2.4 keV of energy. The low initial energy electrons have very little lateral momentum and the total energy and final angular spread when striking the MCP are much lower than

high initial energy electrons. The results of the simulation are presented in table 10.

Initial SE KE (eV)	SE Incident Angle (°)	KE at MCP (eV)	Hit Efficiency (%)
1	89.2367	2400.444	100
10	87.6711	2409.177	100
50	85.2529	2449.528	79.51
75	85.0401	2474.542	48.17
100	85.2344	2499.218	31.26
150	85.361	2549.534	19.98
200	85.4575	2599.429	14.86
500	85.24	2898.789	3.2

Table 10: SIMION SE simulation results.

The simulations in SIMION were performed using 10,000 primary electrons. The initial kinetic energy used in the simulation is centered on a Gaussian distribution. However, experiment has shown the SE energy spectrum to have a higher low-energy component resembling a Maxwellian distribution. In this case, the efficiency results are skewed to lower values than would be seen in the experiment as the probability of the SE being created with higher energy is increased with the Gaussian estimation.

Using Figure 18, one can see the MCP has a maximum efficiency when the incident angle of the electrons entering the MCP channels is near 13° to obtain maximum efficiency. With the MCP channels constructed at 12° to the normal of the plate, the electrons in our simulations enter the MCP at an average of ~5 - 17° with respect to the channels, near the peak of the sensitivity curve.

For kinetic energies of the SEs entering the MCP, comparing with the plot of efficiency as a function of SE energy in figure 17, the inherent detection efficiency is estimated to be ~55%. This efficiency value will be used as the value of p in the binomial distribution calculation.

The probability of an electron reaching the active surface of the MCP, the hit efficiency, becomes the key in the case of alpha particles. Since the SE yield per ion in the downstream is on the order of 3 SEs per incident alpha particle, the possibility of SEs not reaching the surface of the MCP has a significant impact on the overall coincidence efficiency.

Using the results found in the simulation, specific values can be applied to the expected detection and non-detection probability quantities in equation 22.

$$\left[\sum_{\vartheta=1}^3 \binom{3}{\vartheta} 0.55^{\vartheta} 0.45^{3-\vartheta} \right] - \left[\binom{3}{0} 0.55^0 0.45^{3-0} \right] = 81.78 \%$$

The SE/ion, n , is taken to be 3 as the $E/A = 1.37$ value for alpha particle this experiment falls between the alpha particle $E/A = 1.5 - 0.48$ used in the Pferdekamper experiment. With precise positioning and applied potential, the efficiency is expected to be around the value of 60-70% with the assumptions made in the SIMION simulation.

4.1.2 Single Module Efficiency Measurements

Experimental efficiency measurements were performed using a PIPS detector for alpha detection in coincidence with the MCP for secondary electron detection.

The dimensions for the final efficiency measurement are given in Figure 36.

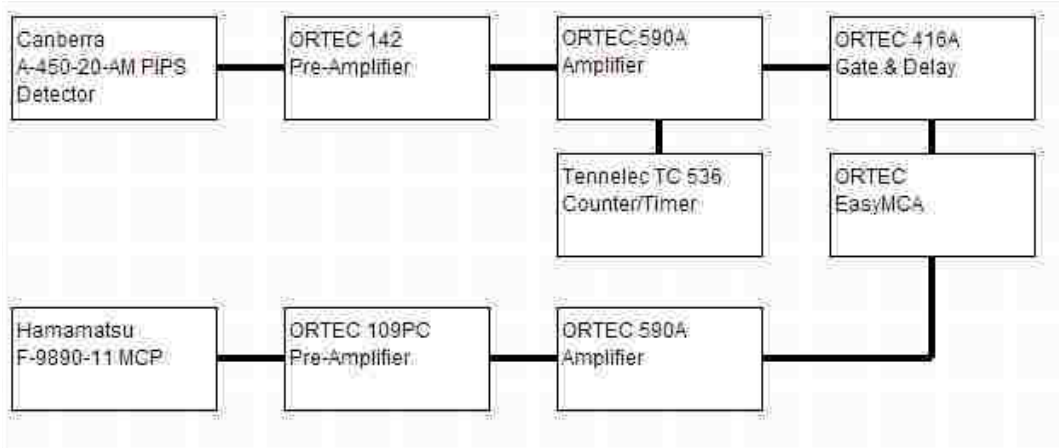


Figure 37: Experimental setup for the coincidence efficiency measurement

A downstream PIPS detector was used to detect alpha particles, producing a logic gate that was a requirement for accepting signals in the EasyMCA from the timing module MCP. The PIPS detector was extremely clean, producing no signals when no alpha source was present, giving confidence to this method. A gate signal width of 50 ns was used since a small gate width decreases accidental coincidences [Leo, 1993]. This is expressed mathematically as:

$$\textit{Accidental Coincidence} = N1 * N2 * \sigma \quad [\text{Eq. 23}]$$

Where $N1$ and $N2$ are the count rates for the MCP and PIPS detector and σ is the gate width. The accidental count rate is low for this work as the count rates above the trigger threshold are less than 10 Hz for the MCP and ~ 0.10 Hz for the gating PIPS detector.

To set the discriminator on the PIPS detector, a pulse height distribution was taken in real time as the discriminator was adjusted. The pulse height discriminator was set to 2 V as this effectively cuts out any infrequent low energy

pulses not attributed to the alpha particles being investigated, which were centered tightly around 4 V. The discriminator on the MCP is carried out by the ADC in the EasyMCA and is set at channel 20 to omit low-level noise in the MCP circuit. A 0.052 μCi ^{241}Am source provided alpha particles. The primary alpha particle energy (84.8% branching) used was 5.485 MeV. The alphas were collimated to 6° half angle with a solid angle slightly smaller than the PIPS detector at the detector distance.

For the initial measurements, the distance from the foil to the reflector, L_1 , and the distance from the reflector to the MCP, L_2 , as shown in figure 36, were configured to 5.8 cm and 6.5 cm, respectively. This returned consistent experimental coincidence efficiency results of $\sim 15 - 20\%$ with a counting time of 10 hours for sufficient statistics. The experimental efficiency was found by taking the ratio of the number of MCP pulses in coincidence with the PIPS based gate to the number of times the PIPS detector fired.

SIMION simulations show that the hit efficiency improves by shifting the single module unit forward relative to the MCP surface by 1.5 cm as shown in Figure 37. These adjustments were made to the single module unit, resulting in the final dimensions that were presented in Figure 36.

SIMION simulations also show the electron angular distribution being coned down towards the reflector and thus the MCP with increasing accelerating voltage. This was borne out experimentally. The results of efficiency as a

function of acceleration potential are presented in Figure 39 with a saturated efficiency ~68 - 70%.

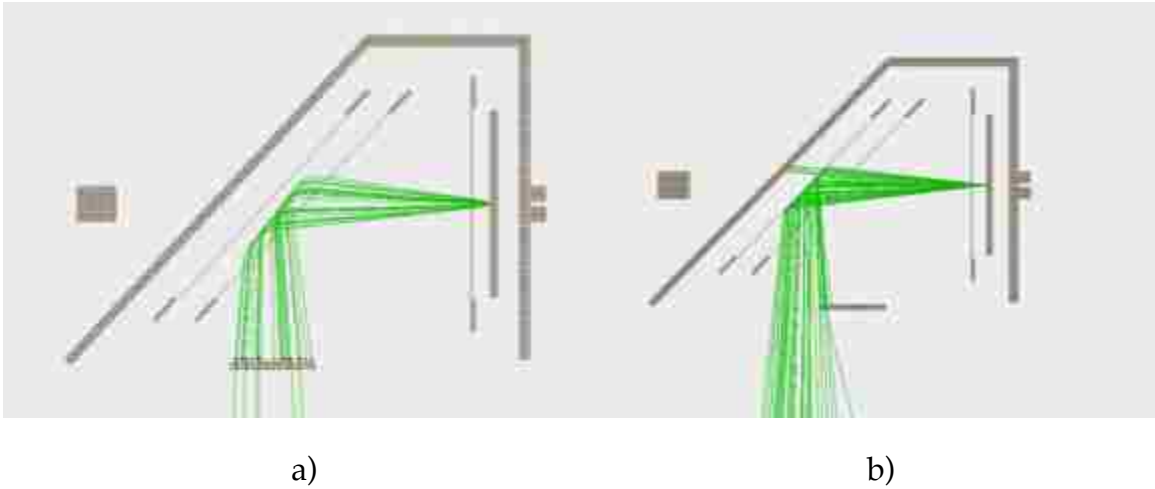


Figure 38: a) Simulated SE flight path with the single module shifted forward by 1.5 cm, hit efficiency = 70-80%. b) Initial MCP position, hit efficiency = 5-10%

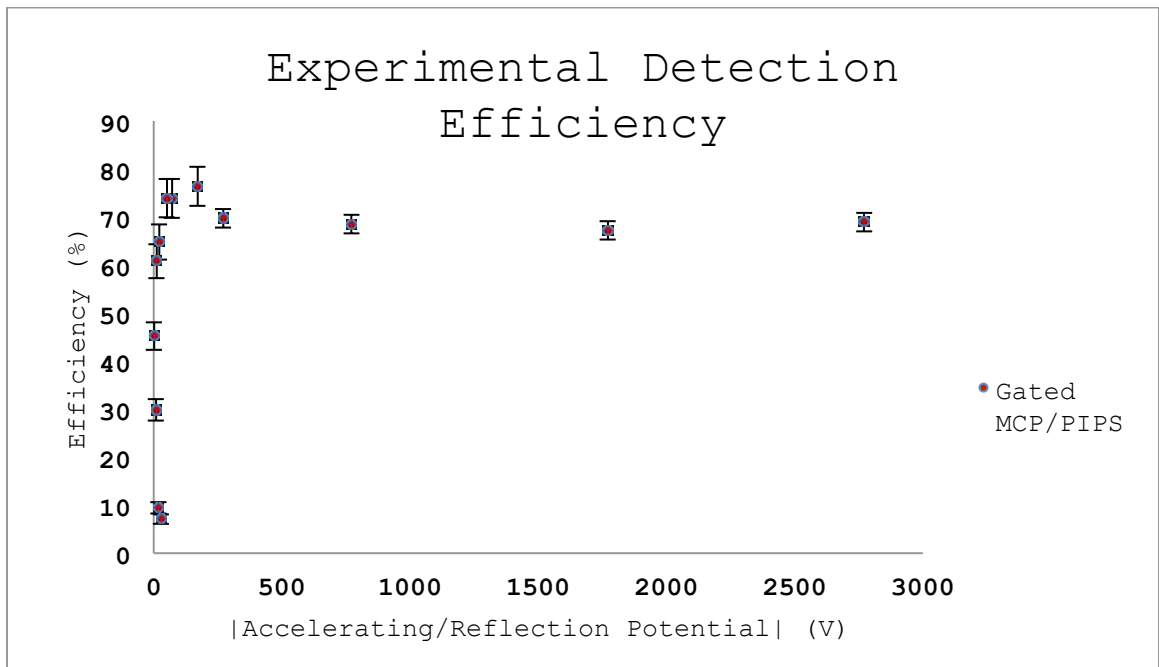


Figure 39: Efficiency of the single module coincidence unit.

These results are in good agreement with previous efficiency measurements performed on similar SE reflection experiments by D'Erasmus et al ($74\% \pm 0.7\%$) [D'Erasmus, 1985]. The main difference in experiments performed by D'Erasmus et al being the reflection potential was kept constant while adjusting the acceleration potential. For this work, the carbon foil and reflection grid voltages are supplied by the same voltage source keeping the ratio of reflection to acceleration potentials equal to or greater than 1. A condition on the potential ratio such that the SEs experience reflection is given by Nankov *et al* [Nankov, 2006],

$$\frac{\Delta V_r}{\Delta V_f} \geq 0.5 \quad [\text{Eq. 24}]$$

The steep drop off in efficiency at low potentials could be due to keeping the ratio in equation 24 equal to or greater than 1. The steep slope in efficiency at low accelerating potentials resembles another SE reflection experiment by Kosev where an efficiency of $\sim 25\%$ was achieved for alpha particles with energy 5.8 MeV, however, the reflection potential used in this work is not reported [Kosev, 2008]. In the D'Erasmus experiment, in which the reflection potential is held constant, the efficiency begins to decrease at an accelerating voltage of 1000 V. SIMION simulations suggest that if that ratio is brought too much above 1, the SEs experience too much reflection and subsequent angular spread, which effectively lowers the hit efficiency as is presented in Figure 40. This ratio becomes important to the optimization of timing measurements discussed in the following section.

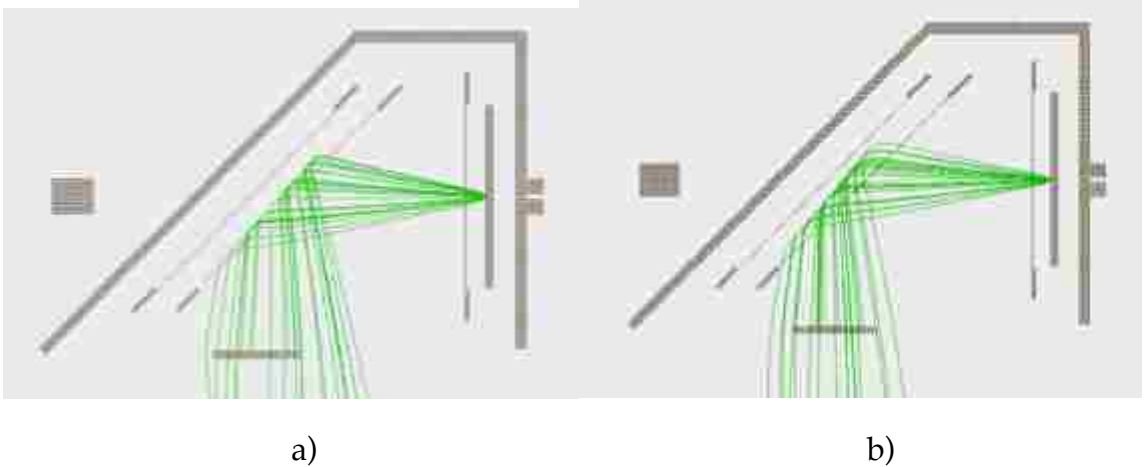


Figure 40: a) Reflection potential at 2500 V, acceleration potential at 1000 V (lower efficiency) and b) Reflection potential at 1000V, acceleration potential at 1000 V (higher efficiency)

4.2 Single Module Timing Measurements

For the single module TOF measurements, dimensions for L_1 and L_2 are kept at the optimum efficiency values 5.8 and 5.0 cm respectively. The ratio of reflection to acceleration potential is kept at a value of 1, with a $\Delta V_{r,f} = 2771$ V.

4.2.1 Timing Optimization

The electric field potentials within the system can be described by three distinct regions: the acceleration region, the field free region, and the reflection region. The SEs emitted from the surface of the foil, enter the acceleration region and immediately experience the acceleration potential between the charged foil and acceleration grid. The angular spread of the SEs, initially slightly forward directed [D'Erasmus, 1985], becomes heavily forward directed as the SEs travel through the acceleration region. After acceleration, the SEs pass through the field

free drift region until crossing the front reflection grid into the reflection region. The SEs are reflected at $\sim 90^\circ$ and leave the reflection field region where they drift in the field free region toward the MCP input surface to be detected. The potential regions are shown in Figure 41.

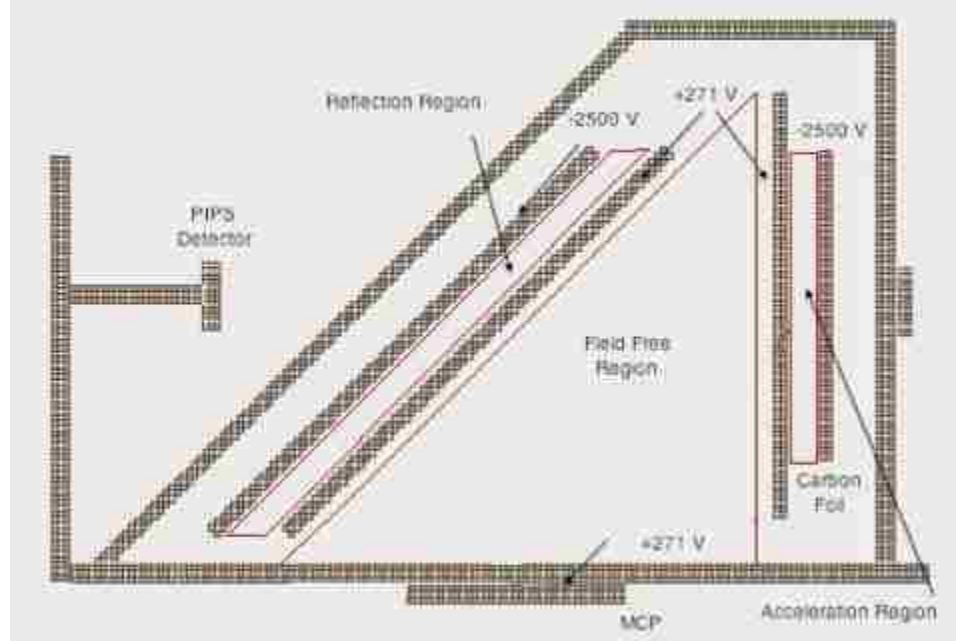


Figure 41: Electric potential regions in the single module unit

Solving the equations of motion for the three regions, a relation can be made between the TOF and characteristics of the acceleration/reflection unit following [Nankov, 2005],

$$T = T_o + \left(\mp \frac{L_1 + L_2 - \frac{d\sqrt{2}\Delta V_f}{\Delta V_r}}{v_o} \pm \left(\frac{2m_e v_o d \sin\theta}{e\Delta V_r} \right) \right) \delta \quad [\text{Eq. 25}]$$

where T_o is the mean TOF, L_1 , L_2 , d , . The distance, d , ΔV_r and ΔV_f are the same quantities discussed in the efficiency measurement, m_e , v_o and δ are the electron mass, initial velocity, and velocity spread. θ is the angle between the reflection

grid and the electron flight direction vector. To make the electron TOF independent of their initial velocity spread, the condition below needs to be satisfied:

$$\frac{d}{(L_1+L_2)} = 0.236 \left(\frac{\Delta V_r}{\Delta V_f} \right) \quad [\text{Eq. 26}] [\text{Nankov, 2005}]$$

This relation becomes problematic for efficiency, as the ratio of reflection potential to acceleration potential in equation 26 would need to be brought well below 0.5 to accommodate current geometries. This relation can never be fully satisfied, however it is a useful guide to improving timing characteristics.

4.2.2 Time Resolution Measurement

The analog data acquisition for the TOF measurements utilizes the same pre-amplifiers used in the efficiency measurements. For timing measurements the ORTEC 590A amplifiers are replaced with ORTEC 460 Delay Line amplifiers, which give a significantly sharper rise time more ideal for setting an optimum trigger level or threshold decreasing the variance (jitter) in the time measurement. Figure 42 shows the experimental setup for the timing measurements.

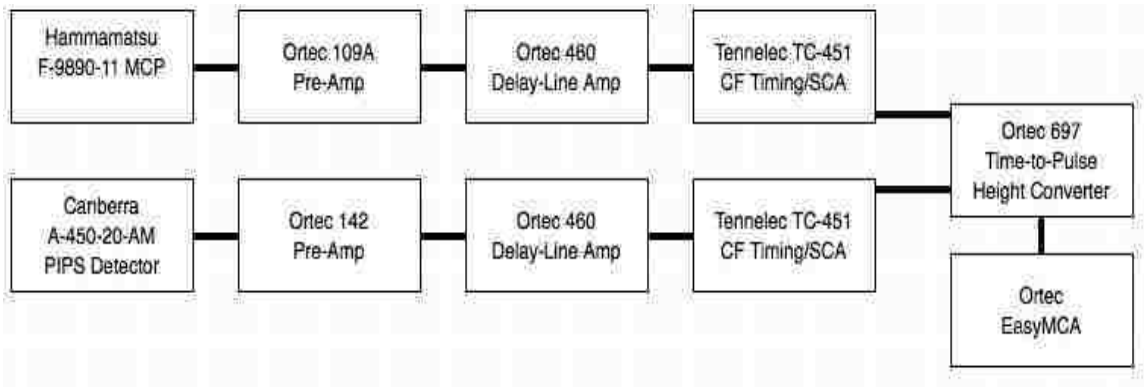


Figure 42: Experimental setup for the timing/ coincidence measurements

The constant fraction (CF) timing generator uses an active filter to generate a pulse delay from the input pulse. The signal pulse is split with one half delayed and inverted. They are recombined to generate a bipolar pulse with a very stable zero crossing. The logic pulse is generated from the zero crossing, making the timing measurement independent of pulse amplitude. This should eliminate inaccuracies in the timing pick off attributed to discriminator walk arising from the varying pulse heights experienced with the MCP discussed previously. The appropriate delay is applied so the PIPS CFT/SCA logic pulse arrives before the MCP CFT/SCA logic pulse; this operation was performed on the Tektronics 4-channel oscilloscope, the delay was adjusted on the PIPS CFT/SCA logic pulse to arrive ~ 80 ns before a MCP CFT/SCA signal was typically seen. The PIPS CFT/SCA logic pulse serves as the *time 1* and gate initiation, with the MCP CFT/SCA signal initiating *time 2*. The TOF is then, $TOF = time\ 2 - time\ 1$. The time 1 and time 2 signals are input to the start and stop times for a time to analog convertor (TAC), which outputs a pulse height proportional to the time difference. The pulse height from the TAC, representing the TOF, is fed to the EasyMCA for timing spectroscopy. The TAC was calibrated using a Canberra 807 Pulser. The input start signal was split and run through a cable to serve as a known delayed stop signal, thus providing a timing calibration. A full spectrum width of 100 ns was chosen for this work. The results of the PIPS-MCP timing resolution are given in Figure 43.

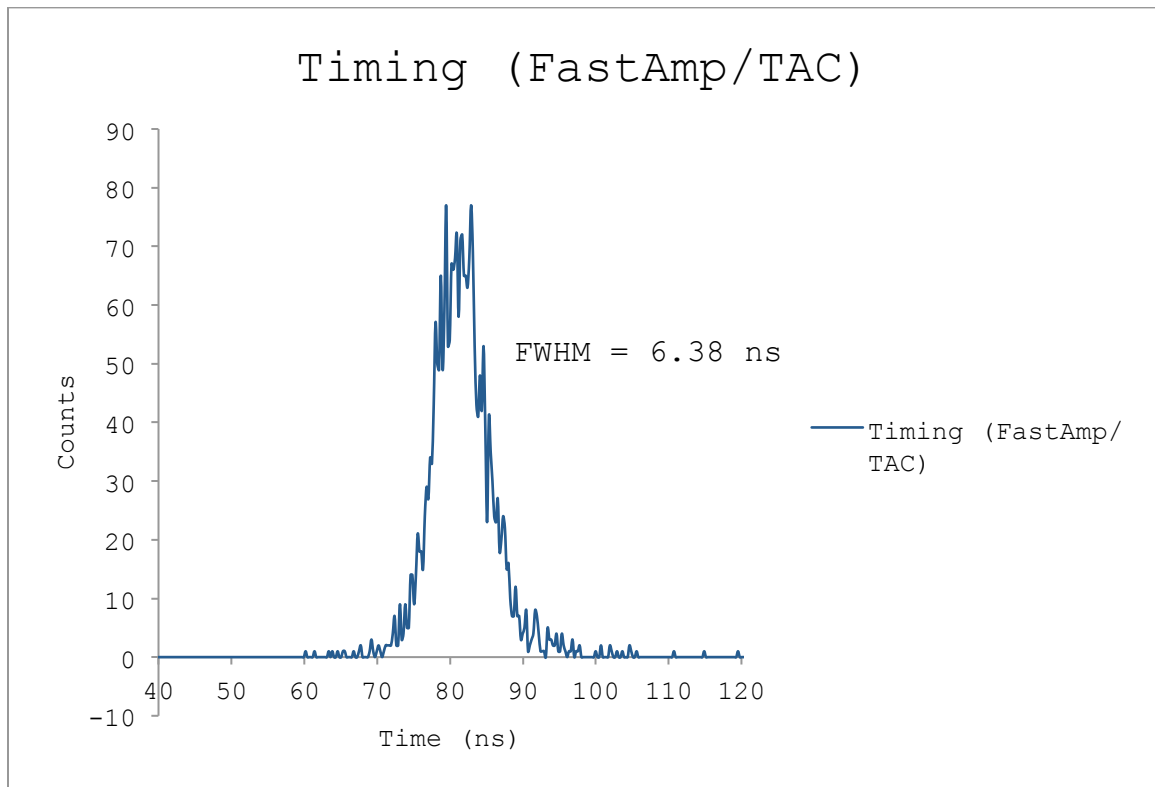


Figure 43: Timing results for the PIPS-MCP coincidence measurements

The single module unit returns a time resolution of 6.38 ns. The timing characteristics of the single module unit are assumed to be dominated by the PIPS detector and analog data acquisition electronics used. The timing resolution of this work compares favorably to a similar timing detector developed by Kosev [Kosev, 2007], where a timing resolution of 15 ns was achieved for a surface barrier (SB) – MCP coincidence measurement using a similar ^{241}Am source.

Chapter 5

Conclusions

The single module coincidence unit performed better than had been anticipated. The efficiency of the system was optimized to reach a saturated coincidence efficiency of $\sim 70\%$ for alpha particles, matching simulations but an improvement in experimental efficiency values reported by Kosev (20-25%) and Starzecki (54%) and in agreement with the work by D'Erasmus (74%) [Kosev, 2007; Starzecki, 1982; D'Erasmus, 1985]. This improvement was realized through diligent troubleshooting and simulation studies to adjust experimental parameters.

Timing resolution measurements on the single module compare favorably with previous MCP-SB type detector timing measurements by Kosev (15 ns), with improved resolution in the current work (6.38 ns). The PIPS detector becomes the limiting factor for measuring timing resolution and thus determining whether the time resolution of the MCPs is adequate to achieve 1 amu mass resolution in the full spectrometer. To further investigate the timing limitations of the MCP, timing measurements will need to be made between two MCPs when the second timing module unit is constructed and installed as is discussed in chapter 6.

Chapter 6

Future Work

The single-arm prototype detector to be fielded at the LANSCE facility for fission fragment identification still has a decent amount of characterization to be done before completion. The MCP-MCP characterization and addition of the ion chamber (IC) for the KE and Z measurements are the major components of the work left to be done before fielding the single-arm prototype detector.

6.1 MCP-MCP Characterization

The *time 2* detector setup still needs to be constructed and tested in conjunction with the *time 1* single module unit tested in this work. The work performed in this thesis should expedite the construction process of the *time 2* detector. From previous experiments performed by Kosev [Kosev, 2007] and our LANL collaborators, we expect to achieve a time resolution ~150-190 picoseconds or better between the two MCPs which is adequate for the required spectrometer mass resolution.

6.2 Ion Chamber

The addition of the ion chamber (IC) to collect energy and charge information will be a more challenging and time consuming process considering the pressure differential between the time-of-flight and IC sections.

The IC has been designed and constructed by UNM graduate student, Drew Mader in conjunction with the construction of the time detectors. The axial IC consists of copper cathode and anode with a voltage potential of 1100 V with guard rings to limit field distortion. The IC will replace the surface barrier detector as the energy detector, through Bragg spectroscopy the charge information can be obtained as well. Figure 44 shows the current IC construction attached to a ConFlat flange by four, 8-32 stainless steel threaded rods.



Figure 44: Axial IC installed onto ConFlat flange

The ionization chamber is filled with ionization gas, while the TOF portion of the spectrometer is held at high vacuum. When connected there will be a thin entrance window to the IC planned for separating the regions. The next challenge will be testing entrance. Mylar is typically used but SiN will be investigated as a possible alternative to mylar. SiN can withstand the pressure differential between the regions for a thinner window than mylar, resulting in less energy loss and straggling of the incident ions.

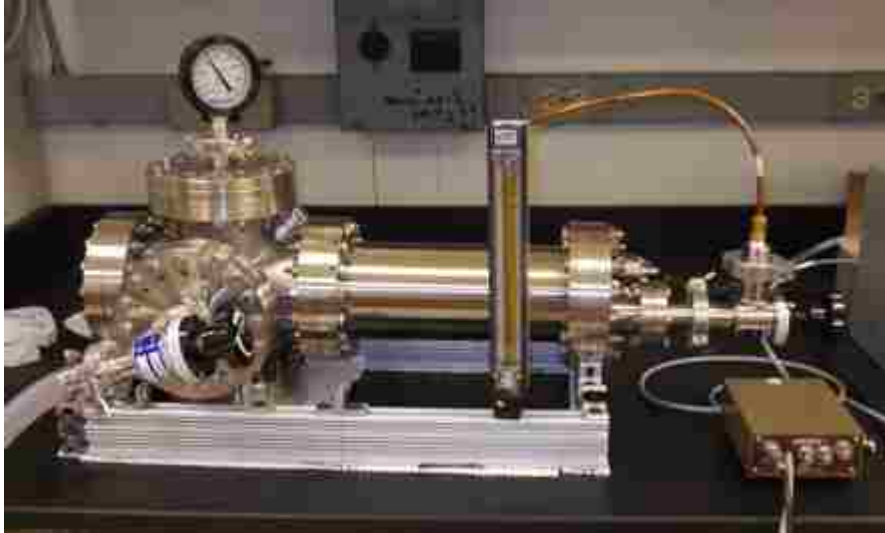


Figure 45: IC experimental setup

The ion chamber is near completion, operating in P-10 gas, the ion chamber is currently returning energy resolution $\sim 1.2 - 1.5\%$. Figure 45 shows an external view of the IC experiment during P-10 gas flow testing. Figure 46 shows a 19.4 hour count, without gas flow. The recent addition of gas flow has led to improvements in the energy resolution to 1.2 %.

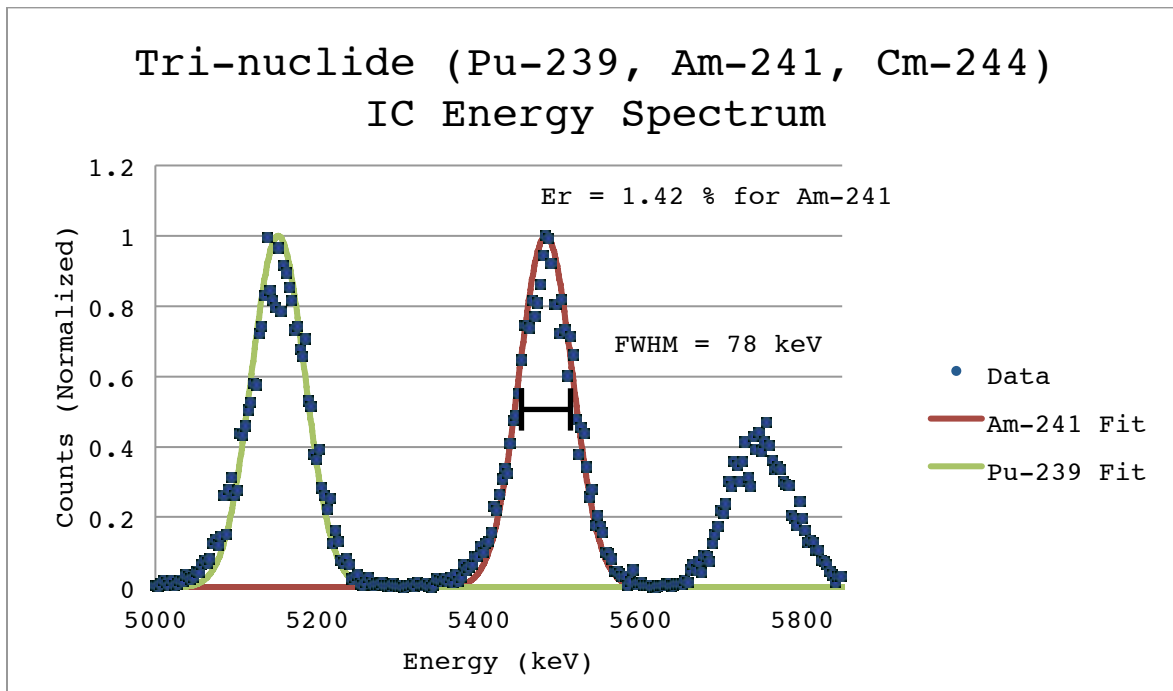


Figure 46: Early results for IC energy spectrum using a 0.025 μ Ci Tri-nuclide source

Bibliography

- [Adams, 1966] J. Adams and B.W. Manley, *The Mechanism of Channel Electron Multiplication*, IEEE Transactions on Nuclear Science, NS-13-88 1966
- [Agostinelli, 2003] S. Agostinelli *et al.*, *Geant4 a simulation toolkit*, Nucl. Instrum. Meth. A506, 250 (2003).
- [Blakeley, 2011] R. Blakeley *et al.*, *Comparison of GEANT4 and MCNPX/CINDER for use in Active Interrogation Simulation*, INMM 51st Ann. Conf. Proc. 2011
- [Boucheneb, 1989] N. Boucheneb *et al.*, *High-Resolution Measurements of Mass, Energy and Nuclear Charge Correlations for Th-229(n,f) with the COSI FAN TUTTE Spectrometer*, Nuclear Physics, A 502 261-270, 1989
- [Canberra, 2012] Canberra <http://www.canberra.com>, *Passivated Implanted Planer Silicon (PIPS) Detector*, 2012
- [Chadwick, 2011] M.B. Chadwick, *Future Challenges for Nuclear Data Research in Fission*, Journal of the Korean Physical Society, Vol.59 No.2, 752-754, 2011
- [D'Erasmus, 1985] G. D'Erasmus and V. Paticchio, *A Transmission Time Detector for Low Energy Light Ions*, Nucl. Instr. And Meth., A234 91-96, 1985
- [Durkee, 2009a] J.W. Durkee, Jr., M.R. James, G.W. McKinney, H.R. Trellue, L.S. Waters, W.B. Wilson, *Delayed-gamma signature calculation for neutron-induced fission and activation using MCNPX. Part I: Theory*, Progress in Nuclear Energy 51, 813 (2009).
- [Durkee, 2009b] J.W. Durkee, Jr., M.R. James, G.W. McKinney, H.R. Trellue, L.S. Waters, W.B. Wilson, *Delayed-gamma signature calculation for neutron-*

- induce fission and activation using MCNPX. Part II: Simulations, Progress in Nuclear Energy* 51, 828 (2009).
- [England, 1993] T.R. England and B.F. Rider, "Evaluation and Compilation of Fission Product Yields", Los Alamos National Laboratory, LA-UR-94-3106; ENDF-349 (1993).
- [Fischer, 1964] P.C. Fisher and L.B. Engle, *Delayed Gammas from Fast-Neutron Fission of Th^{232} , U^{233} , U^{235} , U^{238} , and Pu^{239}* , Physical Review 134, B796 (1964).
- [Ganesan, 1990] S. Ganesan, *Nuclear Data for Neutron Emission in the Fission Process*, Proceedings of a Consultants Meeting, 1990
- [Hall, 2007] J.M. Hall, S. Asztalos, P. Bilotto, J. Church, M.-A. Descalle, T. Luu, D. Manatt, G. Mauger, E. Norman, D. Petersen, J. Pruet, S. Prussin, D. Slaughter, *The Nuclear Car Wash: Neutron interrogation of cargo containers to detect hidden SNM*, Nuc. Instrum. Meth. B 261, 337 (2007).
- [Hamamatsu, 2001] Hamamatsu Technical Document, *MCP Assembly*, Hamamatsu Corporation, 2001
- [Holloway, 2011] S.T. Holloway, W.B. Wilson, I.C.T. Kelsey, H. Little, V. Mozin, *A manual for CINDER2008 codes and data*, Manual LA-UR 11-00006, Los Alamos National Laboratory, Los Alamos, NM (2011).
- [IAEA, 2000] IAEA Co-ordinated Research Project, *Compilation and Evaluation of Fission Yield Nuclear Data*, IAEA-TECDOC-1168, 2000
- [ILL, 2012] Institut Laue-Langevin, <http://www.ill.eu/instruments-support/instruments-groups/instruments/pn1/>, *Fission product spectrometer PN1*, 2012

- [Katakura, 2003] J. Katakura, *Present Status of Fission Yield Data*, JAERI Research, 2003
- [Kosev, 2007] K. Kosev, *A High-Resolution Time-of-Flight Spectrometer for Fission Fragments and Ion Beams*, Dissertation, Institute for Kern Physics, 2007
- [Kosev, 2008] K. Kosev et al, *A high-resolution time-of-flight spectrometer with tracking capabilities for fission fragments and beams of exotic nuclei*, Nuclear Instruments and Methods, A 594 2008 178-183
- [Leo, 1993] W.R. Leo, *Techniques for Nuclear and Particle Physics Experiments*, Springer Verlag, 1993
- [MCNPX, 2008] *MCNPX Version 2.6.0 User's Manual*, LA-CP-07-1473, Los Alamos National Laboratory, Los Alamos, NM (2008).
- [Moller, 1995] P. Moller, J. Nix, W. Myers, and W. Swiatecki, *At. Data, Nuclear Data Tables* 59 (1995) 185
- [Moller, 2001] P. Moller, D. G. Madland, A. J. Sierk, and A. Iwamoto, *Nuclear fission modes and fragment mass asymmetries in a five-dimensional deformation space*, *Nature* 409, (2001) 785.
- [Nankov, 2006] N. Nankov et al, *Energy Distribution of Secondary Electrons by Swift Heavy Ions in Thin Foils*, *Wissenschaftlich-Technische Berichte, FZR-442*, 15, 2006
- [Nankov, 2005] N. Nankov et al, *Calculations for the Optimization of the Time and Space Resolution of an Electrostatic Mirror*, *Wissenschaftlich-Technische Berichte, FZR-423*, 26, 2005
- [NASA, 2013] NASA <http://outgassing.nasa.gov>, *Outgassing Data for Selecting Spacecraft Materials*, 2013

- [Nix, 1972] J. Nix, *Nuclear Mass Formula with Yukawa-plus-exponential Macroscopic Model and a Folded-Yukawa Single-Particle Potential*, *Annu. Rev. Nucl. Sci.* 22 (1972) 65.
- [Oed, 1984] A. Oed et al., *High Resolution Axial Ionization Chamber for Fission Products*, *Nuclear Instruments and Methods* 225 (1984) 508
- [ORTEC, 2010a] ORTEC <http://www.ortec-online.com>, *Introduction to Amplifiers*, 2010
- [ORTEC, 2010b] ORTEC <http://www.ortec-online.com>, *Experiment 5 Energy Loss with Heavy Charged Particles (Alphas)*, 2010
- [Pferdekamper, 1977] K.E. Pferdekamper and H.G. Clerc, *Energy Spectra of Secondary Electrons Ejected by Ions from Foils*, *Z. Physik, A* 280 155-164, 1977
- [Poenaru, 1997] D.N. Poenaru, W. Greiner, *Experimental Techniques in Nuclear Physics*, de Gruyter, 1997
- [Roentdek, 2013] RoentDek GmbH; <http://www.roentdek.com>
- [Schmidt, 1966] K.C. Schmidt and C.F. Hendee, *Continuous Channel Electron Multiplier Operated in the Pulse Saturated Mode*, *IEEE Trans. Nucl. Sci.*, NS-13-100, 1966
- [Selby, 2010] H.D. Selby et al, *Fission Product Data Measured at Los Alamos for Fission Spectrum and Thermal Neutrons on Pu-239, U-235, and U-238*, *Nuclear Data Sheets*, 111, 2010
- [Starzecki, 1982] W. Starzecki et al, *A Compact Time-Zero Detector for Mass Identification of Heavy Ions*, *Nucl. Instr. And Meth.*, 193, 499-505, 1982
- [Vertes, 2010] A. Vertes et al, *Handbook of Nuclear Chemistry Second Edition*, Springer, 2010

[White, 2012] M.C. White, *Advancing the Fundamental Understanding of Fission*,
LANL Internal Document 2012077DR

[Wiza, 1979] J.W. Wiza, *Microchannel Plate Detector*, *Nuclear Instruments and
Methods*, 162-587, 1979

[Wimett, 1959] T.F. Wimett and J.D. Orndoff, *Applications of Godiva II Neutron
Pulses*, *Proc. 2nd Intern. Conf. Peaceful Uses At. Energy Geneva, 1958*,
vol. 10, 449 (1959).



Appendix A

A.1 MCP Further Information

A.1.1 MCP Composition

Z	Element	Weight (%)
82	Pb	47.8
8	O	25.8
14	Si	18.2
19	K	4.2
37	Rb	1.8
56	Ba	1.3
33	As	0.4
55	Cs	0.2
11	Na	0.1

Table A1: MCP glass composition by element [Wiza, 1979]

A.1.2 Dark Current

The dark current or internal background current produced by a MCP is remarkably low. The dark current is primarily thought to come from four sources: thermionic and electric field emission from the channel walls, the ionization of residual gases, the local discharge by the high electric field and last, the photo-electron emission by photons created by electric field scintillation of the MCP support structure [Hamamatsu, 2001]. The background current of MCPs is typically less than 0.5 pA/cm^2 with an applied voltage of 1 kV. The dark count rate for a Chevron or Z-stack MCP is relatively low, typically less than 1-3 count/s- cm^2 at an applied voltage of 1 kV per stage [Kosev, 2007]. Dark current can be reduced through manufacturing techniques, operating at specified

vacuum conditions or cooling methods. Contaminations within the glass, such as sodium and rubidium that arises through the manufacturing process, add to the background current. An increase in background current can be seen when vacuum conditions rise above 10^{-3} mtorr due to ion feedback. Though not always practical, MCP cooling has been shown to decrease the dark current.

A.1.3 MCP Lifetime Characteristics

The lifetime characteristics of MCPs are primarily a function of the accumulated charge drawn from the MCP. This reduces the conversion efficiency, which results in a diminished gain of the system over time. A plot of the relative gain of an MCP as a function of accumulated operation time is given in Figure A1.

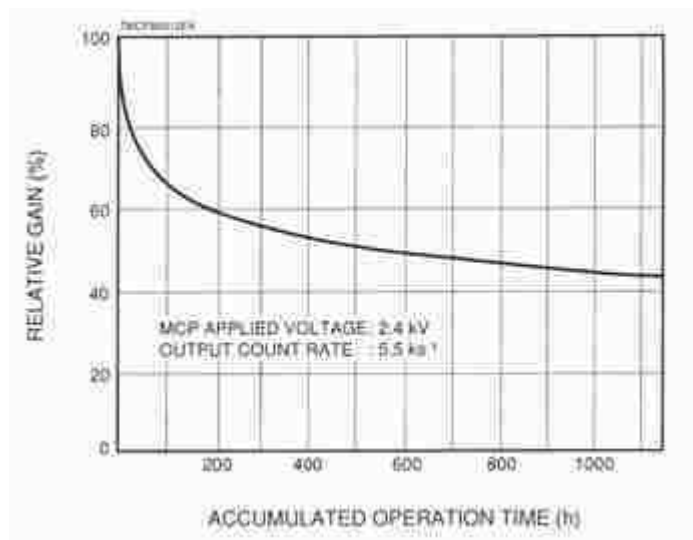


Figure A1: Gain reduction as a function of operation time [Hamamatsu, 2001]

The degree of vacuum during operation and storage is a key component to increasing the lifetime of the MCP. The MCP should be operated at no higher than 10^{-3} mtorr to ensure damage due to ion feedback is kept to a minimum and

electrical breakdown does not occur. MCPs are also subject to hydrocarbon contamination, which can lead to an increase in the work function on the input surface and channel walls, thereby decreasing both efficiency and gain of the MCP. If vacuum conditions are not available for MCP storage, than a dry storage desiccator filled with nitrogen or argon gas will suffice to extend the MCP lifetime while non-operational [Hamamatsu, 2001].

A.2 Simulations of Active Interrogation & Use of Fission Fragment Data

Fission fragment distribution data gathered by the spectrometer being developed will be added to simulations to better model fission fragmentation. To understand the current state of simulation capabilities, fission fragment populations were produced using Geant4 and using MCNP/CINDER and were compared with experiment.

Interest in using a single, all-encompassing simulation method has been sought for the purposes of active interrogation study. In this analysis, the delayed photons from fission product de-excitation are the primary interest. Fisher & Engle's [Fischer, 1964] performed experiments to determine the time and energy dependence of delayed gamma production from 2 MeV neutron induced fission in a sample of ^{235}U . This provided a benchmark for the simulation packages utilized in the simulation study to be accomplished, using both MCNPX/CINDER & GEANT4. The MCNPX/CINDER calculations were performed by Dr. Cassiano De Oliveira's group at UNM, while the GEANT4 simulations were modeled and analyzed by the author. The following section will discuss in detail the problem of interest, background on experimental

benchmark, simulation methods, results and further work to be done to improve the simulation quality.

A.2.1 Active Interrogation Simulation Study

As mentioned previously, one method for the detection of Special Nuclear Material (SNM) under both experimental and simulation study is active interrogation. Passive interrogation intends to detect the signal from passive decay of SNM, such as low energy photons and alpha particles. It is much harder to shield the higher energy radiation from induced fission and subsequent fission product decay. In addition, for pulsed interrogation beams, there is a clear time signature to the SNM radiation intensity.

A pulsed interrogation beam may cause scatter and radiation flash that obscures detection of any SNM signal, and thus the delayed signal is of particular importance for interrogation, but there is still much to be understood. Experimental efforts towards active interrogation have been performed, such as with the nuclear car wash at LLNL [Hall, 2007]. Simulations have been performed to understand the active interrogation signal, many of them using MCNPX. The goal is to understand all steps of the process, from incident beam and induced fission, production of fission product inventories, fission product decay and radiation transport to the detectors.

MCNPX [MCNPX, 2008] is generally considered the standard Monte Carlo particle transport code in the Nuclear Engineering community. However, in the specific application of active interrogation simulation where fission and the

delayed signal are important, MCNPX must be coupled with a burn-up code such as CINDER [Holloway, 2011] to give the fission fragment decay product radiation. This radiation is given in bulk, rather than decay by decay, making coincidences impossible to track. The codes are coupled through neutron flux results in the fissionable material, grouped in rough neutron energy bins. Recent efforts have focused on incorporating CINDER into MCNPX to allow for investigating fission decay products [Durkee, 2009a]. If this incorporated CINDER requires the same input parameters as it currently does, though internalized to the Monte Carlo code, this will still limit parameters that can be tracked and likely still make use of the rough energy binning.

It is worthwhile to investigate active interrogation with other simulation tools. GEANT4 [Agostinelli, 2003], originally assembled for high energy physics use and not typically used in the nonproliferation and safeguards community, may be such a useful simulation tool for fission. GEANT Monte Carlo simulations are event-by-event physics simulations, tracking particle by particle. GEANT allows for enormous flexibility depending on the programmer: physics processes may be added or removed to understand particle behavior, geometries may be inserted from a variety of design programs, and specific particles or processes can be tracked allowing, as just one example, a separate examination of fissions produced by primary or secondary neutrons. The toolkit is open source and an enormous number of models and functionalities exist. Finally, in relation to MCNPX, it does not require interfacing between different codes such as MCNPX and CINDER, to track the entire fission process from incident neutron to

outgoing decay radiation thus allowing far more flexibility in parameters tracked.

A.2.2 Means for Simulation

GEANT was originally developed at CERN (European Organization for Nuclear Research), KEK (High Energy Accelerator Research Organization) with the help of international collaborations for use in simulations of high-energy subatomic physics experiments. In an effort to modernize and optimize functionality of the toolkit, object-oriented technology was formally introduced in 1994, moving from GEANT3 based on fortran to GEANT4 based on C++, with the GEANT4 collaboration established in 1999 [Agostinelli, 2003]. Due to its object-oriented framework and open source code, the GEANT4 toolkit has seen an expanded usage throughout various other nuclear-related disciplines at lower energies, including fission-based applications used in this study.

GEANT4 offers a unique C++ based development platform that allows for a sizeable amount of customization by the user. In contrast, MCNPX requires a coupling with the burn up code, CINDER, to produce fission fragment distributions and the subsequent delayed gamma inventory created from the radioactive decay of the fission daughter products. If the problem of interest involves any sort of attenuation due to a shielded source, the fragment and gamma inventory generated by CINDER needs to be re-coupled with MCNPX to accommodate the attenuation and transport. On the other hand, GEANT4 allows for the full transport of all particles, creation of a fission product inventory,

fission product decay as well as the consequent transport of the gamma radiation from the decay event within a single platform.

A.2.3 Experimental Benchmark Description

For this investigation, a benchmark set of data is needed to validate the results of the models. Since it is necessary for these models to amply describe the delayed photon information, the experiment by Fisher and Engle [Fischer, 1964] is useful for comparison. That experiment was proposed to determine the energy and time dependence of the delayed gamma emission from neutron induced fission of ^{232}Th , ^{233}U , ^{235}U , ^{238}U , and ^{239}Pu . The fission targets consisted of metal discs 0.105 inches in diameter, of varied thicknesses, irradiated by neutrons from the GODIVA II ^{235}U critical sphere [Wimett, 1959]. The subsequent delayed gamma radiation from the fission sample was detected in a 4" x 4" NaI total absorption spectrometer.

For the purposes of preliminary investigation, we compared simulations with the results obtained from the experiments on a 99.9% ^{235}U , 0.1% ^{238}U fission target. Experimental results were reported as photons/fission/second, energy/fission/second, and energy/photon, three easily replicated quantities to compare simulations. Modifications to the simulations from the experimental setup and analysis are discussed below.

A.2.4 Simulations

We performed the simulations carried out within this section with an application we have written for GEANT4 version 9.4, and with identical geometric models

using MCNPX version 2.6 coupled with CINDER 2008 beta 5. For the GEANT4 runs, we used advanced example simulation, A01, from the GEANT4 code download from CERN as a starting template to set the application framework, and then modified it significantly to meet the specific needs to best replicate the experiment. The key physics classes coupled and implemented into the GEANT4 application to enable all-inclusive handling of the problem of interest, inducing fission through assessing the fragment decay radiation, are the ParaFissionModel.cc and Radioactivedecay.cc modules. The ParaFissionModel determines the fission break up and fission product generation after a fission event has been processed. After fission products are selected from the fission event, the radioactive decay module handles the subsequent fission product decay towards stability, including photon emission.

Additionally, we used MCNPX and CINDER to provide a validated set of models to the comparison. MCNPX 2.6 was run using ENDF-B/VII cross-section data and 3 million neutron histories. We employed an F4 tally to get the volume averaged 63-group neutron flux for the entire region in question. That is, 63 distinct energy bins for the neutron flux. This 63-group neutron flux was then supplied to CINDER2008b5 along with the CINDER'90 63-group data library in order to perform the activation and depletion analysis. The neutron flux in CINDER was active for 0.043 sec, mirroring the experimental beam pulse. The nuclide inventory and emission data were requested at times ranges 0.2-0.5, 1.0-2.0, 4.0-5.5, 10.0-13.0, and 35.0-45.0 seconds, with 6 sub-bins in each range to capture the trends more accurately in each time bin.

To best model the Fisher and Engle experiment using fission neutrons on the ^{235}U target, as described above, we performed simulations using a simplified geometry consisting of a sphere of 99.9% ^{235}U and 0.1% ^{238}U . In the experiment, the fission target was of variable thickness, and the large self-attenuation for soft gamma rays was corrected for in the reported values. For simulations, to reduce self-shielding of the delayed gamma signal in ^{235}U , the fission target was modeled as a small sphere with a radius of 0.01975 cm, following Ref. [Durkee, 2009b]. A rendering of the GEANT4 simulation is shown in Figure A2.

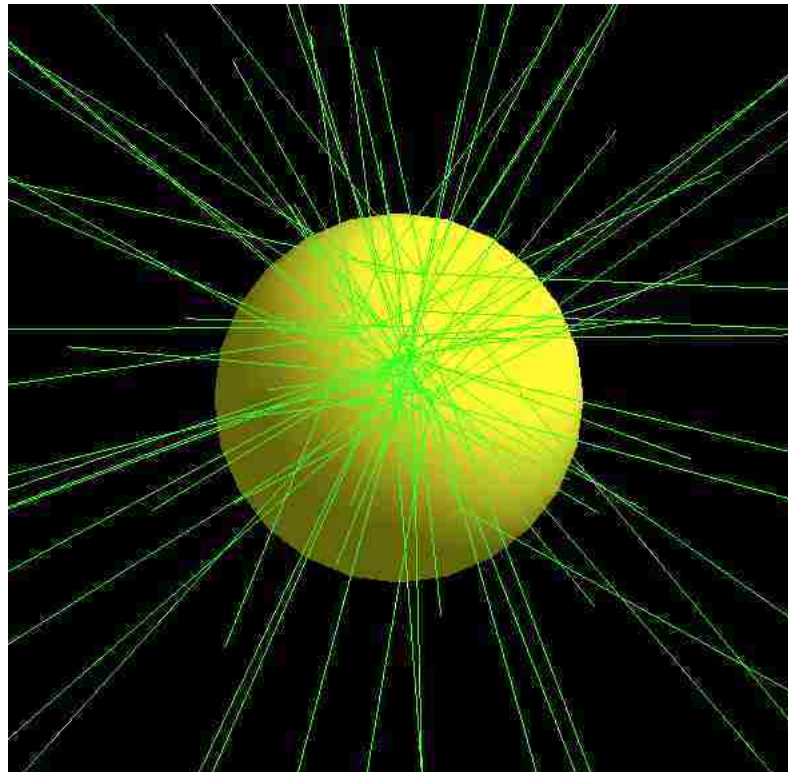


Figure A2: GEANT4 representation of the Uranium sphere

The experiment was run with a fission neutron source. For simplicity and ease of comparison between simulations, we first ran simulations with 2 MeV neutrons, near the average experimental fission neutron energy. For the MCNPX

simulations, we implemented forced collisions to improve fission statistics within the small sphere. GEANT4, on the other hand, did not use forced collisions and the results of 2 MeV neutrons impinging on the small sphere had very low statistics for usable run times.

Thermal neutrons would have a much higher fission cross-section and give much greater statistics for similar simulation time. We undertook investigations into the fission fragment distribution to determine if using thermal neutrons was a valid substitution for 2 MeV neutrons as far as simulation output. Comparisons were made using the GEANT4 simulation to produce fission fragment distributions neutrons on ^{235}U , with 20 million primary neutrons at 2 MeV, and then with 2 million primary thermal energy neutrons. We present a comparison with MCNPX/CINDER and data from the England & Rider [England, 1993] fission product yield distribution library in Figure 3 in linear scale to examine differences. There is minimal difference between the simulated yield values given incident neutron energies of 2 MeV or thermal using GEANT4. Thus we ran the GEANT4 simulations using 2 million primary neutrons at thermal energies to improve reaction and decay statistics. We are studying the differences between our GEANT4, MCNP/CINDER results and the experimental data collected by England & Rider [England, 1993].

A.2.5 Results

From the Fisher and Engle experiments, several easily reproducible quantities of interest regarding delayed gamma emission were obtained: MeV/fission/second,

photons/fission/second, and MeV/fission. Fisher and Engle reported a nominal error of 12% for photons/fission/second and MeV/fission/second, and 15% for photons/fission. The experimental results include photons from 0.1 to 6.5 MeV.

As can be seen from Figure A3, in comparing photons/fission/second the time intervals of 0.2-0.5 and 1.0-2.0 seconds, GEANT4 and MCNPX/CINDER simulations both agree quite well with experimental values. Over the entire range, GEANT4 and MCNPX/CINDER produce lower values than experiment, GEANT4 being typically lower than MCNPX/CINDER.

In the plot of MeV/fission/sec, Figure A4, this same trend continues in nearly the same fashion. However, even in the 0.2-0.5 and 1-2 second time intervals, the spread between the GEANT4 and MCNPX/CINDER results is greater than the 12% nominal error in the experimental photons/fission/sec data.

In comparisons of MeV/photon for these time bins, Figure A5, calculations for the GEANT4 simulations continue to follow the same trend as previous comparisons. The early time interval falls within experimental uncertainty, but deviations from that standard are clearly seen in the later time periods. Since this quantity is not dependent on the number of decays per second as a function of time, but rather on the specific de-excitation energies as a function of time, the trend is much flatter.

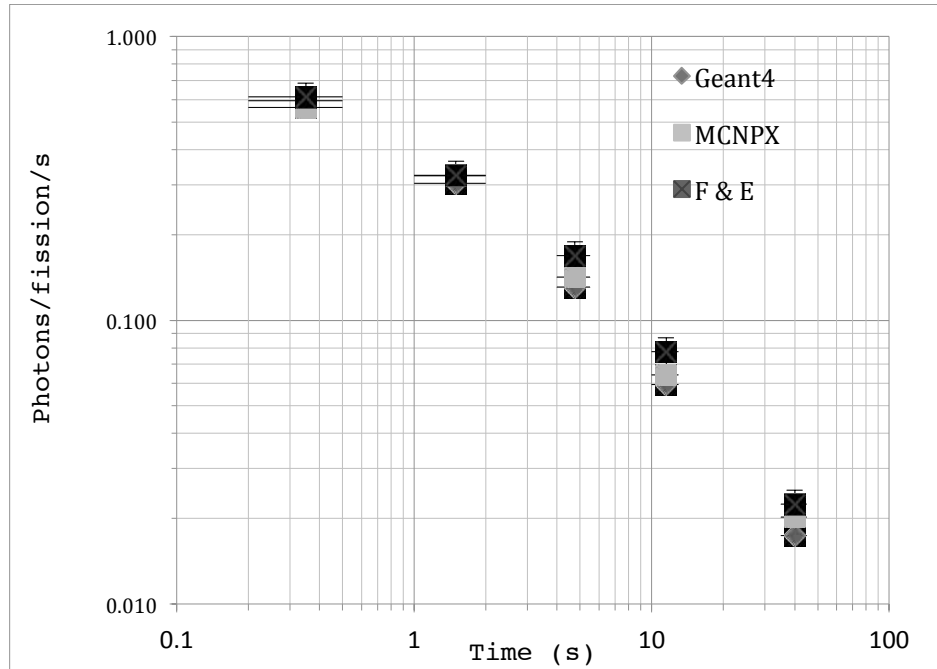


Figure A3: Comparison of average rate of photons per fission.

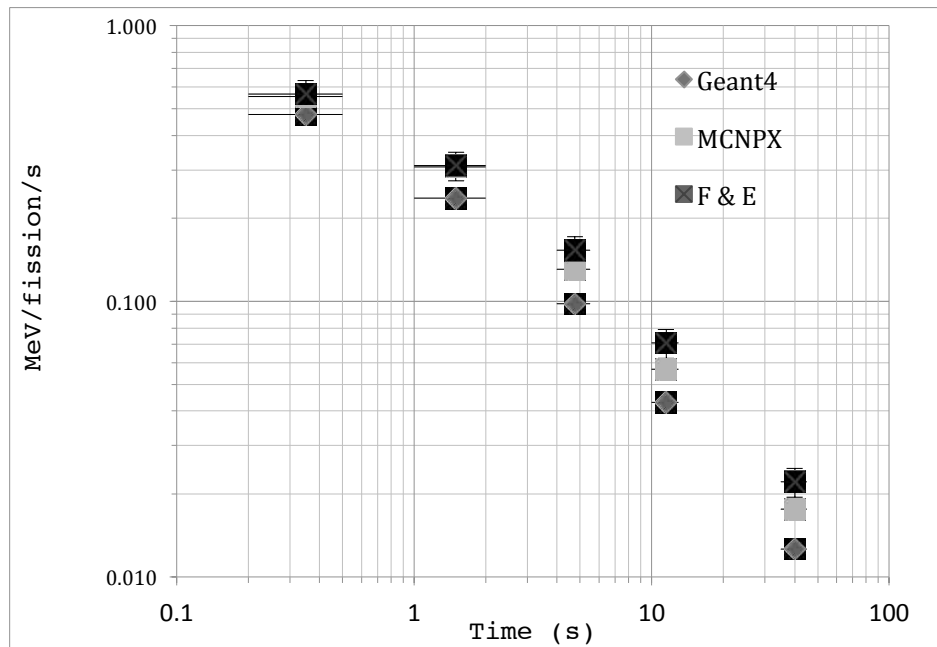


Figure A4: Comparison of average rate of photon energy released per fission.

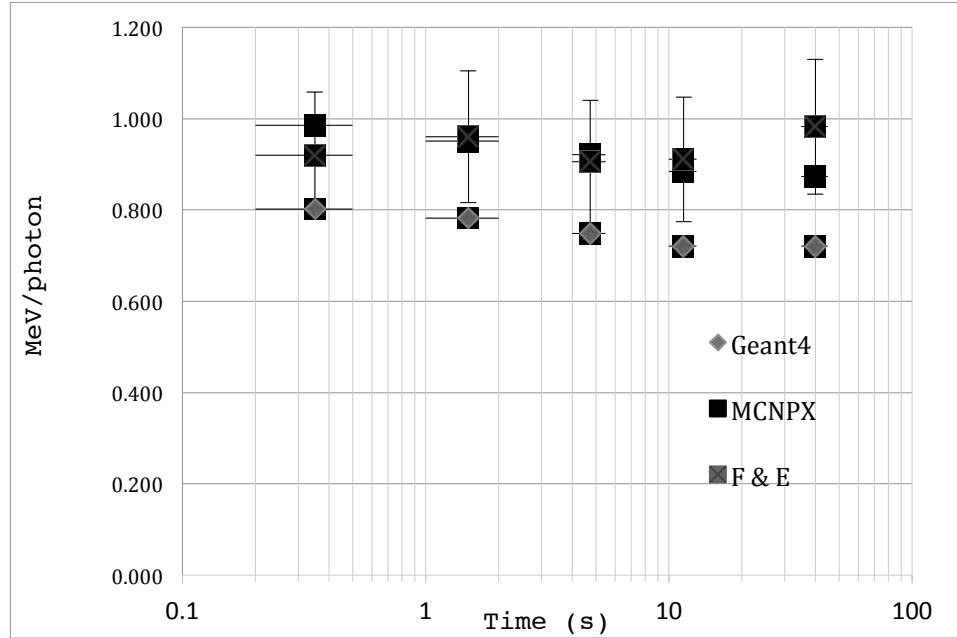


Figure A5: Comparison of time-integrated average energy per photon between computational methods and Fisher and Engle experimental quantities.

We summarize simulation and experimental results in Table A2. Standard statistical uncertainties on simulations are much smaller than experimental errors, and so we do not present them. To compare simulation results, we present the same information in Table A3 as a proportional difference (%) of GEANT4 and of MCNPX/CINDER results below experimental values. All simulation values but for two (marked negative in Table II) are lower than experimental values.

In the Fisher and Engle experimental results, only photons above 0.1 MeV were used. The MCNPX/CINDER photon results do not follow that cutoff, using the broad photon library distribution in CINDER rather than tracking individual decays and photons. GEANT4, though it uses libraries for specific reactions and

decays, and the low energy limit for the production of secondaries is set by a lower length track length cutoff. For shorter cutoff lengths, more low energy photons are produced slightly affecting the final reported values for both total energy and number of photons. We used the default cut of 1 mm minimum required for photon track length. This relates to the creation of secondary particles, including photons created in the fission process. Secondary particles that are created in a physical process will not be generated if the range is less than 1 mm for the secondary particle in question

Table A2: Results from the Fisher and Engle experiment, GEANT4 simulation, and MCNPX/CINDER simulation.

	<i>Fisher and Engle</i>	<i>GEANT4</i>	<i>MCNPX/CINDER</i>
<u>Interval (sec)</u>	<u>Photons/Fiss/s</u>	<u>Photons/Fiss/s</u>	<u>Photons/Fiss/s</u>
0.2 - 0.5	0.613(74)	0.594	0.562
1.0 - 2.0	0.324(39)	0.304	0.323
4.0 - 5.5	0.169(20)	0.131	0.142
10.0-13.0	0.0775(93)	0.0592	0.0640
35.0-45.0	0.0225(27)	0.0174	0.0202

	<i>Fisher and Engle</i>	<i>GEANT4</i>	<i>MCNPX/CINDER</i>
<u>Interval (sec)</u>	<u>MeV/Fiss/s</u>	<u>MeV/Fiss/s</u>	<u>MeV/Fiss/s</u>
0.2 - 0.5	0.564(68)	0.476	0.554
1.0 - 2.0	0.311(37)	0.237	0.307
4.0 - 5.0	0.153(18)	0.098	0.131
10.0-13.0	0.0706(85)	0.0427	0.0566

(Table A2 continued)

35.0-45.0	0.0221(27)	0.0126	0.0176
-----------	------------	--------	--------

<u>Interval (sec)</u>	<u>MeV/Photon</u>	<u>MeV/Photon</u>	<u>MeV/Photon</u>
0.2 - 0.5	0.920(138)	0.802	0.985
1.0 - 2.0	0.960(144)	0.782	0.951
4.0 - 5.0	0.905(136)	0.748	0.921
10.0-13.0	0.911(137)	0.721	0.884
35.0-45.0	0.982(147)	0.721	0.873

<u>Full time (sec)</u>	<u>Photons/Fission</u>	<u>Photons/Fission</u>	<u>Photons/Fission</u>
0.2-45.0	3.31(46)	2.707	2.66

Table A3: Proportional difference below Fisher and Engle experimental values, of GEANT4 and of MCNPX/CINDER results. All differences are in percent (%).

GEANT4 MCNPX/CINDER

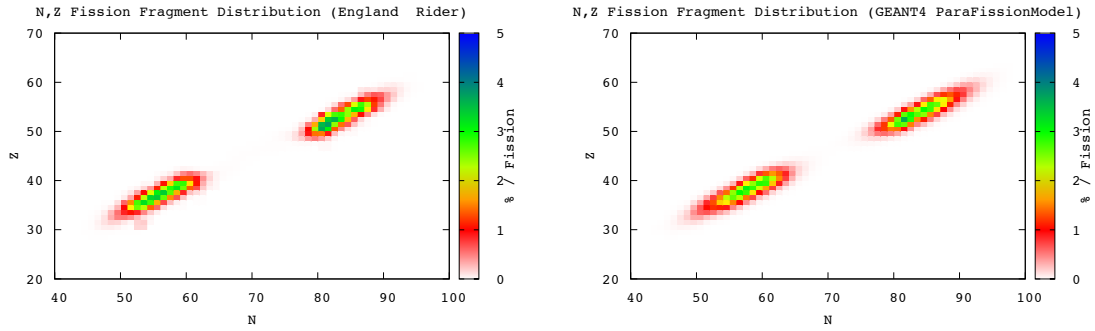
<u>Interval (sec)</u>	<u>Photons/Fiss/s</u>	<u>Photons/Fiss/s</u>
0.2 - 0.5	3.1	8.3
1.0 - 2.0	6.3	0.3
4.0 - 5.5	22.4	16.0
10.0-13.0	23.6	17.4
35.0-45.0	22.5	10.2

(Table A3 continued)

<u>Interval (sec)</u>	<u>MeV/Fiss/s</u>	<u>MeV/Fiss/s</u>
0.2 - 0.5	15.6	1.8
1.0 - 2.0	23.8	1.3
4.0 - 5.5	35.9	14.4
10.0-13.0	39.1	19.8
35.0-45.0	43.2	20.4

<u>Interval (sec)</u>	<u>MeV/Photon</u>	<u>MeV/Photon</u>
0.2 - 0.5	12.8	- 7.1
1.0 - 2.0	18.6	0.9
4.0 - 5.5	17.3	- 1.8
10.0-13.0	20.9	3.0
35.0-45.0	26.6	11.1

<u>Full time (sec)</u>	<u>Photons/Fission</u>	<u>Photons/Fission</u>
0.2-45.0	18.1	19.6



(a)

(b)

Figure A6: a) Contour plot of fission product data from England & Rider for ^{235}U in % / fission. b) Contour plot of simulated fission product data for ^{235}U using GEANT4 in % / fission.

One clear difference in the results returned by the GEANT4 simulation is the fission fragment yield distribution. GEANT4 determines the fragment yield based on a numerical Monte Carlo scheme, while CINDER determines the yield based on data tables sampled using deterministic methods. The G4CompetitiveFission class samples a weighted function of the symmetric and asymmetric Gaussian distributions to best accurately represent yield results. Further investigation into how to modify or compensate for the differences is necessary for more accurate delayed gamma results using GEANT4.

A.2.6 Further Simulation Work

We will need to conduct further work in several areas of the GEANT4 simulation to better represent exploratory methods carried out by Fisher and Engle before moving on to comparison of more complex experiments. The GEANT4

simulation underestimates all delayed-gamma related quantities, which is more severe for the later, longer time periods obtained from the simulation results. We are currently working to improve our initial results by addressing factors that may be contributing to the underestimation of delayed-gamma results.

Another possible issue is the lack of spontaneous decay and fission within our initial simulation. Within the initial GEANT4 model, the spherical mass of ^{235}U does not undergo spontaneous decay or fission. In that framework, for a ^{235}U atom to experience a radioactive decay it must first become active by means of an elastic or inelastic scatter process. To address this problem, we make the atom active within GEANT4 to produce spontaneous decay. We are currently working to implement the GEANT4 class General Particle Source to achieve this task. The General Particle Source class works by randomly distributing ^{235}U atoms with zero kinetic energy within the sphere to simulate the decay process. This enables the radioactive decay process to occur without the need to activate ^{235}U atoms through scatter processes.

This work focused on simulations of photon signatures of SNM. Another quantity of interest in determining the existence of SNM could come from the delayed neutron signature. Delayed neutrons, emitted following some beta decays, are currently not being generated by the radioactive decay model that is employed for this simulation. Although the probability of beta-delayed neutron emission is on the order of 1% per fission, even with the fission sample size we obtained we would still expect to see the clear presence of beta-delayed neutrons. Another option to solve this problem could be to include a statistical,

chronological release of delayed neutrons from the ParaFissionModel. Currently this method is being used in the G4NeutronHPFission model and the functionality could possibly be integrated into our program, however the G4NeutronHPFission model does not produce fission fragments and therefore does not generate delayed gamma emission, which was the primary result of interest. Hence the ParaFissionModel was used for this preliminary study. We are currently investigating the hybridization of these two fission models.

A.2.7 Simulation Conclusions

Investigations were focused on the appropriateness of GEANT4 for fission simulations relevant to active interrogation, following the processes from neutron-induced fission through the fission fragment decay chains and photon emissions. The flexibility of the GEANT4 simulations makes this a highly desirable tool to use. The Fisher and Engle experiment on neutron-induced fission on ^{235}U was used as a standard. We used the quantities MeV/fission/sec, gamma/fission/sec, and MeV/photon for comparison with experiment, and for comparison with MCNPX/CINDER simulation. GEANT4 results compared well using these metrics, though there were discrepancies seen in the fission product distributions. Simulation results for these metrics for both MCNPX/CINDER and GEANT4 were lower than experimental values, with GEANT4 lower than MCNPX/CINDER. The GEANT4 results were typically below 20 percent of the experimental values using these metrics, with an increased accuracy in the earlier time bins. This preliminary comparison suggests GEANT4 as a useful simulation tool for active interrogation. With a large community of developers continually

adding new classes and content, the open source nature of the GEANT4 toolkit allows for expansion into a wider variety of simulated experimental settings.